An improved understanding of Zr-in-rutile thermometry in application to ultrahigh temperature metamorphic rocks

Thesis submitted in accordance with the requirements of the University of Adelaide for an Honours Degree in Geology/Geophysics

Adrian Gaehl

November 2016

THE UNIVERSITY
of ADELAIDE

TITLE

An improved understanding of Zr-in-rutile thermometry in application to ultrahigh temperature metamorphic rocks

RUNNING TITLE

ZIR thermometry

ABSTRACT

Zirconium in rutile (ZIR) concentrations were analysed in samples from two localities in ultrahigh temperature (UHT: >900 °C) metamorphic terranes: Anakapalle, Eastern Ghats Province, India (~1030 °C), and Ayatollah Island, Napier Complex, Antarctica (~1050 °C). ZIR temperatures from analyses of these rocks were categorised according to their microstructural setting—inclusion versus grain boundary—and distance from xenocrystic zircon. ZIR temperatures from three of four samples were all or mostly well below UHT conditions—up to 400 °C in some cases. However, upon reintegrating exsolved zirconium back into rutile grains the distribution of ZIR temperatures in all samples becomes bimodal, more typical of the global UHT ZIR thermometry dataset. There is no obvious trend in the ZIR concentration or temperature data relating to the proximity of rutile to xenocrystic zircon, or to the microstructural setting of rutile, suggesting that rutile and zircon (and quartz) communicate over sufficiently long length scales during the prograde and retrograde history. Stunted Si diffusion does not appear to have been a dominant factor in determining ZIR concentrations and temperatures (contrast with Taylor-Jones & Powell, 2015), as there are no known examples of rutile grains preserving peak (i.e. >1000 °C) temperatures that have *not* exsolved zircon. The major consequence is that ZIR thermometry may almost never preserve the *peak* UHT conditions in regional terranes where cooling is prolonged. The bimodal ZIR concentration and temperature distribution may relate to a subtle, undetected microstructural control on access to Si and Zr reservoirs combined with different timing of growth of different rutile grains.

KEYWORDS

Zirconium in rutile, trace element thermometry, UHT, Eastern Ghats, Napier Complex,

pseudosection

TABLE OF CONTENTS

LIST OF FIGURES AND TABLES

INTRODUCTION

Determining peak conditions of ultrahigh temperature (>900 °C, (Harley, 1998)), UHT, metamorphic rocks has traditionally been difficult, as common thermometers that rely on Fe–Mg exchange are diffusively active well below peak temperatures of UHT rocks (Fitzsimons & Harley, 1994; Pattison & Begin, 1994; Pattison et al., 2003). Hence, they rarely successfully record the peak conditions of these rocks (Fitzsimons & Harley, 1994; Pattison & Begin, 1994; Pattison et al., 2003). More recently, the ability to calculate phase diagrams (i.e. pseudosections) in model chemical systems closely approximating the major element chemistry of rocks has greatly assisted our understanding of peak temperatures achieved in UHT metamorphism (e.g. Kelsey et al., 2004; Kelsey et al., 2005; Korhonen et al., 2011; Taylor-Jones & Powell, 2015). However, the calculation of phase diagrams is commonly time-consuming and complex. The rise of single mineral trace element thermometry has offset and/or value added to the calculation and use of pseudosections.

In the context of UHT rocks, ZIR thermometry (Zack et al., 2004; Ferry & Watson, 2007; Tomkins et al., 2007) has found widespread use (Zack et al., 2004; Watson et al., 2006; Ferry & Watson 2007; Tomkins et al., 2007; Racek et al., 2008; Luvizotto and Zack, 2009; Jiao et al., 2011; Meyer et al., 2011; Kooijman et al., 2012; Korhonen et al., 2014; Pape et al., 2016). Rutile is a common oxide mineral and can incorporate Zr^{4+} into its lattice, replacing Ti^{4+}, and this substitution has a measurable temperature and pressure dependence (Zack et al., 2004; Ferry & Watson, 2007; Tomkins et al., 2007). Because of this, concentrations of Zr in rutile can be used to determine metamorphic temperatures. To be applied, the ZIR thermometer depends on the presence of rutile, a

Zr-bearing phase (i.e. zircon) and a SiO_2 bearing phase (i.e. quartz). Each of these minerals is stable at UHT conditions, and hence this thermometer may be a powerful tool when applied to these rocks.

ZIR thermometry from a global dataset of UHT rocks reveals a distinctly bimodal temperature distribution (Kelsey & Hand, 2015), with the lower temperature peak corresponding to a mean temperature of ~775 °C and comprising ~40% of the dataset. The higher temperature peak corresponds to a mean temperature of ~925 °C. Multiple studies have attempted to explain this bimodal temperature distribution with contrasting interpretations (Ewing et al., 2013; Taylor-Jones & Powell, 2015; Pape et al., 2016). In order for the ZIR thermometer to be successfully applied to, and interpreted from, UHT rocks, it is necessary to understand the cause of this bimodal temperature distribution. In this study I investigate a potential influence on ZIR temperature that is hitherto unstudied, namely the microstructural location of rutile with respect to quartz and xenocrystic zircon[1].

The ZIR data in this study is provided within a calculated pressure–temperature (P–T) pseudosection framework for three of the four samples—to constrain and demonstrate the UHT nature of the samples prior to undertaking ZIR analysis—and additionally takes into consideration two other novel approaches: The abundance of zircon and rutile in the rocks, and the distance separating rutile from xenocrystic zircon.

---

[1] Xenocrystic in this context refers to zircon that is foreign to the rutile, i.e., not formed by exsolution from rutile during cooling.

BACKGROUND

Ultrahigh temperature (UHT) metamorphism is a subcategory of granulite facies metamorphism in which non-igneous crustal temperatures exceed 900 °C (e.g. Harley, 1998; Kelsey & Hand, 2015). UHT metamorphism can also be defined by apparent thermal gradients ≥75 °C.kbar^{-1} (Brown, 2007; Brown, 2014) and therefore indicates a highly perturbed crustal thermal regime.

UHT metamorphism is commonly recognised via diagnostic silicate mineral assemblages. These assemblages are generally found in Mg- and Al-rich pelitic rocks (Harley, 1998; Harley, 2008; Kelsey 2008; Kelsey & Hand, 2015), and include sapphirine–quartz, Al-rich orthopyroxene–sillimanite–quartz, and osumilite (Kelsey et al., 2005). As these exotic assemblages are rare in nature, it is imperative that a method of identifying UHT conditions by other means exists for application to rocks containing more common silicate minerals. Thermometers based on Fe-Mg exchange between common silicate minerals are often diffusively active until well below UHT conditions and will therefore rarely, if ever, record the peak or elevated conditions of granulite and UHT rocks (Fitzsimons & Harley, 1994; Pattison & Begin, 1994; Pattison et al., 2003).

Rutile is a common accessory mineral in crustal rocks, and Zr-in-rutile thermometry is one of several single mineral trace element thermometers that have been proposed over the past decade (Zack et al., 2004; Watson & Harrison, 2005; Wark & Watson, 2006; Kawasaki & Motoyoshi, 2007). For UHT rocks, ZIR thermometry is a promising trace element thermometer (Kelsey & Hand, 2015) that created the possibility that UHT metamorphism can and will be recognised in a far greater number of terranes. Indeed, UHT conditions have been obtained from ZIR thermometry in a large number of studies (Baldwin & Brown, 2008; Racek et al., 2008; Luvizotto and Zack, 2009; Kotková and

Harley, 2010; Jiao et al., 2011; Meyer et al., 2011; Ague and Eckert, 2012; Blackburn et al., 2012; Kooijman et al., 2012; Ague et al., 2013; Ewing et al., 2013; Korhonen et al., 2014; Pape et al., 2016). However, in all cases, a bimodal temperature distribution occurs (global dataset compiled in Kelsey & Hand, 2015), where the lower-temperature peak (~40% of dataset) occurs at ~750–800 °C, well below UHT conditions. The higher-temperature peak (~60% of dataset) occurs at ~900–1000 °C with a mean of ~925 °C (Kelsey & Hand, 2015). This temperature distribution is thought to be due to exsolution of zircon or another Zr-bearing mineral, e.g. baddelyite, from rutile with cooling (e.g. Ewing et al., 2013; Taylor-Jones & Powell, 2015; Pape et al., 2016), rather than diffusive loss of Zr from rutile with cooling (e.g. Ewing et al., 2013). Importantly, the temperature distribution is not thought to be due to post-peak retrogression of UHT rocks, as demonstrated clearly by Ewing et al. (2013).

Rutile (TiO_2), when in equilibrium with quartz and zircon, incorporates Zr^{4+} into its structure as a substitute for Ti^{4+} (Zack et al., 2004; Watson et al., 2006). This substitution has a positive temperature dependence (Zack et al., 2004; Watson et al., 2006; Ferry & Watson, 2007), and a lesser negative pressure dependence (Tomkins et al., 2007). There are two ZIR thermometers in use, both of which are based on the pioneering work by Zack et al. (2004). The two thermometers are based on the equilibrium relationship Zr(in rutile) + SiO_2 $\rightarrow$ zircon (Zack et al., 2004; Watson et al., 2006; Ferry & Watson, 2007; Tomkins et al., 2007). The first, by Ferry & Watson (2007) (herein referred to as **FW07**) does not have a pressure dependence, but has a dependence upon the activity of silica ($a SiO_2$), whereas the later Tomkins et al. (2007) formulation (herein referred to as **To07**) has a pressure dependence but is independent of $a SiO_2$.

The To07 thermometer in the β-quartz field is described mathematically as:

$$T(°C) = \frac{85.7 + 0.473P}{0.1453 - Rln\phi} - 273$$

Where ϕ is ppm Zr, P is in kbar and R is the gas constant, 0.0083144 kJ K^{-1}.

The FW07 thermometer is described mathematically as:

$$T(°C) = \left(\frac{(4530 \pm 111)}{(7.420 \pm 0.105) \times log_{(ppm\ Zr-in-rutile)}} - log_{a_{SiO_2}} \right) - 273$$

If aSiO$_2$ is less than unity the retrieved temperatures will be lower for a given ZIR concentration (Ferry & Watson, 2007), as a reduction in aSiO$_2$ will result in reduced efficacy of exsolution of Zr from rutile, and hence rutile will be over-saturated in Zr during cooling, giving inaccurately high ZIR thermometry results (Ferry & Watson, 2007; Taylor-Jones & Powell, 2015).

Numerous studies (Zuvizotto & Zack, 2009; Jiao et al., 2011; Meyer et al., 2011; Kooijman et al., 2012; Ewing et al., 2013; Pape et al., 2016) present compositional profiles across rutile grains that commonly show unchanging ('flat') Zr concentrations. This is consistent with rapid diffusion of Zr in and out of rutile, despite experimental data that contrasts with this observation (Cherniak et al., 2007). However, Zr concentrations ranging more than two orders of magnitude *between* rutile grains from the same sample (e.g. Zack et al., 2004; Ewing et al., 2013) are common. This suggests there is a control upon retention of Zr by rutile grains that is not yet fully understood, but may relate to the proximity of rutile to xenocrystic zircon (Zack et al., 2004; Taylor-Jones & Powell, 2015) and/or whether the rutile has exsolved a Zr-bearing phase during cooling. The proposed scenarios by which the bimodal temperature distribution may

occur are internal (no net Zr loss) versus external (net Zr loss) exsolution of a Zr-bearing mineral (zircon or baddelyite) from rutile during cooling, as well as no exsolution or diffusive Zr loss during cooling (Ewing et al., 2013; Taylor-Jones & Powell, 2015; Pape et al., 2016). Of these, the third is least understood, but may relate to the ability of rutile to diffuse Si (e.g. Ferry & Watson, 2007; Taylor-Jones & Powell, 2015). With specific regard to microstructural location of rutile, Zack et al. (2004) provide data suggesting that rutile grains held as inclusions in garnet or orthopyroxene commonly record the highest temperatures, whereas grains outside of garnet or orthopyroxene commonly recorded the lowest temperatures (see also Ewing et al., 2013). Zack et al. (2004) postulated that rutile within the rock matrix, or located along fracture planes or at grain boundaries, will more readily re-equilibrate to record lower temperature conditions (Taylor-Jones & Powell, 2015). Crucially, what remains unknown is the critical distance—if it exists—that rutile must be from xenocrystic zircon to disallow chemical communication between rutile and zircon and preserve high Zr concentrations in rutile pertaining to UHT conditions. I investigate this in this study using samples from two well-known UHT terranes.

Study Area

Rock samples selected for analysis were chosen from localities in terranes with well-constrained UHT conditions. Samples AK-3, AK-5 and AK-6 are from Anakapalle, Eastern Ghats Province, India (Fig. 1). Sample R31180 is from Ayatollah Island, Khmara Bay, part of the Napier Complex of Enderby land, Antarctica (Fig. 2).

ANAKAPALLE

The Eastern Ghats Province (Fig. 1) is a granulite facies terrane that records $P–T$

conditions exceeding ~9–10 kbar and 1000 °C. Numerous studies have attempted to

quantify the pressure and temperature conditions of the province (Sengupta et al., 1990;

Dasgupta et al., 1994, 1995; Bose et al., 2000; Sarkar et al., 2003; Bose & Das, 2007;

Korhonen et al., 2011, 2013, 2014), however confusion remains regarding the timing of

parts of the $P–T$ history. Nevertheless, the metamorphic history is characterised by an

early up-pressure, anticlockwise-shape $P–T$ path at UHT conditions (Korhonen et al.,

2014) and a later down-pressure, clockwise-shape $P–T$ path (Simmat & Raith, 2008),

arguably also at UHT conditions (Rickers et al., 2001). Metamorphic ages between

1500–520 Ma provide evidence for polymetamorphism. Recent U–Pb geochronology

indicates that UHT metamorphism occurred between c. 1000–930 Ma, or possibly c.

1130–930 Ma (Korhonen et al., 2013). The lack of resolution largely relates to the

difficulty in interpreting geochronology from UHT terranes, which is typically spread

along concordia (e.g. Kelly & Harley, 2005; Halpin et al., 2012; Korhonen et al., 2013;

Taylor et al., 2015; Walsh et al., 2015; Morrissey et al., 2016).
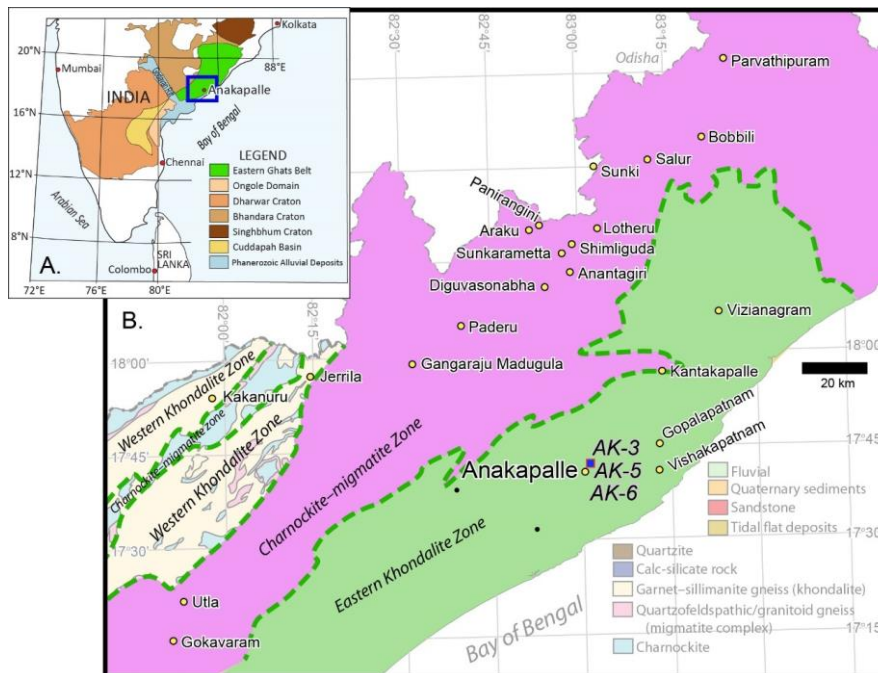
Figure 1 (A) Location of Eastern Ghats Province (green) in India; (B) Simplified map of a portion of the Eastern Ghats Province, India, showing the location of Anakapalle and sample locations with respect to other localities in the Province where metamorphic studies of UHT rocks have been conducted. Figure adapted from (Marshall, 2010).

ENDERBY LAND

The Napier Complex is an Archaean cratonic block in Enderby Land in the East Antarctic Shield (Fig. 2; Kelly & Harley, 2005). The Napier complex is characterised by regionally pervasive UHT mineral assemblages that are indicative of peak metamorphic conditions of 7–11 kbar and 1050–1120 °C (Harley, 1998; Harley & Motoyoshi, 2000; Kelly & Harley, 2005). The terrane experienced three main phases of metamorphism between c. 2990–2450 Ma (Harley 1998; Kelly & Harley, 2005), and resided in the deep crust for up to c. 1500 Myr after the UHT event which involved near-isobaric cooling (Sandiford, 1985a; Harley & Motoyoshi, 2000; Kelly & Harley, 2005). UHT metamorphism is thought to have occurred at c. 2450 Ma (Kelly & Harley, 2005).
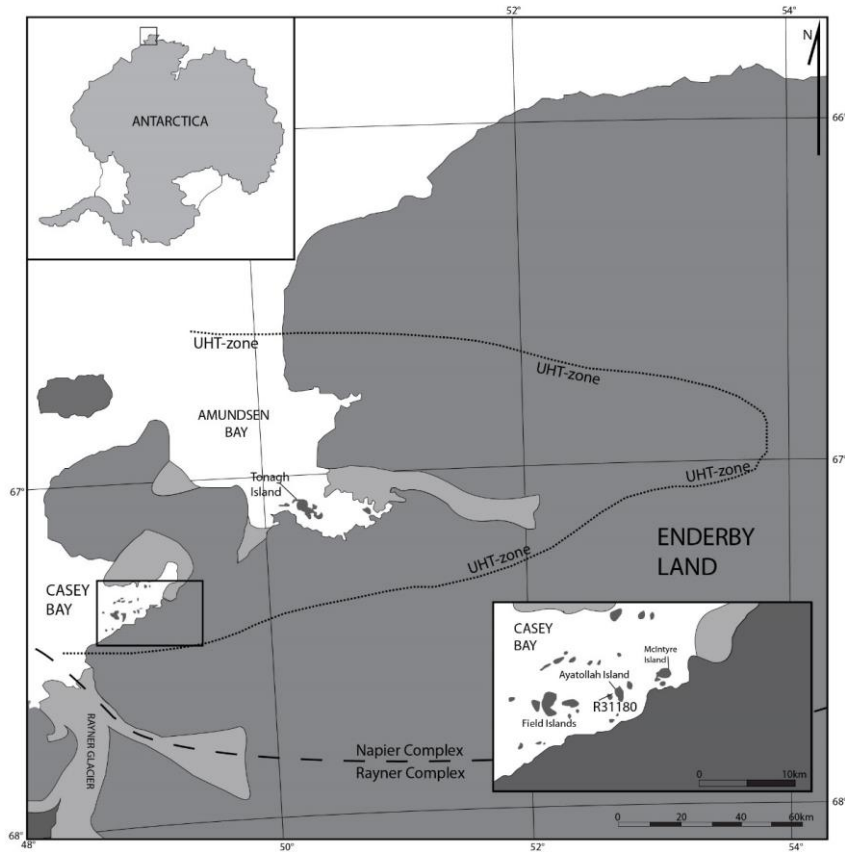
Figure 2 Simplified map of the Napier Complex, Antarctica, with inset of Casey Bay. Sample R31180 sourced from Ayatollah Island. (Modified from Kelly & Harley 2005). Regional UHT metamorphism, with rocks containing sapphirine + quartz, orthopyroxene + sillimanite + quartz and osumilite-bearing assemblages, occurs inside of the dashed UHT zone boundary.

Petrography

Full petrographic descriptions for each sample are provided in Appendix A.

AK-3

The interpreted peak metamorphic assemblage for sample AK-3 is $biotite_1$–$garnet_1$–$orthopyroxene_1$–$spinel_1$–plagioclase–K-feldspar–rutile–melt. The interpreted post-peak, retrograde minerals are $sapphirine_2$ and $orthopyroxene_2$ ($\pm$ $plagioclase_2$) followed by $sillimanite_3$, $biotite_3$ and $plagioclase_3$; and then $garnet_4$ (Fig. 3).
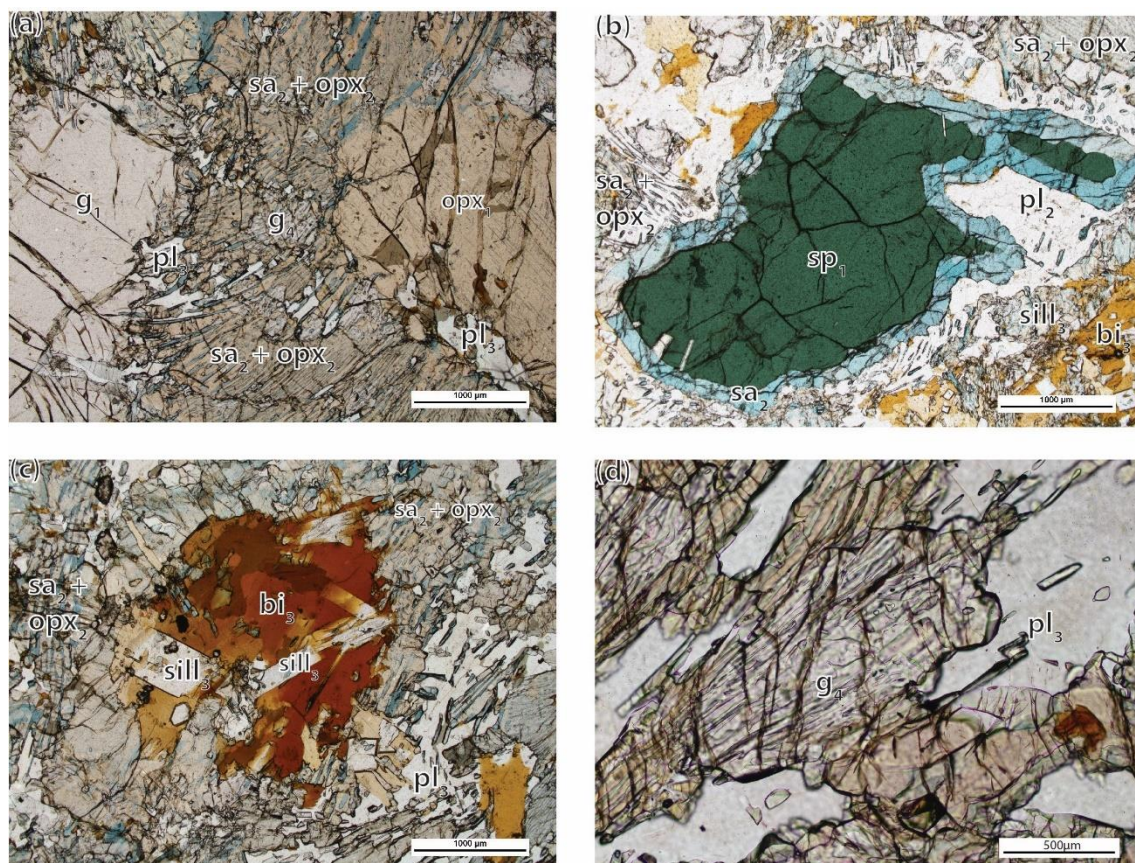
Figure 3 Optical microscope images showing reaction microstructures from sample AK-3. g = garnet, opx = orthopyroxene, sa = sapphirine, pl = plagioclase, sp = spinel, bi = biotite, sill = sillimanite. (A) Coarse-grained garnet (g_1) and orthopyroxene (opx_1) separated by finer-grained symplectite of sapphirine (sa_2) and orthopyroxene (opx_2), with later development of plagioclase (pl_3)

and fine-grained garnet (g_4). **(B) Coarse-grained spinel separated from sa_2 + opx_2 symplectites by a corona of sapphirine. Post-peak plagioclase (as pl_2) is reasonably extensively developed. Later biotite–sillimanite patches ($sill_3$, bi_3) occur in bottom right of picture. (C) Detail of late biotite (bi_3) and sillimanite ($sill_3$) that post-dates the sapphirine (sa_2) + orthopyroxene (opx_2) symplectites. In rare cases, the bi + sill patches can be seen to surround sa_2 + opx_2 symplectites and separate them from coarse-grained garnet and orthopyroxene. (D) Close-up photo of late garnet (g_4) containing inclusions of rib-like sapphirine (sa_2) and orthopyroxene (opx_2).**

AK-5

The interpreted peak metamorphic assemblage for sample AK-5 is orthopyroxene$_1$–garnet–sillimanite$_1$–quartz–K-feldspar$_1$–rutile (and melt), where K-feldspar is ternary feldspar. The post-peak minerals are interpreted to be sapphirine$_2$, plagioclase$_2$, K-feldspar$_2$, cordierite$_2$, biotite$_2$ and orthopyroxene$_2$, followed by sillimanite$_3$, cordierite$_3$, biotite$_3$, and then garnet$_4$ (Fig. 4).

Figure 4 Optical microscope images of sample AK-5, showing reaction microstructures and textural relationships of peak and post-peak minerals. g = garnet, opx = orthopyroxene, pl = plagioclase, ksp = k-feldspar, sa = sapphirine, sill = sillimanite, fsp = feldspar (perthitic), q = quartz,

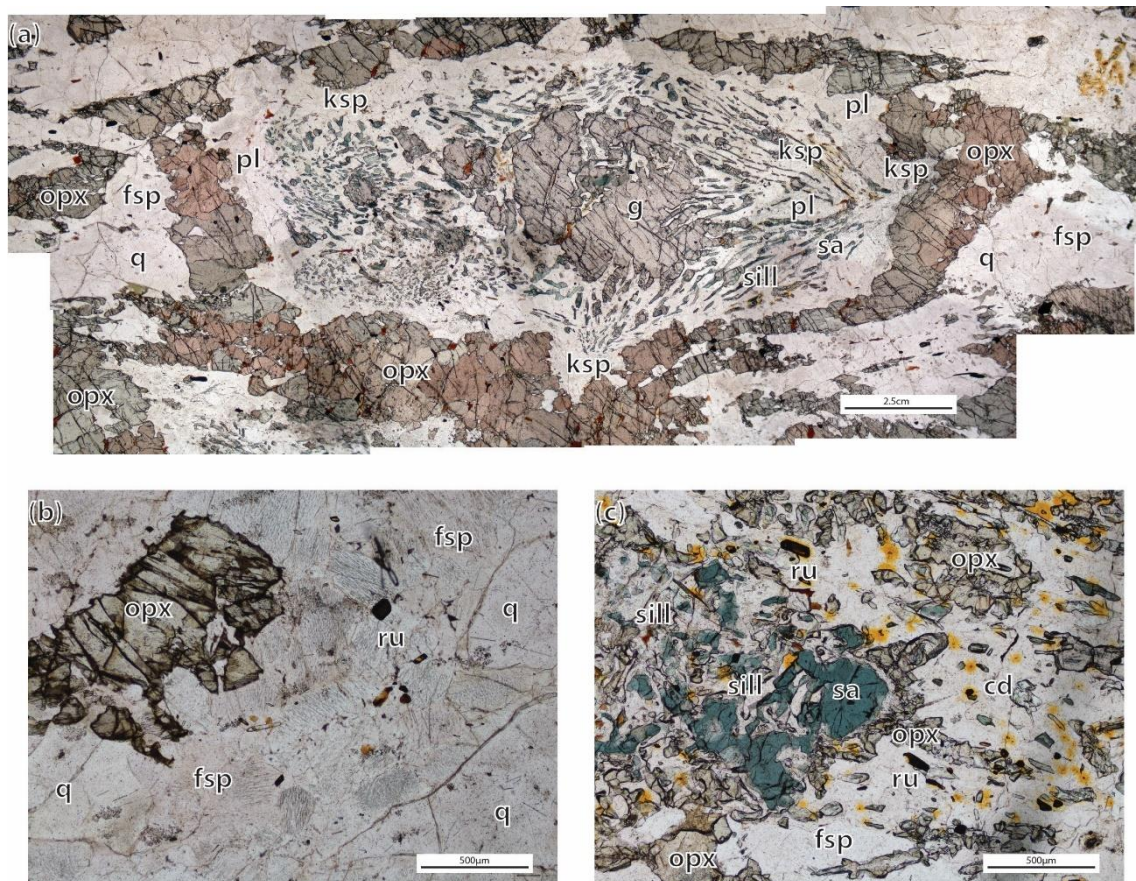**ru = rutile, cd = cordierite. (A) Photo collage of one of the AK-5 thin sections showing garnet at centre mantled by coronas of sapphirine, feldspar, and orthopyroxene. Quartz does not occur in the corona region between garnet and the thick 'ring' of orthopyroxene, but does occur outside the orthopyroxene 'ring. (B) Close up of the quartz-bearing matrix showing perthitic and mesoperthitic feldspar along with orthopyroxene and quartz. (C) Close up of sapphirine in the symplectite structure, which is isolated from symplectic orthopyroxene by later sillimanite and abundant cordierite. Presence of cordierite can be identified by common yellow radiation damage halos.**

AK-6

Figure 5 Optical microscope images of sample AK-6, showing reaction microstructures and relationships is peak and retrograde minerals. g = garnet, sa = sapphirine, opx = orthopyroxene, fps = feldspar, q = quartz, ru = rutile. (A) Garnet porphyroblast with inclusions of early sapphirine and rutile. Garnet is separated from orthopyroxene by feldspar. (B) Elongate porphyroblast of garnet containing inclusions of sapphirine and rutile set in a quartz- and feldspar-rich matrix. Feldspar immediately surrounds garnet.

The interpreted peak metamorphic assemblage for sample AK-6 is orthopyroxene–garnet–K-feldspar–quartz–rutile–melt. Prograde minerals are interpreted to be sillimanite, sapphirine and rutile. The post-peak minerals are interpreted to be biotite and K-feldspar. The significance of matrix sillimanite is unclear (Fig. 5).

R31180

The interpreted peak mineral assemblage for sample R31180 is quartz–sapphirine–mesoperthitic K-feldspar–rutile–melt. Retrograde minerals are interpreted to be sillimanite, orthopyroxene, corundum and biotite (Fig. 6).
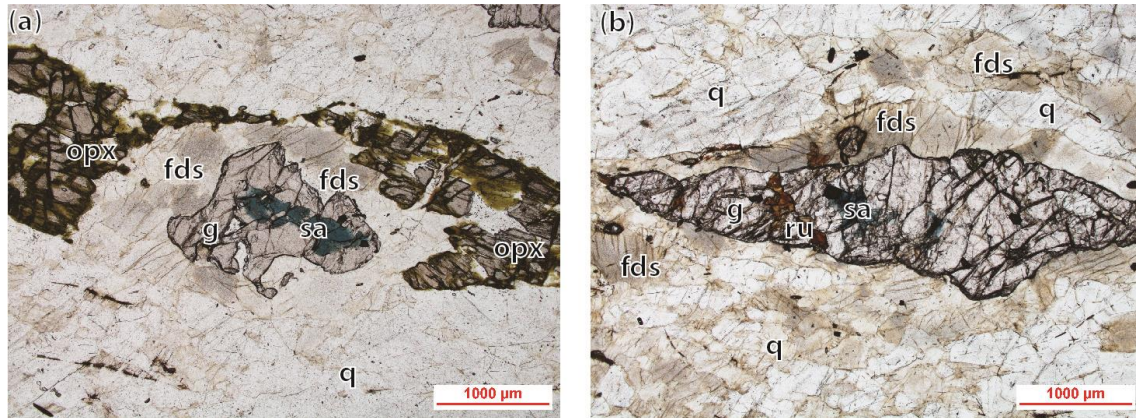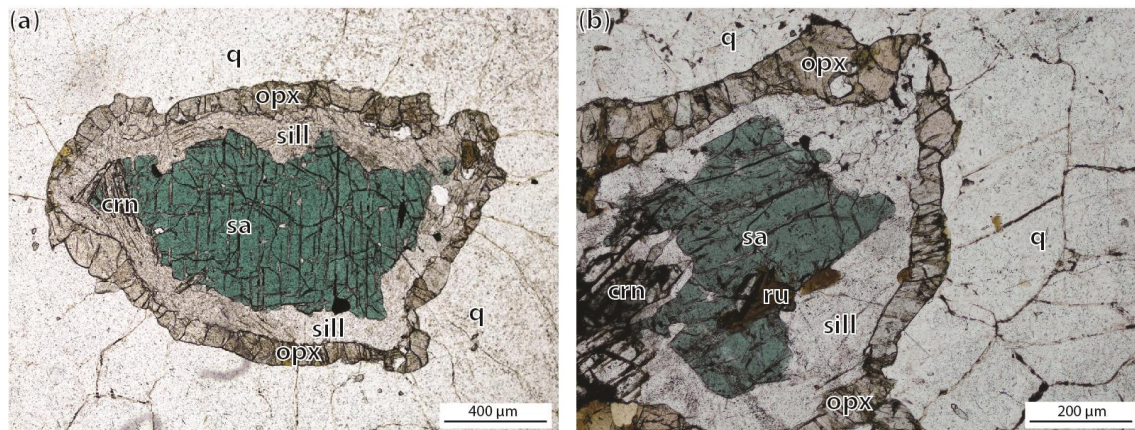
Figure 6 Optical microscope images of sample R31180, showing reaction textures and relationships is peak and retrograde minerals. sa = sapphirine, opx = orthopyroxene, q = quartz, ru = rutile. (A) Classic double-layer corona structure of sillimanite and orthopyroxene separating sapphirine porphyroblast from quartz. A large rutile grain occurs in the top right of the orthopyroxene corona. (B) Close up of sapphirine mantled successively by corundum (at left), sillimanite and orthopyroxene as corona layers that separate sapphirine from quartz.

METHODS

Phase Equilibria Forward Modelling

Phase equilibria calculations were performed using the software program

THERMOCALC (Powell & Holland, 1988; Holland & Powell, 2011) in the model

chemical system $Na_2O–CaO–K_2O–FeO–MgO–Al_2O_3–SiO_2–H_2O–TiO_2–O–ZrO_2$, where

'O' is a proxy for Fe_2O_3, using the latest internally-consistent thermodynamic dataset

'ds6' (filename tc-ds62.txt; Holland & Powell, 2011) and activity–composition (a–x)

models (Powell et al., 2014; White et al., 2014). The Zr-bearing end-members for

garnet, rutile and silicate melt in the a–x models are from Tomkins et al. (2007) and

Kelsey & Powell (2011) and the Ti end-member of silicate melt is from Tomkins et al.

(2007). The initial stable assemblage is determined by performing a Gibbs energy

minimisation calculation at a set pressure–temperature (P–T) condition. The diagram is

built up from and around that initial assemblage and involves many trial and error

calculations in order to determine phase changes as a function of pressure, temperature

13

and/or composition. Therefore, a single diagram commonly comprises ~100-150 total line and point calculations, and the user is intellectually involved in the calculations at every step along the way, amounting to weeks of calculation per diagram. The most uncertain compositional variables are Fe_2O_3 and H_2O, commonly requiring that these be constrained with T–M type diagrams (where M refers to amount of an oxide component). The choice of pressure at which to calculate the T–M diagrams is based on broadly estimating the pressure at which the petrographically-determined peak metamorphic assemblage is stable. The inclusion of Zr in the calculations means that the Zr content of rutile (including ppm ZIR) can be calculated as a direct function of P–T–X.

Phase diagrams were contoured for phase abundance ('mode') and ZIR concentration using the software program TCInvestigator (Pearce et al., 2015). As input, this program requires a completed THERMOCALC pseudosection, the a–x and thermodynamic dataset files used to calculate the pseudosection, and a list of stable assemblages corresponding to the fields in the pseudosection.

Rock compositions

Rock compositions used for the calculation of phase diagrams for Anakapalle samples were based on whole-rock geochemistry obtained from Franklin and Marshall College, Pennsylvania. Major elements were analysed by fusing 0.4g of the powdered sample (sample powdered at Franklin and Marshall College) with lithium tetraborate for analysis by XRF. Trace elements—including Zr—were analysed by mixing 7g of crushed rock powder with Copolywax powder and measurement by XRF. The composition used for the calculation of phase diagrams for sample R31180 involved

combining measured mineral chemistry from the sample (Sandiford, 1984) and the

abundance of minerals estimated from thin section. The ZrO_2 concentration of the

sample R31180 was estimated using the calculated abundance of zircon and rutile in the

thin section as determined by MLA mapping (see below), and the average ZIR

concentration in the sample.

LA–ICP–MS monazite U–Pb geochronology

In-situ monazite U–Pb dating was undertaken for the purpose of demonstrating that the

Anakapalle samples in this study record the effectually same age of metamorphism as

other localities in the Eastern Ghats Province. The methods and results are provided in

Appendix D.

Scanning Electron Microscope (SEM) and Mineral Liberation Analysis (MLA)

The QUANTA 600 SEM at Adelaide Microscopy was used to produce back-scattered

electron (BSE) image mosaics of the entire thin sections of samples AK-3, AK-5, AK-6

and R31180 (Appendix E). These images were produced from carbon-coated thin

sections using a 25 KeV accelerating voltage, under high vacuum conditions, at a

working distance of 10 mm.

Mineral Liberation Analysis (MLA) mapping was also undertaken using the QUANTA

600 SEM (under the same conditions), for identification of mineralogy, mineral

abundance and distribution. Full size thin section maps were obtained for presence of

rutile and zircon (Appendix E).

Electron Probe Microanalysis (EPMA)

Electron probe microanalysis (EPMA) was undertaken at Adelaide Microscopy on individual grains of rutile in order to measure trace element concentrations. Beam operating conditions were 1 µm width and current and voltage of 50 nA and 20 kV, respectively. Two of the five wavelength dispersive spectrometers were used to count Zr with a long dwell time of 45 s. Dwell times for other measured elements were: 25s for Si, Mg, Al, 12s for Ti, and 45s for Cr, Fe, V, Nb. A BSE image of each rutile grain analysed was captured for the purpose of calculating distances between rutile and xenocrystic zircon.

Zr reintegration and Zr thermometry

To reintegrate exsolved zircon (or Zr) back into rutile grains, BSE images of analysed rutile grains were processed using Adobe Photoshop. Pixels with a grey scale corresponding to rutile were counted. Pixels with a grey scale corresponding to zircon were counted, with care being taken not to include xenocrystic zircon grains. The pixel ratio of rutile to zircon was then used in conjunction with the measured ZIR content (from EPMA) in ppm and the known Zr ppm in perfectly stoichiometric zircon ($ZrSiO_4$, 497,664ppm Zr) to calculate the total amount of Zr contained in a rutile grain before exsolution occurred.

ZIR thermometry in this study used the To07 formulation for these scenarios: (a) no reintegration of exsolved Zr back into rutile, for the purpose of quantifying the extent of ZIR temperature reduction due to exsolution loss of Zr; and (b) reintegrated of exsolved Zr (as zircon) back into rutile to quantify the ZIR temperature prior to exsolution occurring. As both the FW07 and To07 thermometers give the same temperatures

within ~5 °C I predominantly use the more recent To07 formulation. The FW07

formulation is used only for quartz-absent sample AK-3.

RESULTS

Phase Equilibria Forward Modelling

In order to calculate a P–T pseudosection for a particular rock, an appropriate rock

composition must first be constrained by calculating P– or T–M_O and P– or T–M_{H2O}

diagrams to constrain the amount of FeO vs Fe_2O_3 (i.e. the oxidation state) and the

amount of H_2O, since these are the most uncertain components of rock composition. In

this study, P–M_O and P–M_{H2O} diagrams were calculated only for sample AK-6, and a T–

M_O diagram was calculated for sample R31180. No P–T pseudosection was calculated

for sample R31180 due to time constraints, but the P–T path can be interpreted from the

T–M_O pseudosection. P–M diagrams were previously calculated by D. Kelsey

(unpublished data) for samples AK-3 and AK-5, such that only P–T pseudosections

were required to be calculated for those samples. The P–M diagrams are presented in

Appendix F.

AK-3

The calculated P–T pseudosection for sample AK-3 is shown in Fig. 7. The peak

assemblage biotite$_1$–garnet$_1$–orthopyroxene$_1$–spinel$_1$–plagioclase–K-feldspar–rutile–

melt occurs over the P–T range ~8.8 to >12 kbar, ~900–1100 °C (without spinel) and

~9.8–11.5 kbar, 1030–1085 °C (with spinel). Post-peak sapphirine occurs in fields to

lower pressure than the peak field(s), that is to pressures lower than ~8.8–10 kbar. Other

post-peak minerals, interpreted to post-date sapphirine (and orthopyroxene$_2$), such as

17

sillimanite[3], biotite[3] and plagioclase[3] and garnet[4] all occur within fields to lower temperature than the first appearance of sapphirine. The *P–T* pseudosection, contoured for the modal abundance ('modes') of some phases, and the ZIR concentration in ppm, is shown in Fig. 8. ZIR concentration increases with increasing temperature.
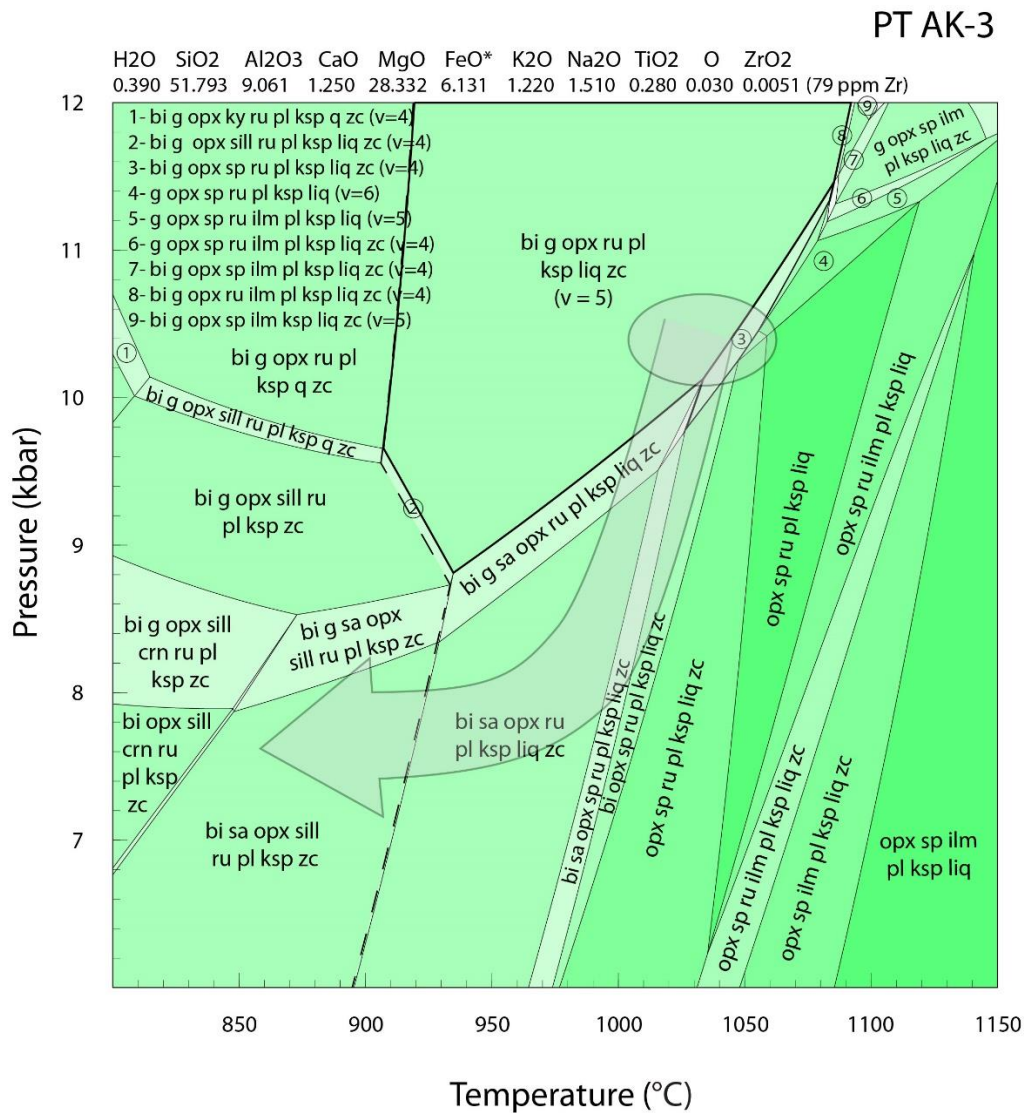
Figure 7 Calculated *P–T* pseudosection graphically representing changes in mineralogy for the composition of sample AK-3 across *P–T* space. Abbreviations: bi = biotite; crn = corundum; g = garnet; ilm = ilmenite; ksp = K-feldspar; liq = silicate melt; opx = orthopyroxene; pl = plagioclase; q = quartz; ru = rutile; sa = sapphirine; sill = sillimanite; sp = spinel; zc = zircon. The composition (in mole%) used to calculate the pseudosection is provided above the diagram. FeO* = FeO + 2 × 'O'. Two fields are highlighted with bold outline as the peak fields, one with spinel and one without, due to the scarcity of coarse-grained spinel in the sample. This constraint of low spinel abundance must place peak conditions near to the boundary between the two fields. The solidus is given as a dashed line and the semi-transparent ellipse and arrow show the interpreted peak *P–T* conditions and post-peak, retrograde path, respectively. Fields are shaded according to their variance: higher variance field are darker, lower variance fields are lighter.

Figure 8 TCInvestigator outputs for the *P–T* pseudosection for sample AK-3 graphically representing: A–E: changes in modal proportions of key silicate minerals as a function of pressure–temperature; F: Zirconium concentration in rutile in ppm as a function of pressure–temperature, showing ZIR to be positively proportional to temperature and negatively proportional to pressure. White space represents regions of *P-T* space in which the mineral being represented is not stable. These diagrams were used to estimate the peak conditions experienced by sample AK-3 by correlating modal mineral abundances in the sample to those calculated, as well as to delineate the post-peak, retrograde *P–T* path.

AK-5

The calculated P–T pseudosection for sample AK-5 is shown in Fig. 9. The peak assemblage orthopyroxene$_1$–garnet–sillimanite$_1$–quartz–K-feldspar$_1$–rutile–melt occurs over the P–T range of ~9.0–11.2 kbar, ~910–1140 °C. The post-peak minerals sapphirine$_2$, plagioclase$_2$ and K-feldspar$_2$ occur in lower pressure fields than the peak assemblage field, and cordierite$_2$ stability occurs to lower pressure than where sapphirine first stabilises. Biotite stability occurs to lower temperature than the high-temperature fields containing sapphirine and cordierite. The P–T pseudosection, contoured for the modal abundance ('modes') of some phases, and the ZIR concentration in ppm, is shown in Fig. 10. ZIR concentration increases with increasing temperature.

PT AK-5

H2O	SiO2	Al2O3	CaO	MgO	FeO*	K2O	Na2O	TiO2	O	ZrO2
0.139	51.172	13.429	0.669	24.803	7.294	0.639	1.287	0.329	0.239	0.0102

1- bi g ru pl sill zc (v=6)
2- bi g opx ru pl ksp sill liq zc (v=4)
3- bi g opx cd ru pl ksp sill zc (v=4)
4- g sa opx cd ru pl ksp sill zc (v=4)
5- sa opx cd ru pl ksp sill q zc (v=4)
6- sa opx cd ru pl liq q zc (v=5)
7- sa opx ru pl liq (v=8)
8- opx ru pl ksp liq sill q zc (v=5)
9- opx ru pl liq sill q zc (v=6)
10- g sa opx ru pl liq sill q zc (v=4)
11- g sa opx ru pl liq sill q (v=5)
12- g sa opx ru pl liq q (v=6)
13- g opx ru pl liq sill q (v=7)
14- g ru pl liq sill q (v=8)

Figure 9 Calculated *P–T* pseudosection graphically representing changes in mineralogy for the composition of sample AK-5 across *P–T* space. Abbreviations: bi = biotite; cd = cordierite; g = garnet; ksp = K-feldspar; ky = kyanite; liq = silicate melt; opx = orthopyroxene; pl = plagioclase; q = quartz; ru = rutile; sa = sapphirine; sill = sillimanite; zc = zircon. The composition (in mole%) used to calculate the pseudosection is provided above the diagram. FeO* = FeO + 2 × 'O'. The field highlighted by bold boundaries is the peak field, and as such the *P–T* path (arrow) must begin within that field from the peak conditions (ellipse). By comparison with the *P–T* path of sample AK-3, which is from the same locality, and retrograde mineralogy (retrograde biotite, cordierite, K-feldspar) the *P–T* path is constrained. The solidus is shown as a dashed line.
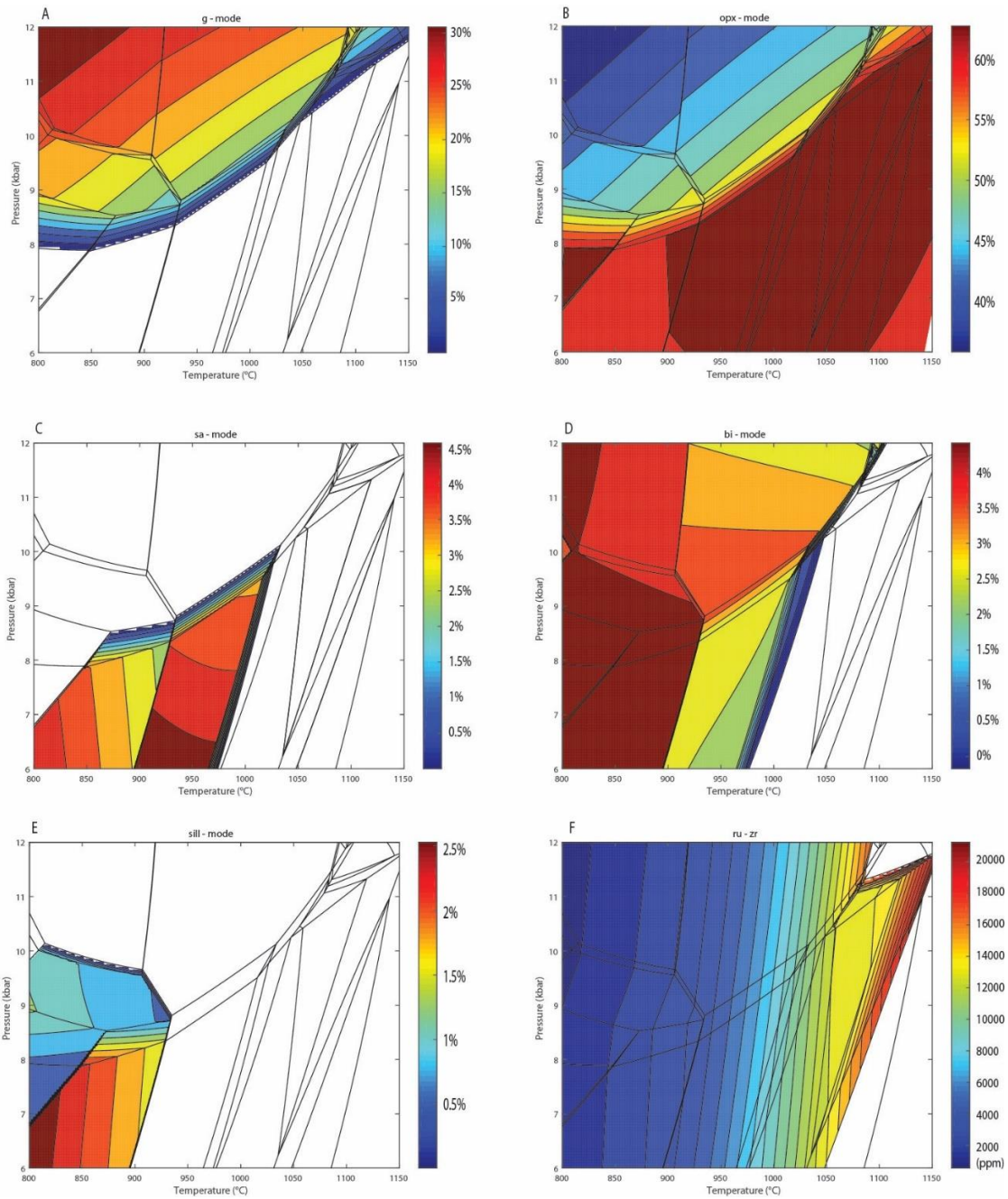
Figure 10 TCInvestigator outputs for the *P–T* pseudosection for sample AK-5 graphically representing: A–E: changes in modal proportions of key minerals as a function of pressure–temperature; F: Zirconium concentration in rutile in ppm as a function of pressure–temperature, showing ZIR to be positively proportional to temperature and negatively proportional to pressure. White space represents regions of *P–T* space in which the mineral being represented is not stable. These diagrams were used to constrain the retrograde *P–T* path recorded by sample AK-5 by correlating modal mineral abundances in the sample to those calculated.

AK-6

The calculated *P–T* pseudosection for sample AK-6 is shown in Fig. 11. The peak

assemblage orthopyroxene–garnet–K-feldspar–quartz–rutile–melt occurs as a

triangular-shaped field over the *P–T* range of ~6.9–11.0 kbar, ~920–1140. The peak

field is bound to lower temperature by the absence of orthopyroxene and to lower

pressure by the appearance of sillimanite. The post-peak mineral biotite occurs to lower

temperature than the peak assemblage field. The *P–T* pseudosection, contoured for the

modal abundance ('modes') of some phases, and the ZIR concentration in ppm, is

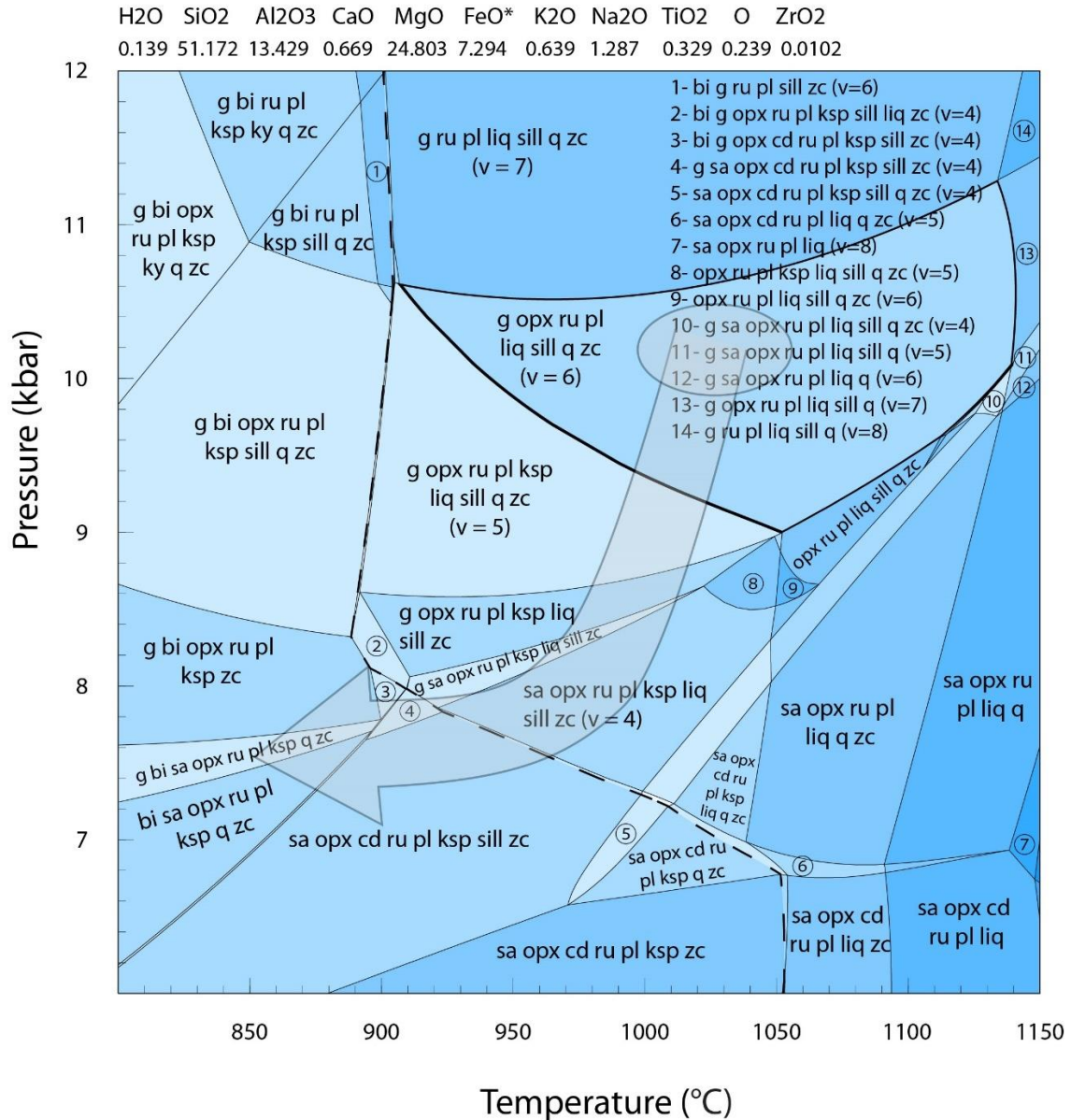shown in Fig. 12. ZIR concentration increases with increasing temperature.

PT AK-6

H2O   SiO2   Al2O3   CaO   MgO   FeO*   K2O   Na2O   TiO2   O   ZrO2
0.572 82.809 6.716   0.507 2.605 1.869   2.464 2.245   0.182 0.014 0.016

Mineral assemblage fields:

1- g bi ksp liq sill q zc (v=6)
2- g opx ilm ru ksp liq sill q zc (v=4)
3- sa opx ilm ksp liq q zc (v = 6)
4- opx ilm ksp liq q zc (v=7)
5- opx ilm ksp liq q (v=8)
6- sa opx ilm ru ksp liq q zc (v=5)
7- opx ilm ru ksp liq q zc (v=6)
8- opx ilm ru ksp liq q (v=7)
9- opx ru ksp liq q zc (v=7)
10- g ksp liq q zc (v=8)
11- g ru ksp liq q (v=8)

Figure 11 Calculated *P–T* pseudosection graphically representing changes in mineralogy for the composition of sample AK-6 across *P–T* space. Abbreviations: bi = biotite; ilm = ilmenite; g = garnet; ksp = K-feldspar; ky = kyanite; liq = silicate melt; opx = orthopyroxene; q = quartz; ru = rutile; sa = sapphirine; sill = sillimanite; zc = zircon. The composition (in mole%) used to calculate the pseudosection is provided above the diagram. FeO* = FeO + 2 × 'O'. The field highlighted in bold represents the peak field, and as such the *P–T* path (arrow) must begin within that field from peak *P–T* conditions (ellipse). By comparison with the *P–T* path of samples AK-3 and AK-5, which are from the same locality, the *P–T* path can be broadly constrained. Due to few retrograde minerals and reaction microstructures in this sample, determination of a retrograde path relies more heavily on the *P–T* paths for other rocks from the same locality.
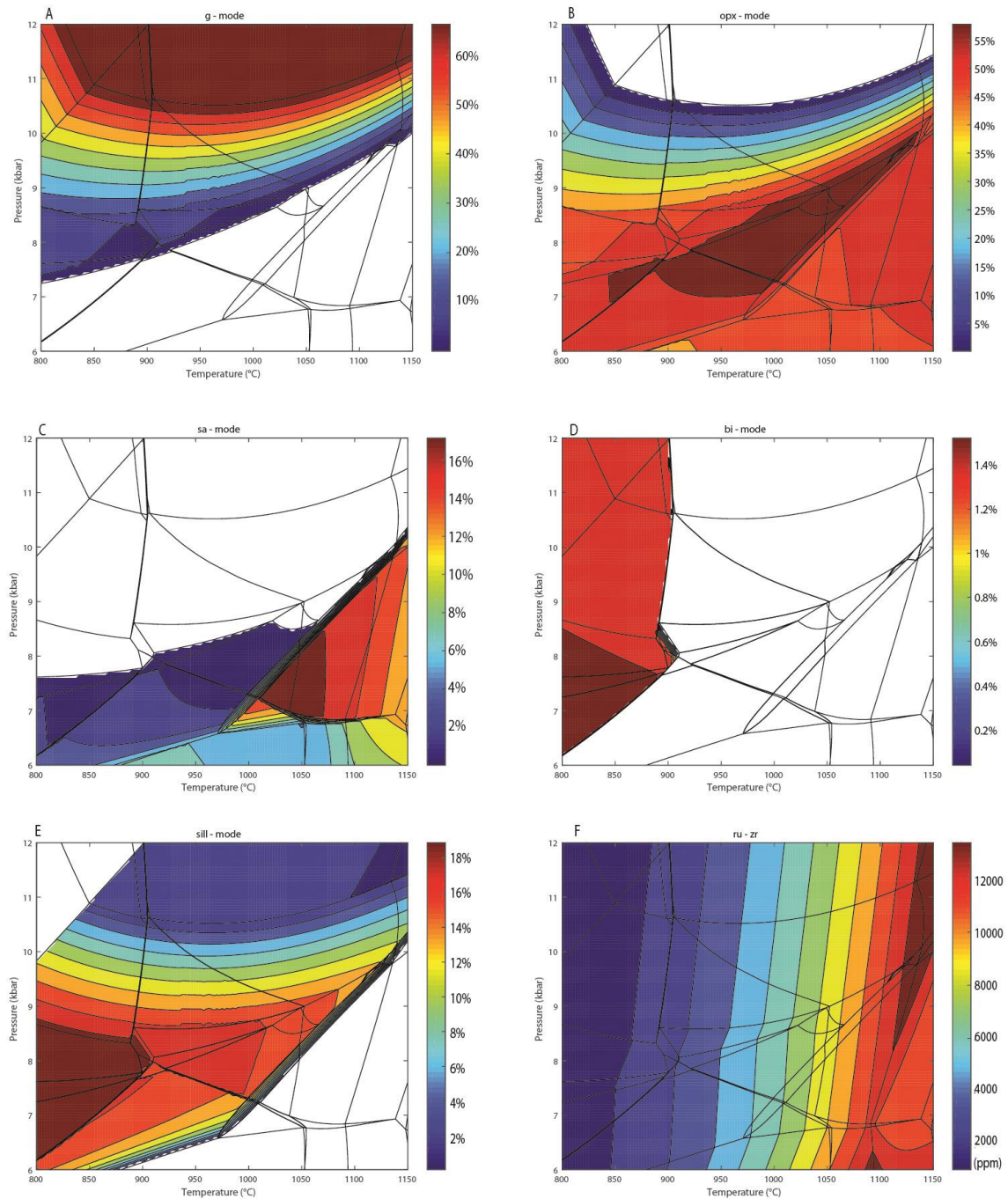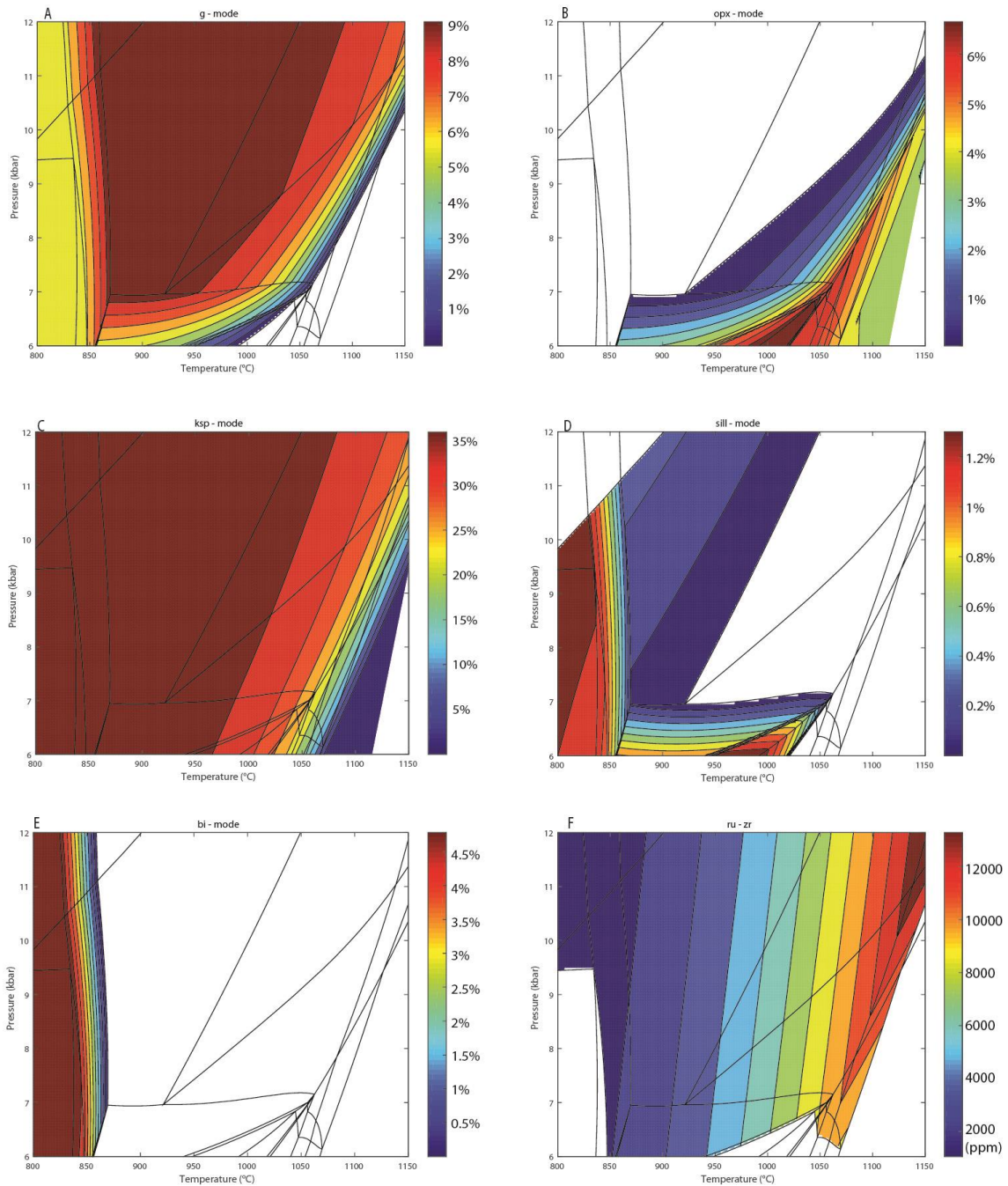
Figure 12 TCInvestigator outputs for the *P–T* pseudosection for sample AK-6 graphically representing: A–E: changes in modal proportions of key minerals as a function of pressure–temperature; F: Zirconium concentration in rutile in ppm as a function of pressure–temperature, showing ZIR to be positively proportional to temperature and negatively proportional to pressure. White space represents regions of *P–T* space in which the mineral being represented is not stable.

R31180
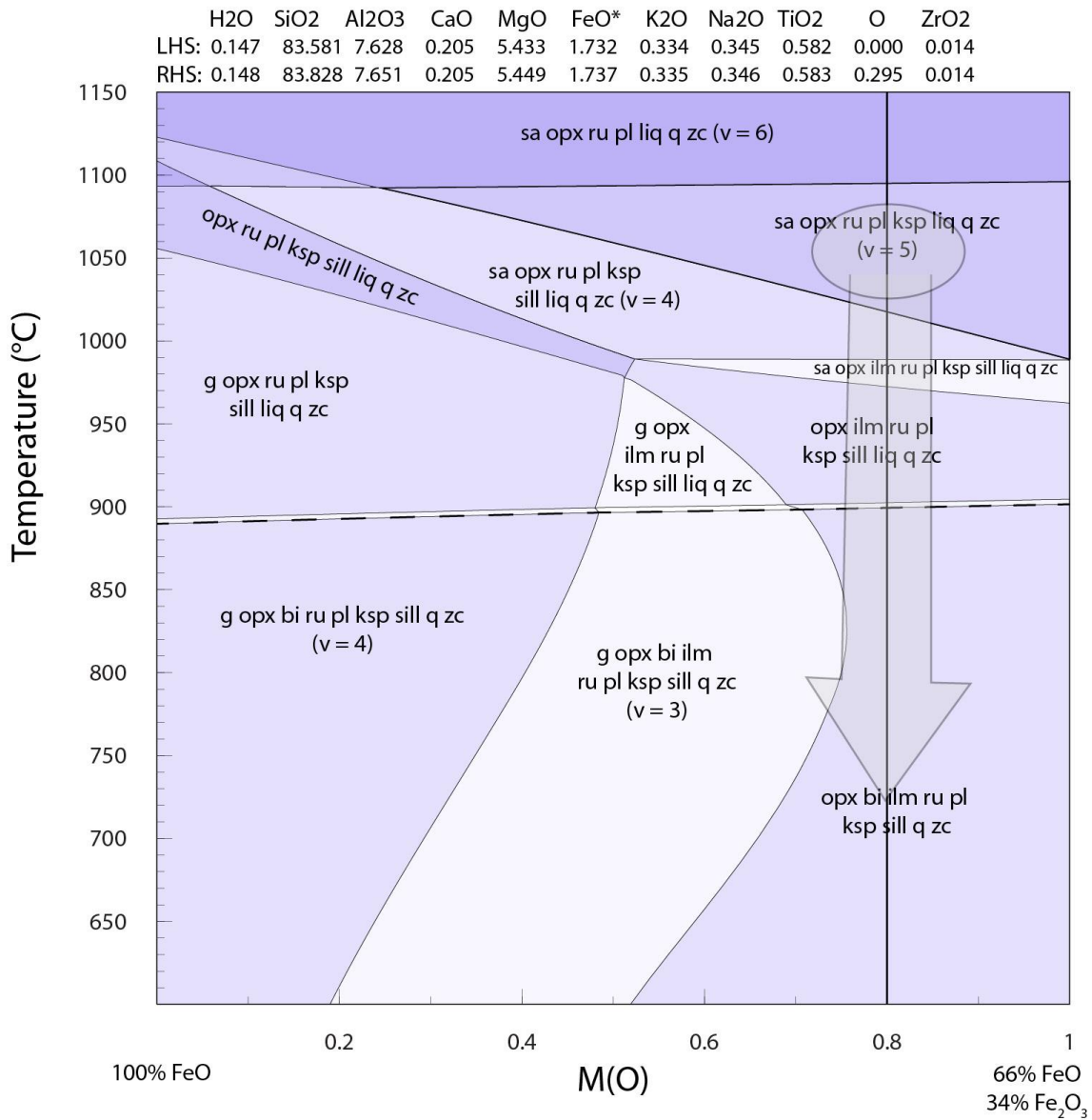
Figure 13 Calculated T–M_O **pseudosection at 8.5 kbar for sample R31180. Abbreviations: bi = biotite; ilm = ilmenite; g = garnet; ksp = K-feldspar; liq = silicate melt; opx = orthopyroxene; pl = plagioclase; q = quartz; ru = rutile; sa = sapphirine; sill = sillimanite; zc = zircon. The compositions (in mole%) used to calculate the pseudosection are provided above the diagram, where the top line represents that at** M**=0 (left-hand side) and the bottom line represents that at** M**=1 (right-hand side). FeO* = FeO + 2 × 'O'. This shows how phase assemblages change with varying oxidation state in the rock. From this diagram, an oxidation state can be chosen on the basis of mineralogy in the rock (bold vertical line at** M_O **= 0.8). Due to the isobaric nature of cooling in the Napier Complex (see discussion), the** P–T **path for R31180 can be presented on this diagram.**

The T–M_O pseudosection calculated at 8.5 kbar for sample R31180 is shown in Fig. 13.

The peak assemblage of quartz–sapphirine–mesoperthitic K-feldspar–rutile–melt does

not appear in the diagram. Instead, orthopyroxene- and/or sillimanite- and/or garnet-bearing assemblages occur. The reasons for these minerals occurring along with the peak minerals in the calculated diagram are provided in the Discussion. On this basis, an oxidation state and composition corresponding to that at $M_O = 0.80$ was chosen, and the peak field (with orthopyroxene) is outlined by bold lines. This oxidation state does not allow garnet to be stable at any temperature at 8.5 kbar but does allow sillimanite stability at lower temperature, faithful to observations from the rock.

SEM and MLA maps

SEM and MLA maps (Figs. 14–17) provide a framework that allowed rutile grains to be analysed as a function of microstructural location (inclusion versus grain boundary) and with different relationships to zircon (internally or externally exsolved zircon, proximal to or contacting xenocrystic zircon, or in locations sparsely populated with zircon). The vast majority of rutile grains in AK-3 are located at grain boundaries (Fig. 14). A greater proportion of rutile grains occur as inclusions in AK-5 compared to AK-3 (compare Fig. 14 to 15). Most rutile in AK-6 and R31180 occurs at grain boundaries (Figs. 16, 17). The maps also allowed the abundances of rutile and zircon and the ratio of the two values to be calculated for each sample (Table 1). Sample AK-3 had the most total zircon and the lowest rutile:zircon ratio (1.13:1.00). Samples AK-5 and AK-6 had equally low zircon concentrations (0.02% of total area of thin section); however, due to the abundance of rutile in sample AK-5, it had the highest rutile:zircon ratio (32:1) of all samples (Table 1). AK-6 has the second lowest rutile:zircon ratio (5:1). Sample R31180 had the second highest rutile:zircon ratio (12.75:1).

Table 1 Rutile:zircon ratios for all samples as calculated using MLA maps to determine the total amount of rutile and zircon in the thin section.

Sample	Total area rutile (%)	Total area zircon (%)	Normalised rutile area	Normalised zircon area	Ratio Rutile:zircon
AK3	0.17	0.15	53.125	46.875	1.13
AK5	0.64	0.02	96.970	3.030	32.00
AK6	0.10	0.02	83.333	16.667	5.00
R31180	0.51	0.04	92.727	7.273	12.75

Figure 14 (A) BSE image mosaic of a part of sample AK-3, with the MLA map (colours) superimposed on top, showing the spatial distribution and location of monazite (white), zircon (blue) and rutile (red). The full thin section map images are provided in Appendix E. The sample is dominated by symplectic intergrowths of sapphirine + orthopyroxene ± plagioclase; (B) MLA image mosaic of sample AK-3 that allows the abundance of zircon and rutile to be seen more clearly. Rutile is depicted by red, and zircon by blue.
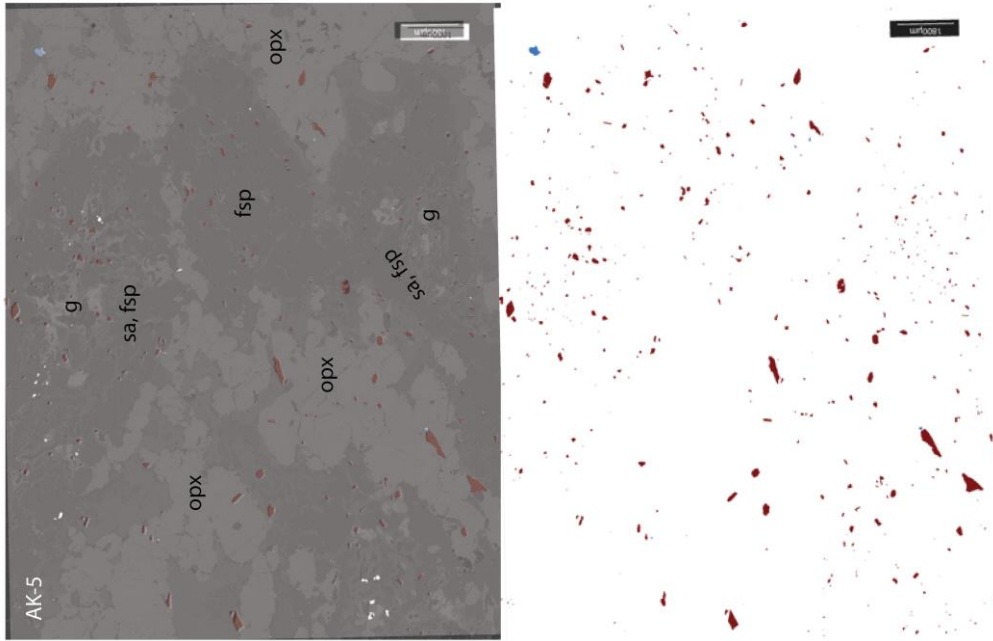
Figure 15 (A) BSE image mosaic of a part of sample AK-5, with the MLA map (colours) superimposed on top, showing the spatial distribution and location of monazite (white), zircon (blue) and rutile (red). The full thin section map images are provided in Appendix E. The part of the sample shown is dominated by orthopyroxene, feldspar and quartz; (B) MLA image mosaic of sample AK-5 that allows the abundance of zircon and rutile to be seen more clearly. Rutile is depicted by red, and zircon by blue.
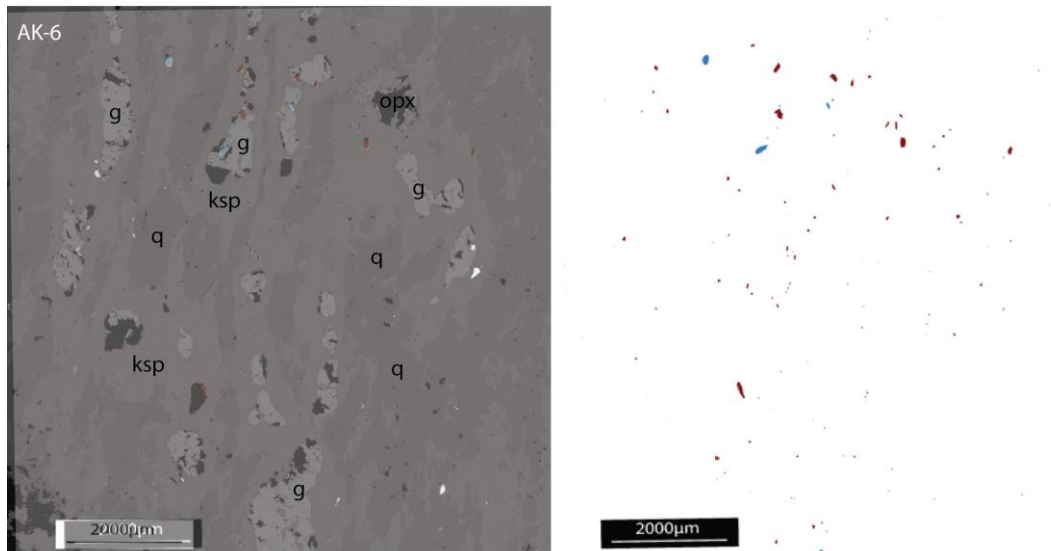
Figure 16 (A) BSE image mosaic of a part of sample AK-6, with the MLA map (colours) superimposed on top, showing the spatial distribution and location of monazite (white), zircon (blue) and rutile (red). Black is holes in the slide. The full thin section map images are provided in Appendix E. The part of the sample shown is dominated by quartz and garnet that is surrounded by K-feldspar; (B) MLA image mosaic of sample AK-6 that allows the abundance of zircon and rutile to be seen more clearly. Rutile is depicted by red, and zircon by blue.
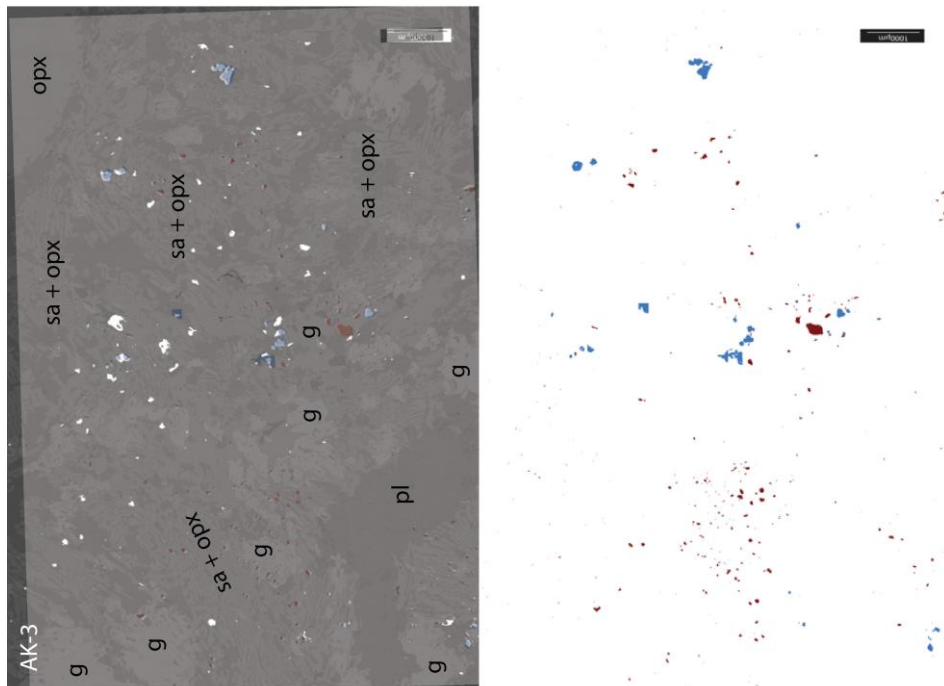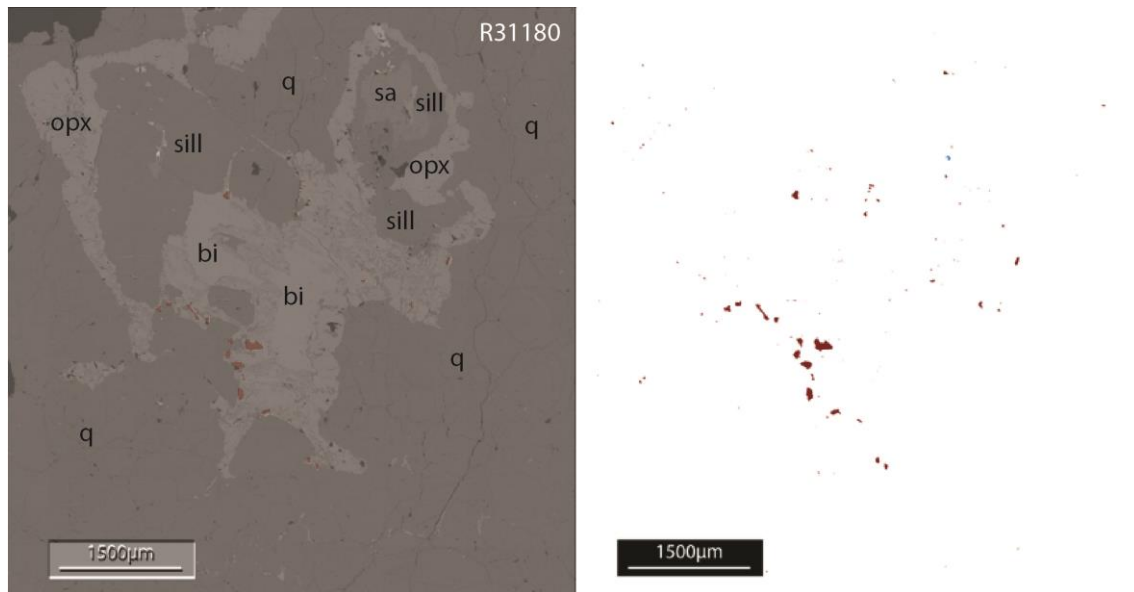
Figure 17 (A) BSE image mosaic of a part of sample R31180, with the MLA map (colours) superimposed on top, showing the spatial distribution and location of monazite (white), zircon (blue) and rutile (red). Black is holes in the slide. The full thin section map images are provided in Appendix E. Quartz and a rare grain of biotite dominate the part of the sample shown; (B) MLA image mosaic of sample R31180 that allows the abundance of zircon and rutile to be seen more clearly. Rutile is depicted by red, and zircon by blue.

Trace Element concentrations and thermometry and distance between rutile and xenocrystic zircon

ZIR CONCENTRATION DATA

Rutile grains from the two microstructural locations and with a variety of relationships with zircon were analysed via EPMA from the four samples. The full dataset of analyses is provided in Appendix B.

Forty-seven spot analyses were obtained on rutile grains from sample AK-3 via EPMA (Fig. 18, Table 2). Two of these analyses came from rutile classified as inclusions and forty-five were classified as grain boundary-hosted. Sixty-two analyses were obtained from rutile grains in sample AK-5 (Fig. 19, Table 2). Fifteen of these data came from rutile grains classified as inclusions, and forty-seven from grains classified as grain boundary-hosted. Eighty-one analyses were obtained from rutile grains in sample AK-6

30

(Fig. 20, Table 2), with seventeen from inclusion of rutile grains, and sixty-four from

grain boundary hosted grains. Seventy analyses were performed on rutile grains from

sample R31180 (Fig. 21, Table 2), with seven of those coming from rutile grains held as

inclusions and sixty-three from grains at grain boundaries. In AK-3, AK-5, AK6

inclusion grains had a higher mean ZIR concentration than grain-boundary located

grains (Table 2), whereas in sample R31180 the opposite held. The concentration data

was plotted as a function of distance from the nearest xenocrystic zircon grain (Figs.

18–21c,d,g,h,k,l).

Table 2 Mean ZIR concentrations for all samples classified by microstructural setting

Sample	Mean ZIR concentration (All data) (ppm)	Mean ZIR concentration (inclusion) (ppm)	Mean ZIR concentration (grain boundary) (ppm)
AK-3	1498.66 ± 52.88 (n=47)	1865.86 ± 54.78 (n=2)	1482.34 ± 52.80 (n=45)
AK-5	1269.41 ± 50.58 (n=62)	1330.08 ± 50.56 (n=15)	1250.05 ± 50.59 (n=47)
AK-6	3547.06 ± 65.04 (n=81)	3942.38 ± 66.38 (n=17)	3442.05 ± 64.68 (n=64)
R31180	587.94 ± 45.82 (n=70)	422.97 ± 43.71 (n=7)	606.27 ± 46.05 (n=63)

ZR REINTEGRATION

BSE images of analysed rutile grains were examined for evidence of zircon exsolution,

and, where possible, Zr in exsolved zircon was reintegrated back into rutile. After all

possible reintegrations were performed, the ZIR concentration data was replotted (Figs.

17–20b,f j), including against the distance from the nearest xenocrystic zircon grain

(Figs. 17-20d,h,l).

Of the forty-seven rutile grains analysed in AK-3, fifteen had visible zircon exsolution

and reintegrations were performed for these grains (Table 3). Thirty-six of sixty-two

data from sample AK-5 could be reintegrated (Table 3), namely seven of fifteen rutile

inclusions, and twenty-nine of the forty-seven grain boundary-hosted grains. Eleven of

eighty-one data from AK-6 could be reintegrated, namely two of seventeen rutile

inclusions, and nine of the sixty-four grain boundary-hosted grains (Table 3). Thirty-two of seventy data from sample R31180 could be reintegrated, namely one of seven inclusions and thirty-one of the sixty-three grain boundary-hosted grains (Table 3). Grain boundary-located grains had a higher mean ZIR concentration than inclusion grains after reintegration for all samples (Table 3; contrast to Table 2).

Table 3 Post-reintegration mean ZIR concentrations for all samples classified by microstructural setting

Sample	Mean reintegrated ZIR concentration (All data) (ppm)	Mean reintegrated ZIR concentration (inclusion) (ppm)	Mean reintegrated ZIR concentration (grain boundary) (ppm)
AK-3	3648.86 ± 112.696 (n=47, including 15 reintegrated grains)	1865.86 ± 54.782 (n=2; no reintegrated grains)	3728.11 ± 116.173 (n=45, including 15 reintegrated grains)
AK-5	4968.11 ± 171.973 (n=62, including 36 reintegrated grains)	3946.28 ± 127.666 (n=15, including 7 reintegrated grains)	5294.22 ± 189.211 (n=47, including 29 reintegrated grains)
AK-6	5310.35 ± 91.136 (n=81, including 11 reintegrated grains)	4896.24 ± 82.546 (n=17, including 2 reintegrated grains)	5420.35 ± 93.360 (n=64, including 9 reintegrated grains)
R31180	3101.41 ± 205.062 (n=70, including 32 reintegrated grains)	846.62 ± 75.242 ppm (n=7, including 1 reintegrated grain)	3351.94 ± 220.366 (n=64, including 31 reintegrated grains)

Figure 18 Ppm Zr results for rutile grains from sample AK-3. Results have been separated into three categories: graphs including all data (n = 47) (a, b, c, d); graphs including only data from inclusions of rutile in other minerals (n = 2) (e, f, g, h); graphs including only data from grain boundary-hosted rutile (n = 45) (i, j, k, l). The first row of graphs summarises ppm Zr values without reintegrating Zr from exsolved zircon back into any rutile grains. The second row of graphs shows the same data, but with reintegration of exsolved Zr (in zircon) into rutile done where possible (see Table 3). The third row of graphs shows the data as a function of rutile grain distance from xenocrystic zircon, and the fourth shows the same data but with reintegration of Zr from exsolved zircon into rutile where possible (see Table 3).
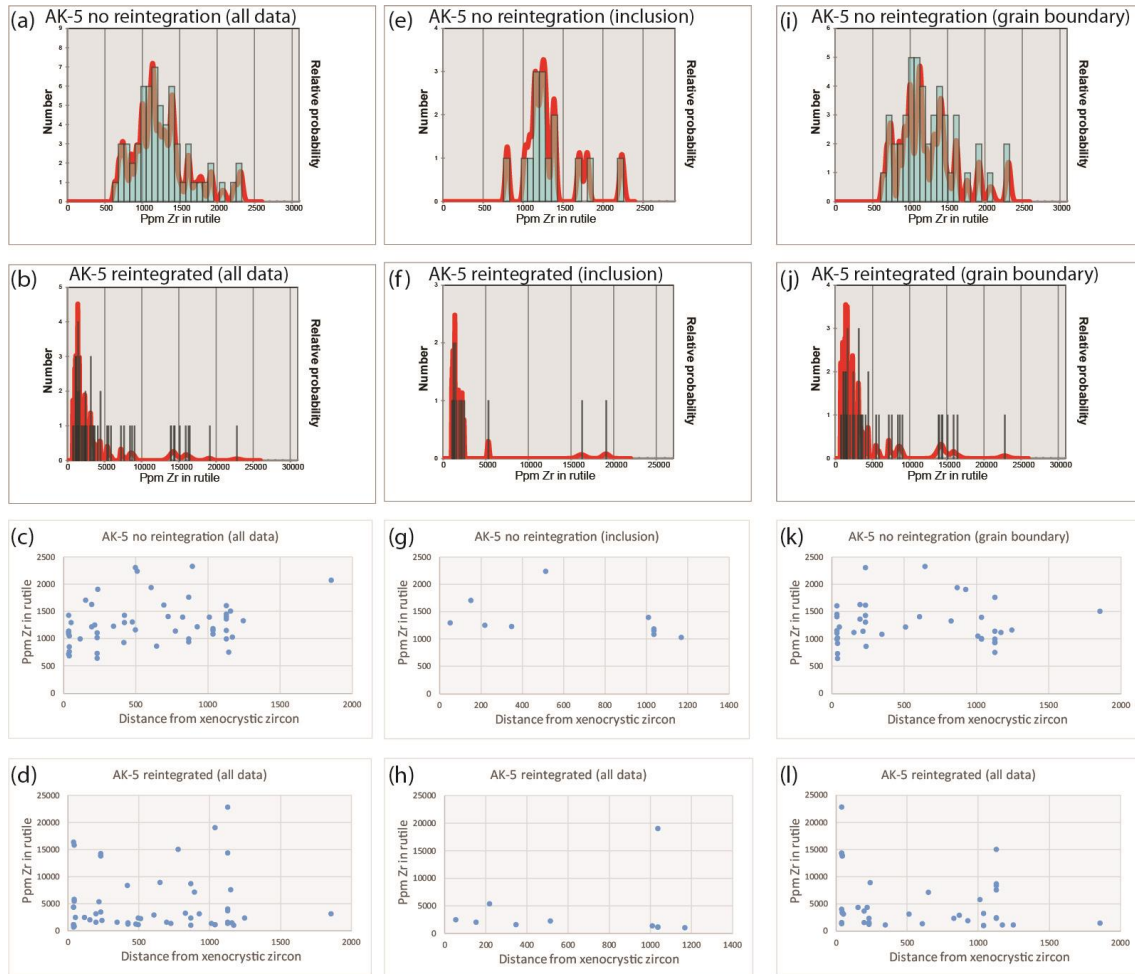
Figure 19 Ppm Zr results for rutile grains from sample AK-5. Results have been separated into three categories: graphs including all data (n = 62) (a, b, c, d); graphs including only data from inclusions of rutile in other minerals (n = 15) (e, f, g, h); graphs including only data from grain boundary hosted rutile (n = 47) (i, j, k, l). The first row of graphs summarises ppm Zr values without reintegrating Zr from exsolved zircon back into any rutile grains. The second row of graphs shows the same data, but with reintegration of exsolved Zr (in zircon) into rutile done where possible (see Table 3). The third row of graphs shows the data as a function of rutile grain distance from xenocrystic zircon, and the fourth shows the same data but with reintegration of Zr from exsolved zircon into rutile where possible (see Table 3).
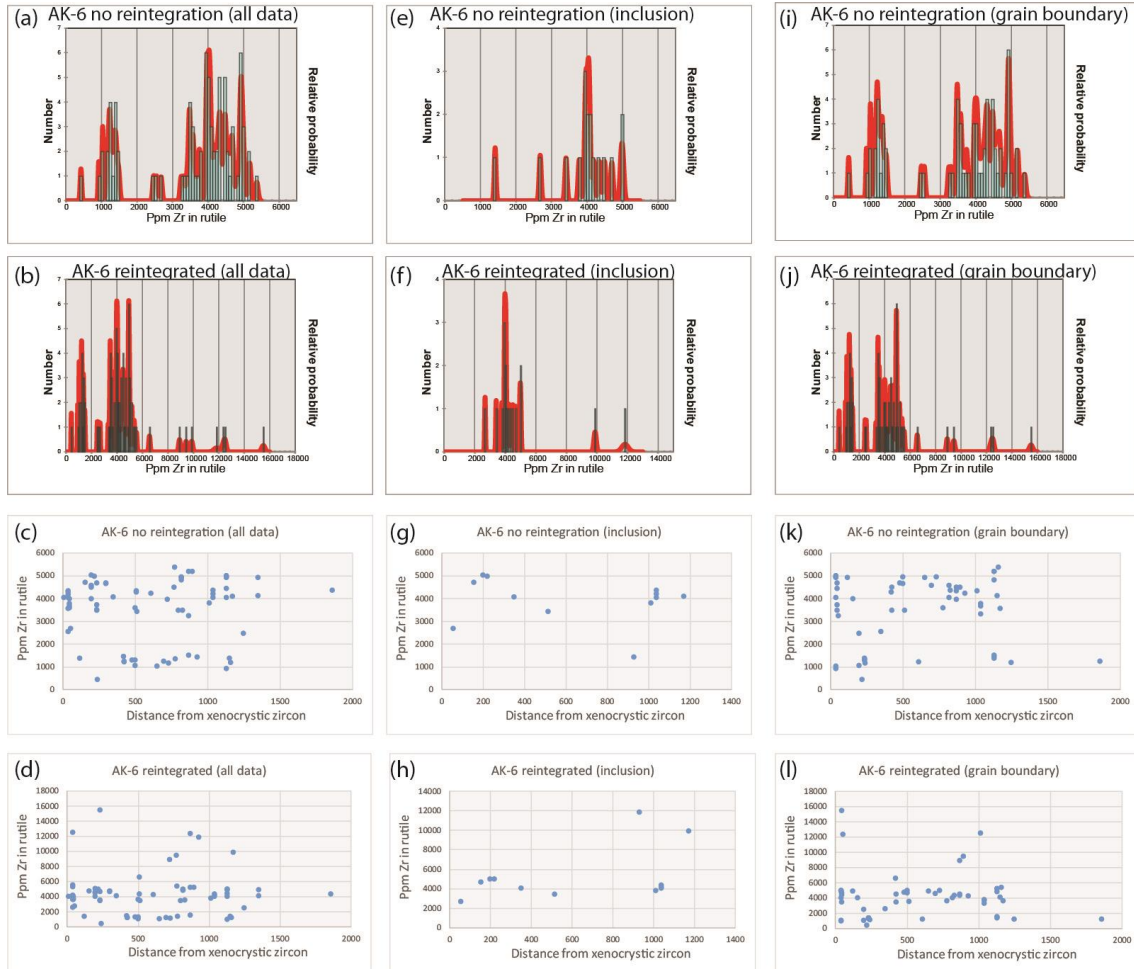
Figure 20 Ppm Zr results for rutile grains from sample AK-6. Results have been separated into three categories: graphs including all data (n = 81) (a, b, c, d); graphs including only data from inclusions of rutile in other minerals (n = 17) (e, f, g, h); graphs including only data from grain boundary hosted rutile (n = 64) (i, j, k, l). The first row of graphs summarises ppm Zr values without reintegrating Zr from exsolved zircon back into any rutile grains. The second row of graphs shows the same data, but with reintegration of exsolved Zr (in zircon) into rutile done where possible (see Table 3). The third row of graphs shows the data as a function of rutile grain distance from xenocrystic zircon, and the fourth shows the same data but with reintegration of Zr from exsolved zircon into rutile where possible (see Table 3).
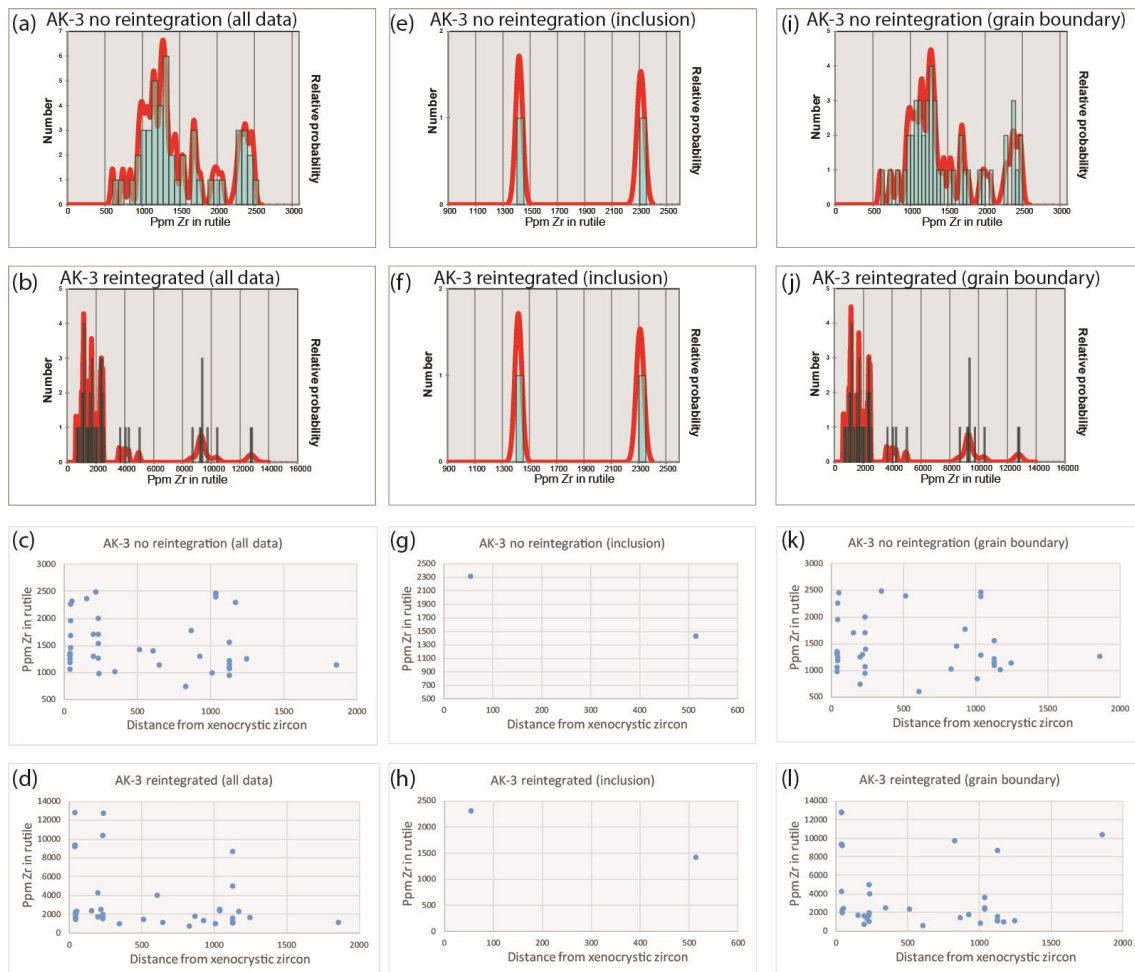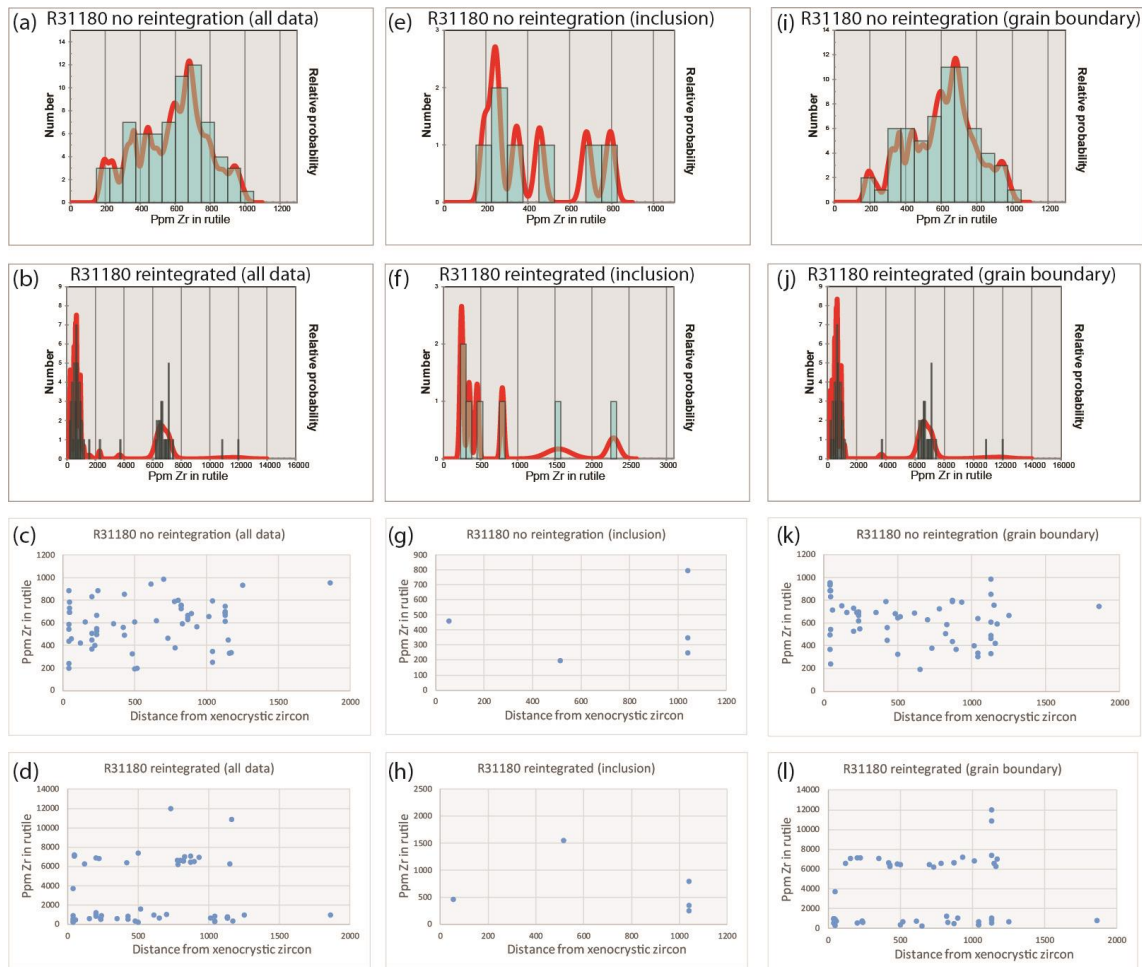
Figure 21 Ppm Zr results for rutile grains from sample R31180. Results have been separated into three categories: graphs including all data (n = 70) (a, b, c, d); graphs including only data from inclusions of rutile in other minerals (n = 7) (e, f, g, h); graphs including only data from grain boundary hosted rutile (n = 63) (i, j, k, l). The first row of graphs summarises ppm Zr values without reintegrating Zr from exsolved zircon back into any rutile grains. The second row of graphs shows the same data, but with reintegration of exsolved Zr (in zircon) into rutile done where possible (see Table 3). The third row of graphs shows the data as a function of rutile grain distance from xenocrystic zircon, and the fourth shows the same data but with reintegration of Zr from exsolved zircon into rutile where possible (see Table 3).

ZIR THERMOMETRY

ZIR thermometry results are shown in Table 4 (To07 thermometer). Prior to

reintegration of exsolved Zr (Table 3), all samples but AK-6 showed a single peak in

temperature distribution and sample AK-6 showed a bimodal distribution (Figs. 22–25

a, e, i). Sample AK-3 shows temperature peaks corresponding to ~700–800 °C (Fig. 22;

Table 4), sample AK-5 shows temperature peaks corresponding to ~700–800 °C (Fig.

23; Table 4), sample AK-6 shows a bimodal distribution, with a lower peak at ~750–

800°C, and an upper peak at ~900–950 °C (Fig. 24; Table 4), and sample R31180

shows a single peak at ~650–700 °C (Fig. 25; Table 4).

After Zr reintegration, temperature distributions for all samples were bimodal. All

samples saw significant increases in ZIR temperatures after reintegration (compare

diagrams (a) and (b) in Fig. 22–25). Sample AK-3 shows a lower peak of ~750–850 °C

and upper peak of ~1000–1100 °C (Fig. 21; Table 5), sample AK-5 shows a lower peak

of ~750–900 °C and upper peak of ~1125 °C (Fig. 23; Table 5), sample AK-6 shows a

lower peak of ~775 °C and upper peak of ~900–950 °C (Fig. 24; Table 5) and sample

R31180 shows a lower peak of ~700–750 °C and upper peak of ~975 °C (Fig. 25; Table

5).

Table 4 Summary of mean temperatures using the To07 thermometer for each sample classified by 3 categories: all data, data from rutile grains classified as inclusions, and data from rutile grains from grain boundaries. No Zr reintergration was performed for calculation of these temperatures.

Sample	Mean temperature (To07) (All data) (°C)	Mean temperature (To07) (inclusion) (°C)	Mean temperature (To07) (grain boundary) (°C)
AK-3	790 ± 30 (n=47)	814 ± 25 (n=2)	789 ± 30 (n=45)
AK-5	773 ± 32 (n=62)	777 ± 31 (n=15)	771 ± 33 (n=47)
AK-6	892 ± 19 (n=81)	906 ± 16 (n=17)	888 ± 20 (n=64)
R31180	698 ± 60 (n=70)	669 ± 83 (n=7)	701 ± 58 (n=63)

As sample AK-3 is a quartz absent rock the aSiO$_2$ value for this rock would be less than

unity. Therefore, the FW07 thermometer was used to present the thermometry data from

sample AK-3 with several different aSiO$_2$ values (Fig. 26). As aSiO$_2$ decreases, a

decrease in ZIR temperatures is observed (Fig. 26).

Figure 22 ZIR thermometry results for rutile grains from sample AK-3 using the To07 thermometer. Results have been separated into three categories: graphs including all data (n = 47) (a, b, c, d); graphs including only data from inclusion hosted rutile (n = 2) (e, f, g, h); graphs including only data from grain boundary hosted rutile (n = 45) (i, j, k, l). The first row of graphs summarises ZIR temperatures without reintegrating Zr from exsolved zircon back into any rutile grains. The second row of graphs shows the same data, but with reintegration of exsolved Zr (in zircon) into rutile done where possible (see Tables 6 & 7). The third row of graphs shows the data as a function of rutile grain distance from xenocrystic zircon, and the fourth shows the same data but with reintegration of Zr from exsolved zircon back into rutile where possible (see Table 4).
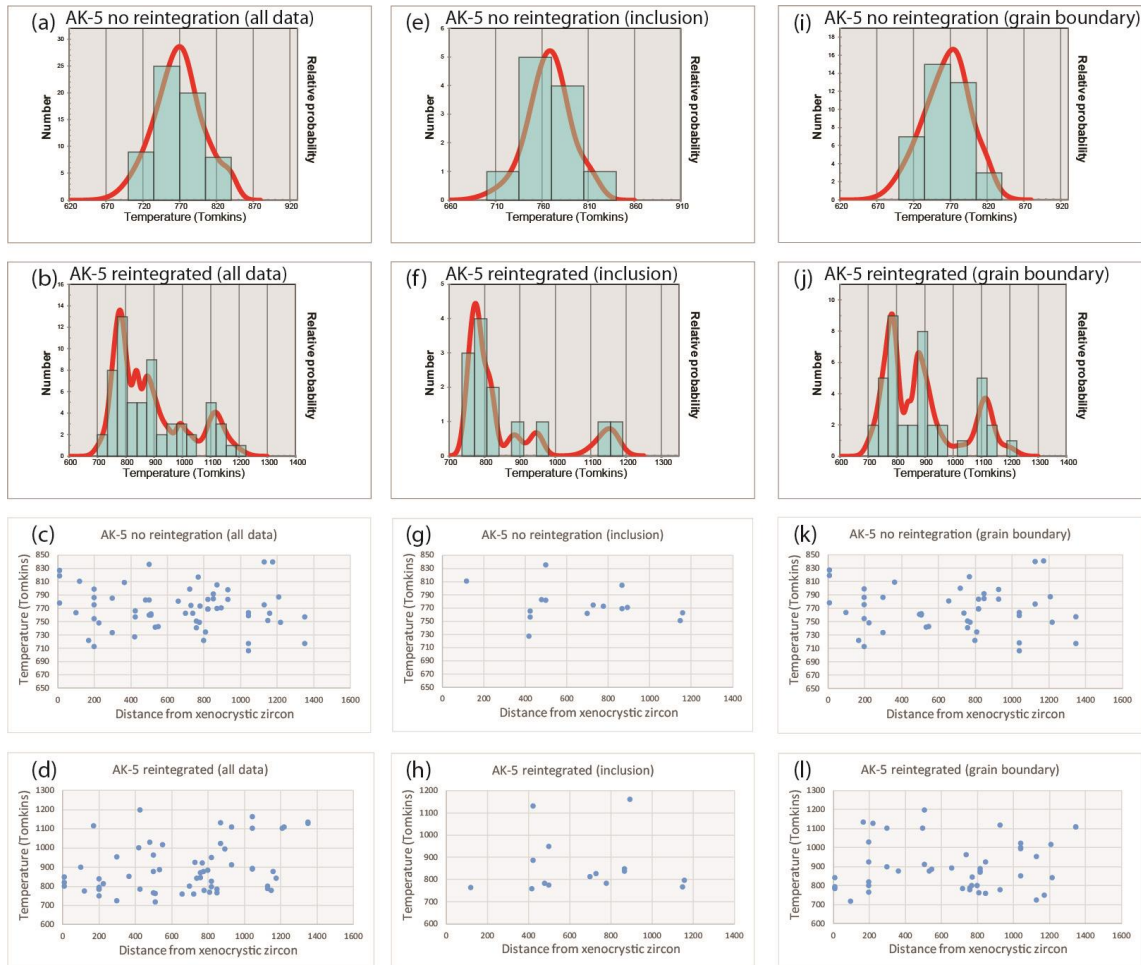
Figure 23 ZIR thermometry results for rutile grains from sample AK-5 using the To07 thermometer. Results have been separated into three categories: graphs including all data (n = 62) (a, b, c, d); graphs including only data from inclusion hosted rutile (n = 15) (e, f, g, h); graphs including only data from grain boundary hosted rutile (n = 47) (i, j, k, l). The first row of graphs summarises ZIR temperatures without reintegrating zirconium from exsolved zircon back into any rutile grains. The second row of graphs shows the same data, but with reintegration of exsolved Zr (in zircon) into rutile done where possible (see Tables 6 & 7). The third row of graphs shows the data as a function of rutile grain distance from xenocrystic zircon, and the fourth shows the same data but with reintegration of Zr from exsolved zircon back into rutile where possible (see Table 4).
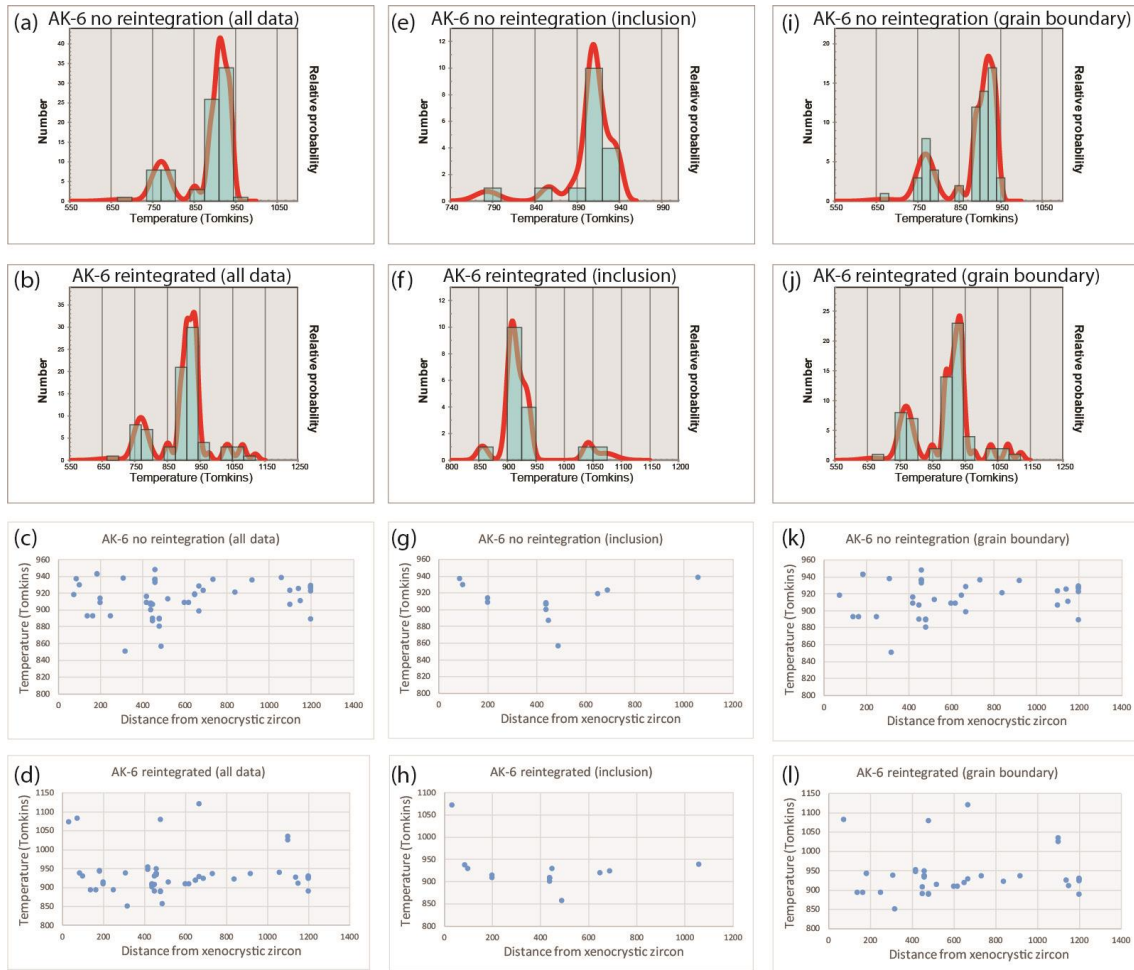
Figure 24 ZIR thermometry results for rutile grains from sample AK-6 using the To07 thermometer. Results have been separated into three categories: graphs including all data (n = 81) (a, b, c, d); graphs including only data from inclusion hosted rutile (n = 17) (e, f, g, h); graphs including only data from grain boundary hosted rutile (n = 64) (i, j, k, l). The first row of graphs summarises ZIR temperatures without reintegrating zirconium from exsolved zircon back into any rutile grains. The second row of graphs shows the same data, but with reintegration of exsolved Zr (in zircon) into rutile done where possible (see Tables 6 & 7). The third row of graphs shows the data as a function of rutile grain distance from xenocrystic zircon, and the fourth shows the same data but with reintegration of Zr from exsolved zircon back into rutile where possible (see Table 4).
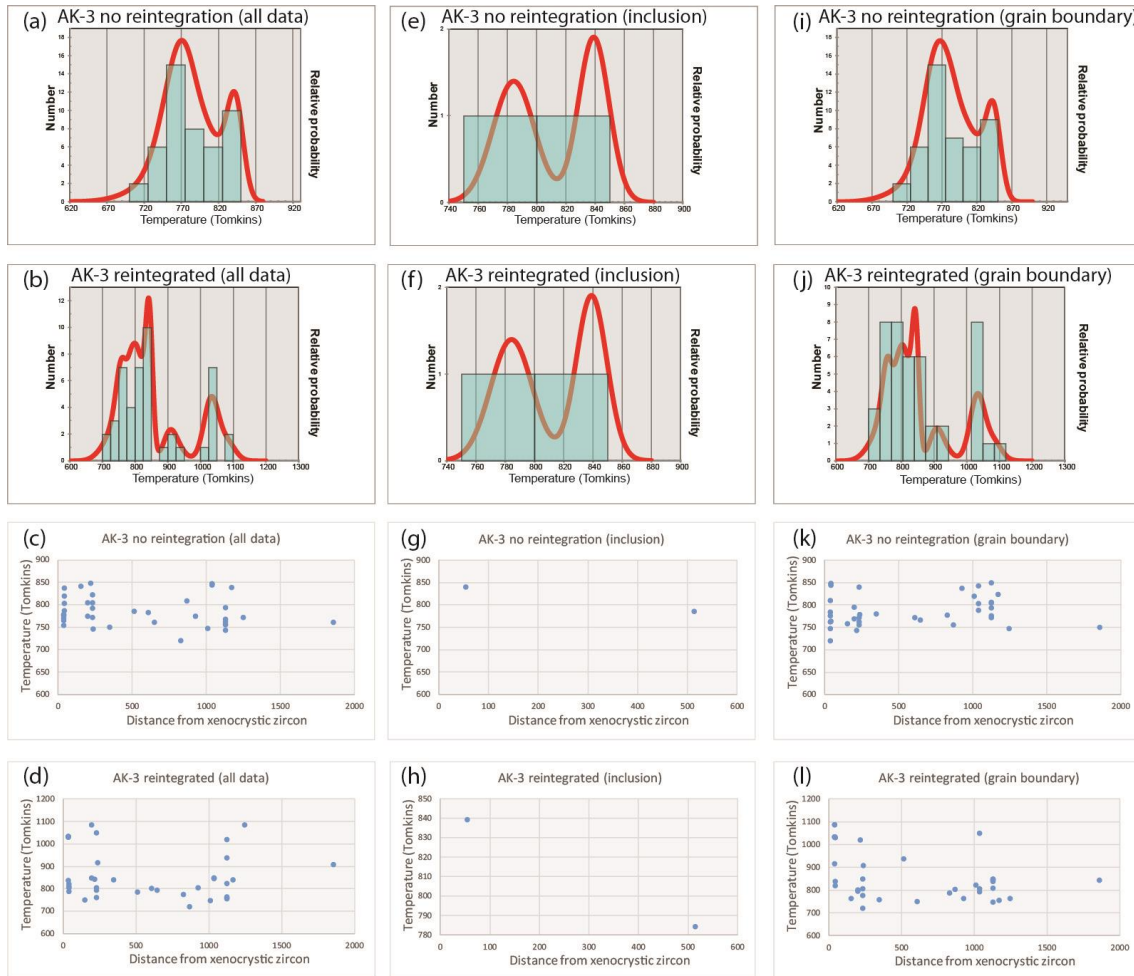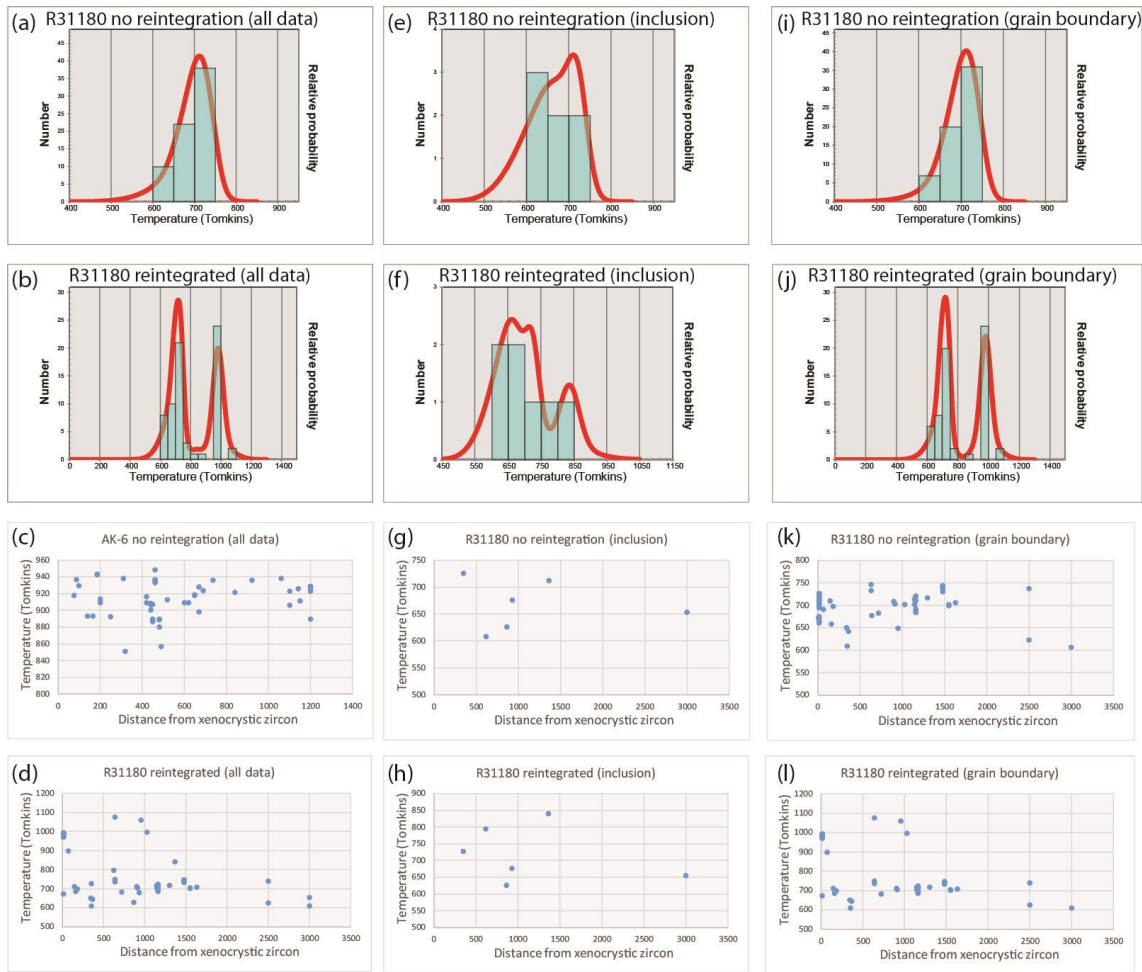
Figure 25 ZIR thermometry results for rutile grains from sample R31180 using the To07 thermometer. Results have been separated into three categories: graphs including all data (n = 70) (a, b, c, d); graphs including only data from inclusion hosted rutile (n = 7) (e, f, g, h); graphs including only data from grain boundary hosted rutile (n = 63) (i, j, k, l). The first row of graphs summarises ZIR temperatures without reintegrating zirconium from exsolved zircon back into any rutile grains. The second row of graphs shows the same data, but with reintegration of exsolved Zr (in zircon) into rutile done where possible (see Tables 6 & 7). The third row of graphs shows the data as a function of rutile grain distance from xenocrystic zircon, and the fourth shows the same data but with reintegration of Zr from exsolved zircon into rutile where possible (see Table 4).
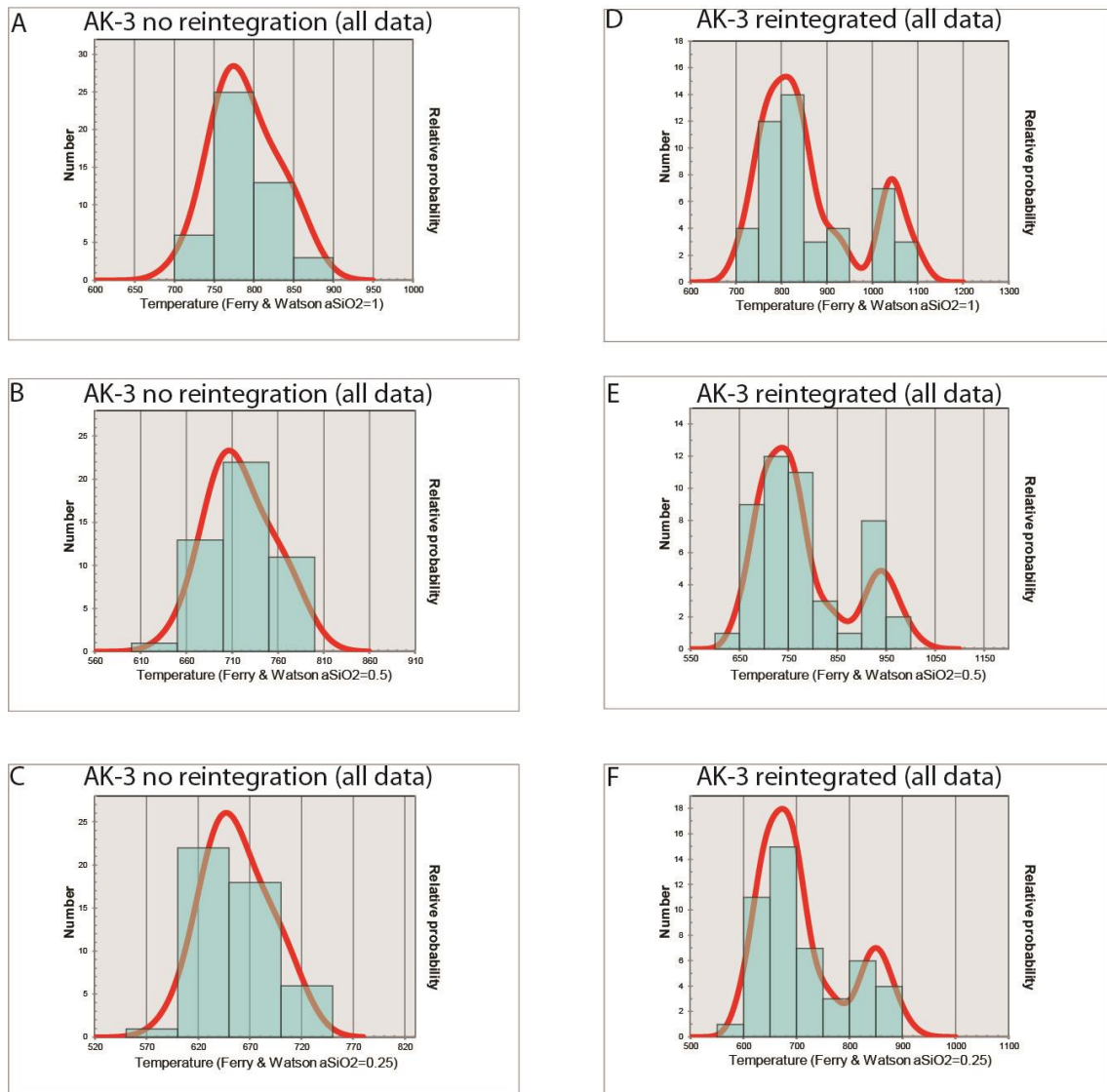
Figure 26 Sample AK-3 is quartz-absent, so thermometry for the sample requires *a*SiO₂ values less than unity. The FW07 thermometer allows for *a*SiO₂ to be varied. As *a*SiO₂ decreases (simulating the sample becoming progressively more silica-deficient) the ZIR temperatures decrease: compare C to B to A, and F to E to D.

DISCUSSION

Phase Equilibria Forward Modelling

Phase diagrams were calculated to quantify that the studied rocks reached UHT

conditions at the peak of metamorphism, constrain their *P–T* path, and calculate trends

and absolute ZIR contents as a function of *P–T–X* space (Kelsey & Powell, 2011;

Skrzypek et al., 2012), for the purpose of comparing and interpreting calculated to

measured ZIR data (Skrzypek et al., 2012). *P–T* paths for the rocks are defined by integrating the petrographic observations of interpreted prograde, peak and retrograde minerals with the trends in changing mineral abundance in *P–T* space as calculated by TCInvestigator.

AK-3

Sample AK-3 has a peak mineral assemblage of biotite$_1$–garnet$_1$–orthopyroxene$_1$–spinel$_1$–plagioclase–K-feldspar–rutile–melt, where coarse-grained spinel is rare. Due to the scarcity of spinel, the peak metamorphic conditions must lie close to (or within) the spinel-bearing field, as depicted by the semi-transparent ellipse on Fig. 7, at P–T conditions of ~10.5 kbar and 1000–1050 °C. The size of the ellipse is reasonably large to convey uncertainty in the exact peak *P–T* conditions. Sapphirine–orthopyroxene symplectites are interpreted to be the first developed retrograde products, followed by plagioclase, biotite, sillimanite and, lastly, garnet. From the trends in mineral abundance in the contoured pseudosections, Fig. 8, the retrograde *P–T* path as shown on Fig. 7 is deduced, satisfying all petrographic observations. Dasgupta et al. (1994) interpreted a similarly shaped *P–T* path in their study of rocks from Anakapalle. I have not attempted to propose a prograde *P–T* path for any sample, as this is uncertain in granulite facies rocks (White & Powell, 2002). However, if the early metamorphic record of rocks in the Eastern Ghats Province holds for Anakapalle, the prograde *P–T* path (in the granulite facies) likely involved an increase in pressure along an anti-clockwise path (Korhonen et al., 2014). Rare inclusions of sapphirine in relict garnet$_1$ provide circumstantial support for this interpretation. Along the deduced *P–T* path the ZIR concentration decreases from a maximum of ~11,000–12,000 ppm (Figs. 7, 8f; 1060–1070 °C, To07) at the metamorphic peak to ~3000–4000 ppm (Fig. 7, 8f, To07) along the near-isobaric

cooling segment of the *P–T* path at ~7.5–8 kbar. These ZIR values cover some of the

measured ZIR data for AK-3 (reintegrated data, Fig. 18b), discussed later.

AK-5

Sample AK-5 records a peak mineral assemblage of garnet–orthopyroxene–rutile–

plagioclase–sillimanite–quartz–melt–zircon, constraining peak *P–T* conditions to that

field (Fig. 9). Exact *P–T* conditions within that peak field are difficult to determine, due

to ambiguity in estimating peak mineral abundances. However, as AK-5 is from the

same location as sample AK-3, the peak *P–T* conditions are likely to be shared.

Therefore, I interpret that the peak *P–T* conditions and retrograde *P–T* path for AK-5,

are the same as for AK-3 (Fig. 9). This *P–T* path satisfies the observations from

petrography that orthopyroxene, sapphirine, K-feldspar, plagioclase and cordierite are

all retrograde minerals that increase in abundance down-pressure and/or temperature

(Fig. 10b, c, feldspar and cordierite abundance not shown in Fig. 10), and that the

abundance of garnet decreases down-pressure (Fig. 10a). Sillimanite is problematic in

that its preserved abundance in AK-5 is very low, and almost entirely of retrograde

origin, yet the calculated pseudosection indicates sillimanite abundance should be quite

high (up to ~15–19%). This discrepancy may relate to favourable reactivity of (peak)

sillimanite compared to other minerals (White & Powell, 2011). The ZIR concentrations

are calculated to be ~7,000–9,000 ppm (~990–1030 °C for To07) at the metamorphic

peak, decreasing to ~3000–4000 ppm (~875–910 °C) along the near-isobaric cooling

segment of the retrograde *P–T* path. These lower temperatures are similar to or greater

than the majority of ZIR data from this sample (Fig. 23b), as discussed later.

AK-6

Sample AK-6 has a peak assemblage of orthopyroxene–garnet–quartz–feldspar–rutile–

melt in a mostly quartz–feldspar rock. Due to the low abundance of orthopyroxene in

this sample the peak metamorphic conditions may be close to the orthopyroxene-in-out

line (bold diagonal line from 7 to 11 kbar in Fig. 11). However, following the logic

from sample AK-5, it is reasonable to assume that the peak metamorphic conditions—

and retrograde P–T path—for AK-6 were similar to or the same as those for sample

AK-3. If true, this may mean that either: 1) the composition used for the calculation of

the P–T pseudosection was not hydrous enough. More hydrous compositions would

result in orthopyroxene stability expanding up-pressure (P–M_{H2O} diagram, Appendix F);

and/or 2) that orthopyroxene is actually an early retrograde mineral. In AK-6,

orthopyroxene is separated from garnet by K-feldspar (Figs. 5a, 12a). Therefore,

arguably, orthopyroxene is a peak rather than retrograde mineral that reacted with

garnet to produce K-feldspar (Fig. 11a). The peak metamorphic conditions, depicted by

an ellipse on Fig. 11, are shown at lower pressure than for samples AK-3, AK-5. This is

to convey that orthopyroxene is interpreted to be a peak mineral, rather than indicate

that the peak conditions in AK-6 were different than in AK-3 and AK-5. AK-6 has very

minor ($<<1\%$) sillimanite occurring in the matrix, but its paragenetic significance is

unclear. However, given the presence of a sillimanite-bearing field to lower pressure

than the peak assemblage field, it could be that matrix sillimanite is a minor retrograde

product. From TCInvestigator outputs (Fig. 14), the abundance of sillimanite is

constrained to be very low (Fig. 12d), so if a sillimanite-bearing field was accessed by

the P–T path, the abundance of sillimanite is not expected to be significant. The ZIR

concentrations are calculated to be ~7000–9000 ppm (~990–1030 °C, To07) at the

metamorphic peak, decreasing to ~1000–4000 ppm (~750–910 °C) along the near-

isobaric cooling segment of the retrograde P–T path. This entire temperature range (i.e.

~750–1030 °C) is covered by the spread of ZIR data from this sample (Fig. 25b), as

discussed later.

R31180

Sample R31180 has a peak assemblage of quartz–sapphirine–mesoperthitic K-feldspar–

rutile–melt. This assemblage does not appear in the T-M_O pseudosection (Fig. 13). The

field corresponding to the peak assemblage is chosen to be one that also includes

orthopyroxene (see text for T–M_O diagram, Fig. 13). The reason the field corresponding

to what is observed in the thin section does not occur is a consequence of the

composition of orthopyroxene versus sillimanite in the context of typical sapphirine–

quartz rock compositions (see figure in Appendix G). Therefore, in sample R31180, the

peak field of quartz–sapphirine–mesoperthitic K-feldspar–rutile–melt–orthopyroxene

occurs at temperatures >1050°C (Fig. 13). Constraining tighter peak conditions in this

field are difficult but existing estimates of peak temperatures in the Napier Complex

UHT rocks are ~1050 to >1120 °C (Sandiford & Powell, 1986; Harley, 1987; Hensen

and Motoyoshi, 1992; Harley and Motoyoshi, 2000; Hollis & Harley, 2002; Hokada et

al., 2008; Harley, 1998; Harley, 2008; Shimuzu et al., 2013;). Regardless of the specific

peak temperature, the peak metamorphic conditions are well within the UHT realm. The

Napier Complex is well-known as a near-isobarically cooled terrane (Sheraton et al.,

1980; Harley, 1989; Sandiford, 1985a), and so I have interpreted the post-peak P–T path

to pass into the stability field of orthopyroxene–sillimanite–bearing assemblages, as per

the petrographic interpretations (Fig. 13).

ZIR concentrations and thermometry

The *P–T* and geochronology (Appendix D) framework provides a sound basis for interpreting the main focus of this study, ZIR concentration and thermometry results in the context of the microstructural setting of rutile and its proximity to zircon.

A ZIR concentration of ~4000 ppm produces a ZIR temperature of ~900 °C, and thus represents the minimum amount of ZIR required to show UHT conditions. Interestingly, the data in Table 3, and in Figs. 18b,f,j–21b,f,j, show that the vast majority of rutile grains in all four samples preserve ZIR concentrations < ~4000–6000 ppm, after reintegration of exsolved Zr back into rutile. Sample AK-6 has the largest proportion of ZIR ppm >4000 ppm (Fig. 20b,f,j), whereas sample R31180 records the smallest proportion of ZIR ppm >4000 ppm (Fig. 21b,f,j). The majority of ZIR ppm data for R31180 are <1000 ppm, even after reintegration of exsolved Zr (Fig. 21b,j). Several options may explain the preponderance of low ZIR ppm in R31180. First is that the majority of the analysed rutile grew at either an earlier or later stage than the peak of metamorphism, thus never witnessing the peak UHT conditions. Second, the ratio of rutile:zircon in the sample could indicate there was a deficiency of Zr (in zircon) to allow ZIR concentrations to become high. Third, there may be out-of-plane influences on ZIR concentrations by xenocrystic zircon not seen in the 2D plane of a thin section. Fourth may be the long-lived residence time of the Napier Complex in the deep crust.

For the first option, it is highly likely that rutile grew during the prograde evolution and was stable at the metamorphic peak. Rutile forms during prograde metamorphism by the breakdown of Ti reservoirs such as biotite (White et al., 2014a,b). At the peak UHT conditions, well above biotite stability (White et al., 2014a,b), rutile is the only Ti-bearing mineral in the rock. If at least some rutile is preserving low Zr concentrations

from earlier in the prograde history, I might expect these grains to occur as inclusions in other minerals. Indeed, Figs. 21f,h show that all rutile inclusions in this rock preserve lower Zr concentrations. This could mean that at least some rutile was shielded from obtaining more Zr as temperature increased. For grain boundary-hosted rutile, the lower Zr concentrations (Fig. 21j, l) are more problematic as retrograde rutile growth is difficult to explain for this sample.

The relative abundance of rutile to zircon (12.75:1.0 in Table 1), indicates that rutile is far more abundant than zircon in this sample (see also Fig. 16). Although this is not the highest rutile:zircon ratio of all investigated samples, it does suggest that a lack of Zr reservoirs could have prevented a majority of rutile grains from preserving UHT conditions. However, the data in Figs. 21d,l contrast with this notion as low (reintegrated) ZIR concentrations occur in rutile that is very proximal (<100 μm) to zircon (Fig. 21l). Out-of-plane zircon grains not imaged by BSE and MLA mapping are unlikely to explain the low ZIR ppm concentrations, because proximity to xenocrystic zircon does not appear to have influenced ZIR ppm concentrations.

The last option, the long residence time of ca. 1000–1500 Myr of the Napier Complex granulites in the deep crust (Sandiford, 1985a, b; Carson et al., 2002a, b; Black et al., 1983) has merit as it allows for ample high-temperature diffusion to occur. Indeed, many of the ZIR temperatures for R31180 are in the range 600–800 °C after Zr reintegration (Fig. 21). Grains that preserve very low ZIR temperatures are predominantly located at grain boundaries (Fig. 25l). Resetting of ZIR to temperatures ~500–300 °C lower than the metamorphic peak strongly suggests the equilibrium relation between quartz, rutile and zircon was sustained for many of the rutile grains in

the rock. This would imply that diffusion of Si out of rutile—which is argued to be slow and a determining factor for Zr retention in rutile (e.g. Taylor-Jones and Powell, 2015)—was sustained over that full cooling range. However, to complicate things, other rutile grains in R31180 located along grain boundaries preserve ZIR concentrations indicative of UHT conditions after reintegration (Figs. 25l). The simplest interpretation is that these grains became isolated from zircon during cooling (Taylor-Jones & Powell, 2015), however calculations of distance to xenocrystic zircon (Fig. 25l) show that these grains are not more distal from zircon than those that did not preserve UHT conditions. Therefore, it remains unclear why some grains have reset their ZIR chemistry and others have not.

The distribution of reintegrated ZIR temperatures in sample AK-3, specifically that the majority of them are <900 °C with $a\mathrm{SiO_2} = 1.0$ (Figs. 21j,l), can be partly attributed to the absence of quartz, which implies $a\mathrm{SiO_2} < 1.0$ and a reduced ability of rutile to intake Zr (with Si; Taylor-Jones & Powell, 2015) during heating. AK-3 has 51.60 wt% $\mathrm{SiO_2}$, which translates to $a\mathrm{SiO_2} \sim 0.5$ (see Ferry & Watson, 2007). Therefore, reintegrated ZIR temperatures shown in Fig. 26e, clustering around 600–700 °C, are more appropriate. However, consideration still needs to be given to when rutile may have grown. If rutile is predominantly relict (i.e. was formerly inclusions in now-resorbed peak minerals) then rutile is prograde and peak and preserves a mix of temperatures towards, and at, the peak of metamorphism. This could be argued to explain the distribution of ZIR temperatures for $a\mathrm{SiO_2} = 0.5$, which reach a maximum of ~900 °C (Fig. 26e). If rutile is predominantly retrograde it may be expected to show a range of temperatures, analogous to relict rutile, decreasing from the peak of metamorphism (but adjusted down due to lower $a\mathrm{SiO_2}$) to some temperature along the retrograde path. The

growth of rutile during retrograde metamorphism would require a Ti source, such as silicate melt and/or garnet (Ague & Eckert, 2012; Ague et al., 2013; Kawasaki & Motoyoshi, 2007) and/or orthopyroxene (Kawasaki & Motoyoshi, 2007). I tentatively interpret that the ZIR temperatures in AK-3 are a combination of the possibilities, i.e. relict (and peak) and retrograde rutile, in the absence of being able to make a definitive distinction between generations of growth.

ZIR temperatures, with Zr reintegration, in sample AK-5 span a wide range, from ~730 to ~1210 °C (Fig. 20b,d,j,l). Rutile grain size shows a strong correlation with its location in the rock. Coarser grains typically occur within or in direct contact with coarse-grained orthopyroxene (which is a combination of opx_1 and opx_2) and finer-grained rutile occurs concentrated in symplectic parts of the rock (Fig. 15). This suggests that the finer-grained rutile may be of different (retrograde) origin to the coarser-grains. Fine-grained rutile does not preserve systematically different ZIR temperatures than coarse-grained examples. Fine-grained rutile may originate from decomposition of garnet during retrograde metamorphism, analogous to that proposed for AK-3 (Ague et al., 2013; Kawasaki & Motoyoshi, 2007), while coarse-grained rutile could be peak or prograde. Despite the lack of correlation between rutile size and ZIR concentrations, this does not preclude the possibility that different generations of rutile growth may preserve differing ZIR concentrations. Sample AK-5 has the highest rutile:zircon ratio (Table 1), suggesting that of all samples, this one has potential for chemical communication via element exchange between zircon and rutile to be inhibited. However, a significant proportion of analyses record UHT conditions after Zr reintegration (compare Fig. 23c to 23d), indicating the $ZIR + SiO_2$ = zircon equilibrium was sustained up to and beyond the metamorphic peak, providing clear evidence there is

no apparent limit to the length scale over which xenocrystic zircon may chemically interact with rutile (Figs. 23c,d,g,h,k,l). Last, the ZIR concentrations and (Zr-reintegrated) temperatures recorded by rutile in this sample match very well with the ZIR concentrations and temperatures shown in the calculated P–T pseudosection, Figs. 9, 10. Therefore, the calculated P–T pseudosection may be used to argue that at least some rutile in this sample grew during the retrograde history of the rock.

Sample AK-6 is the only one to record a number of ZIR temperatures from rutile grains without reintegration of exsolved Zr back into rutile (Figs. 25a,e,i,c,g,k). What this implies is that Si (and Zr) communication was broken between rutile, quartz and zircon during cooling. This seems odd as AK-6 is more quartz-rich than AK-5; however, AK-6 is more felsic and drier than AK-5, which may indicate that Zr exsolution from rutile was less commonly inhibited by a lack of Si. The majority of the ZIR temperatures for AK-6 cluster in the interval ~890–960 °C (Figs. 25, 26) which could reflect either that: Si diffusion out of zircon stopped in this range (Taylor-Jones & Powell, 2015); or rutile grew along the retrograde P–T path as a result of decomposition of other Ti-reservoirs such as garnet and/or orthopyroxene (Ague et al., 2013; Kawasaki & Motoyoshi, 2007), as argued above for other samples. This temperature interval corresponds reasonably well with the interpreted near-isobaric cooling part of the retrograde P–T path (Fig. 11), where the P–T path involves crossing rutile abundance contours at a high angle (Fig. 12f), i.e. more rapid, abundant rutile growth than compared to the steeply decompressional segment of the P–T path. Therefore, I interpret that the rutile in AK-6 is probably a combination of prograde, peak and retrograde grains, reflected well in the ZIR concentration and thermometry data.

Microstructural location and proximity to xenocrystic zircon

ZIR concentration data (Figs. 18-21) show that for the total dataset for each sample there is no obvious correlation with the distance to xenocrystic zircon grains (Figs. 18–21c,d), regardless of whether exsolved Zr is reintegrated back into rutile. In addition, though ZIR ppm data are dominated by rutile grains located at grain boundaries, there is no clear correlation between the microstructural setting of rutile and its ZIR concentration in relation to the nearest xenocrystic zircon grain (compare Figs. 18–21g,h,k,l), despite mean ZIR ppm statistics typically showing higher ZIR ppm in rutile grains located along grain boundaries (Table 3). Moreover, no noticeable correlation was determined between the magnitude of the increase in Zr concentration post-reintegration and distance to xenocrystic zircon. That is, the amount of Zr exsolved was apparently not consistent among rutile grains throughout a sample (Appendix C).

A number of existing studies have documented a strong correlation between rutile Zr composition and proximity to *exsolved* zircon (Luvizotto & Zack, 2009; Jiao et al., 2011; Kooijman et al., 2012; Ewing et al., 2013). I have also found this in my study. However, I have progressed understanding to show that the ZIR + SiO_2 = zircon equilibrium operates effectively over length scales much greater than the typical size of individual rutile and zircon grains. This means that prograde rutile grains could very likely attain Zr concentrations corresponding to the thermal peak of UHT metamorphism. However, my data also strongly suggests that during the retrograde evolution this equilibrium remains operational causing many grains to no longer record UHT conditions, even after exsolved Zr is reintegrated. Therefore, in the three quartz-bearing samples, stunted Si diffusion does not appear to have been a dominant factor in determining ZIR concentrations and temperatures (contrast with Taylor-Jones &

Powell, 2015), as there are no known examples of rutile grains preserving peak (i.e.

>1000 °C) temperatures that have *not* exsolved zircon. The major consequence is that

ZIR thermometry may almost never preserve the *peak* UHT conditions in regional

terranes where cooling is prolonged. In terranes where sustained cooling has occurred

(Napier Complex), the ZIR + SiO_2 = zircon equilibrium operates to remove the record

of UHT metamorphism from almost all rutile grains.

The dominant ZIR temperatures without any Zr reintegration are in the range of ~650–

800 °C (Figs. 22–25 a,c) which correlates well with the lower-temperature peak of ~780

°C in the bimodal distribution of ZIR temperatures in the global dataset (Kelsey &

Hand, 2015). The bimodal distribution has been explained as being due to exsolution

combined with Zr diffusion closure (e.g. Taylor-Jones & Powell, 2015; Pape et al.,

2016). However, bimodality occurs even *after* Zr reintegration (Figs. 22-25), possibly

reflecting a microstructural control on access to Si and Zr reservoirs that remained

buried in my dataset, perhaps combined with the timing of growth of different rutile

grains.

CONCLUSIONS

The main aims of the study were to investigate whether the microstructural location

(inclusion vs grain boundary) of rutile plays a role in controlling its ZIR temperature by

means of facilitating or restricting its access to Zr; as well as to investigate whether the

distance from xenocrystic zircon plays a role in controlling ZIR concentrations and

temperatures.

Four samples were investigated, and all were shown to be UHT samples with peak *P–T*

conditions of >1000 °C, but mostly preserve less-than-UHT ZIR temperatures. No

correlation was found between microstructural location and ZIR temperatures, nor distance to xenocrystic zircon. However, a more comprehensive dataset may yet prove that rutile grown at different stages of the rocks history have a correlation to ZIR temperatures. This suggests that the ZIR + SiO_2 = zircon equilibrium operates effectively over length scales much greater than the typical size of individual rutile and zircon grains for the prograde as well as part of the retrograde history. The major consequence is that ZIR thermometry may almost never preserve the peak UHT conditions, especially for very slowly-cooled terranes such as the Napier Complex.

ACKNOWLEDGMENTS

REFERENCES

AGUE, J. J., & ECKERT, J. O. (2012). Precipitation of rutile and ilmenite needles in garnet: Implications for extreme metamorphic conditions in the Acadian Orogen, U.S.A. *American Mineralogist, 97*(5-6), 840-855. doi:10.2138/am.2012.4015

AGUE, J. J., ECKERT, J. O., CHU, X., BAXTER, E. F., & CHAMBERLAIN, C. P. (2013). Discovery of ultrahigh-temperature metamorphism in the Acadian orogen, Connecticut, USA. *Geology, 41*(2), 271-274. doi:10.1130/g33752.1

BALDWIN, J. A., & BROWN, M. (2008). Age and duration of ultrahigh-temperature metamorphism in the Anápolis–Itauçu Complex, Southern Brasília Belt, central Brazil – constraints from U–Pb geochronology, mineral rare earth element chemistry and trace-element thermometry. *Journal of Metamorphic Geology, 26*(2), 213-233. doi:10.1111/j.1525-1314.2007.00759.x

BLACK, L. P., JAMES, P. R., & HARLEY, S. L. (1983). Geochronology and geological evolution of metamorphic rocks in the Field Islands area, East Antarctica. *Journal of Metamorphic Geology, 1*, 277-303.

BLACKBURN, T., SHIMIZU, N., BOWRING, S. A., SCHOENE, B., & MAHAN, K. H. (2012). Zirconium in rutile speedometry: New constraints on lower crustal cooling rates and residence temperatures. *Earth and Planetary Science Letters, 317–318*, 231-240. doi:http://dx.doi.org/10.1016/j.epsl.2011.11.012

BOSE, FUKUOKA, SENGUPTA, & DASGUPTA. (2000). Evolution of high-Mg–Al granulites from Sunkarametta, Eastern Ghats, India: evidence for a lower crustal heating–cooling trajectory. *Journal of Metamorphic Geology, 18*(3), 223-240. doi:10.1046/j.1525-1314.2000.00253.x

BOSE, S., & DAS, K. (2007). Sapphirine + quartz assemblage in contrasting textural modes from the Eastern Ghats Belt, India: Implications for stability relations in UHT metamorphism and retrograde processes. *Gondwana Research, 11*(4), 492-503. doi:http://dx.doi.org/10.1016/j.gr.2006.07.003

BROWN, M. (2007). Metamorphic Conditions in Orogenic Belts: A Record of Secular Change. *International Geology Review, 49*(3), 193-234. doi:10.2747/0020-6814.49.3.193

BROWN, M. (2014). The contribution of metamorphic petrology to understanding lithosphere evolution and geodynamics. *Geoscience Frontiers, 5*(4), 553-569. doi:http://dx.doi.org/10.1016/j.gsf.2014.02.005

CARSON, C. J., AGUE, J. J., & COATH, C. D. (2002b). U-Pb geochronology from Tonagh island, East Antarctica: implications for the timing of ultra-high temperature metamorphism of the Napier Complex. *Precambrian Research, 116*, 237-263.

CARSON, C. J., AGUE, J. J., GROVE, M., COATH, C. D., & HARRISON, T. M. (2002a). U-Pb isotopic behaviour of zircon during upper-amphibolite facies fluid

infiltration in the Napier Coplex, east Antarctica. *Earth and Planetary Science Letters, 199*, 287-310.

CHERNIAK, D. J., MANCHESTER, J., & WATSON, E. B. (2007). Zr and Hf diffusion in rutile. *Earth and Planetary Science Letters, 261*(1–2), 267-279. doi:http://dx.doi.org/10.1016/j.epsl.2007.06.027

CHERNIAK, D. J., WATSON, E. B., GROVE, M., & HARRISON, T. M. (2004). Pb diffusion in monazite: a combined RBS/SIMS study. *Geochimica et Cosmochimica Acta, 68*, 829-840.

DASGUPTA S., SANYAL, S., SENGUPTA, P., & FUKUOKA, M. (1994). Petrology of Granulites from Anakapalle—Evidence for Proterozoic Decompression in the Eastern Ghats, India. *Journal of Petrology, 35*(2), 433-459. doi:10.1093/petrology/35.2.433

DASGUPTA S., SENGUPTA, P., EHL, J., RAITH, M., & BARDHAN, S. (1995). Reaction Textures in a Suite of Spinel Granulites from the Eastern Ghats Belt, India: Evidence for Polymetamorphism, a Partial Petrogenetic Grid in the System KFMASH and the Roles of ZnO and Fe2O3. *Journal of Petrology, 36*(2), 435-461. doi:10.1093/petrology/36.2.435

ELLIS, D. J., SHERATON, J. W., ENGLAND, R. N., & DALLWITZ, W. B. (1980.). Osumilite-sapphirine-quartz granulites from Enderby Land, Antarctica: mineral assemblages and reactions. *Contributions to Mineralogy and Petrology, 72*, 123–143.

EWING, T., HERMANN, J., & RUBATTO, D. (2013). The robustness of the Zr-in-rutile and Ti-in-zircon thermometers during high-temperature metamorphism (Ivrea-Verbano Zone, northern Italy). *Contributions to Mineralogy and Petrology, 165*(4), 757-779. doi:10.1007/s00410-012-0834-5

FERRY, J., & WATSON, E. (2007). New thermodynamic models and revised calibrations for the Ti-in-zircon and Zr-in-rutile thermometers. *Contributions to Mineralogy and Petrology, 154*(4), 429-437. doi:10.1007/s00410-007-0201-0

FITZSIMONS, I. C. W., & HARLEY, S. L. (1994). The Influence of Retrograde Cation Exchange on Granulite P-T Estimates and a Convergence Technique for the Recovery of Peak Metamorphic Conditions. *Journal of Petrology, 35*(2), 543-576. doi:10.1093/petrology/35.2.543

GREW, E. S. (1980). Sapphirine + quartz association from Archaen rocks in Enderby Land, Antarctica. *American Mineralogist, 65*, 821-836.

HALPIN, J. A., DACZKO, N. R., MILAN, L. A., & CLARKE, G. L. (2012). Decoding near-concordant U–Pb zircon ages spanning several hundred million years: recrystallisation, metamictisation or diffusion? *Contributions to Mineralogy and Petrology, 163*(1), 67-85. doi:10.1007/s00410-011-0659-7

HARLEY, S. L. (1987). A pyroxene-bearing meta-ironstone and other pyroxene-granulites from Tonagh Island, Enderby Land, Antarctica: further evidence for very high temperature (980 °C) Archaean regional metamorphism in the Napier Complex. *Journal of Metamorphic Geology, 5*, 341-356. doi:http://dx.doi.org/10.1111/j.1525-1314.1987.tb00389.x

HARLEY, S. L. (1989). The origins of granulites: a metamorphic perspective. *Geological Magazine, 126*, 215-247.

HARLEY, S. L. (1998). On the occurrence and characterization of ultrahigh-temperature crustal metamorphism. *Geological Society Special Publication, 138*, 81-107. doi:10.1144/GSL.SP.1996.138.01.06

HARLEY, S. L. (2008). Refining the P–T records of UHT crustal metamorphism. *Journal of Metamorphic Geology, 26*(2), 125-154. doi:10.1111/j.1525-1314.2008.00765.x

HARLEY, S. L., & MOTOYOSHI, Y. (2000). Al zoning in orthopyroxene in a
sapphirine quartzite: evidence for >1,120 C UHT metamorphism
in the Napier Complex, Antarctica, and implications for
the entropy of sapphirine. *Contributions to Mineralogy and Petrology, 138*, 293–307.

HENSEN, B. J. (1971). Theoretical phase relations involving cordierite and garnet in the system MgO FeO Al2O3 SiO2. *Contributions to Mineralogy and Petrology, 33*, 191-214.

HENSEN, B. J. (1987). P T grids for silica-undersaturated granulites in the systems MAS (n + 4) and FMAS (n + 3)-tools for the derivation of P T paths of metamorphism. *Geology, 5*(2), 255-271.

HENSEN, B. J., & MOTOYOSHI, Y. (1992). *Osumilite-producing reactions in high-temperature granulites from the Napier Complex, East Antarctica: tectonic implications* (Y. Yoshida, K. Kaminuma, & K. Shiraishi Eds.): Recent progress in Antarctic Earth Science: Tokyo, Terra Scientifica Publishing Company

HOKADA, T., MOTOYOSHI, Y., SUZUKI, S., ISHIKAWA, M., & ISHIZUKA, H. (2008). Geodynamic evolution of Mt. Riiser-Larsen, Napier Complex, East Antarctica, with reference to the UHT mineral associations and their reaction relations. *Geological Society, London, Special Publications, 308*(1), 253-282. doi:10.1144/sp308.13

HOLLAND, T. J. B., & POWELL, R. (2011). An improved and extended internally consistent thermodynamic dataset for phases of petrological interest, involving a new equation of state for solids *J. Metamorph. Geol.* (Vol. 29, pp. 333-383).

HOLLIS, J., & HARLEY, S. L. (2002). New evidence for the peak temperatures and the near-peak pressure temperature evolution o the Napier Complex. *Royal Society of New Zealand Bulletin, 35*, 19-29.

JIAO, S., GUO, J., MAO, Q., & ZHAO, R. (2011). Application of Zr-in-rutile thermometry: a case study from ultrahigh-temperature granulites of the Khondalite belt, North China Craton. *Contributions to Mineralogy and Petrology, 162*(2), 379-393. doi:10.1007/s00410-010-0602-3

KAWASAKI, T., & MOTOYOSHI, Y. (2007). Solubility of TiO2 in Garnet and Orthopyroxene: Ti Thermometer for Ultrahigh-temperature Granulites. *U.S. Geological Survey and the National Academies;, USGS OF-2007-1047. Short Research Paper 038*.

KELLY, N., & HARLEY, S. (2005). An integrated microtextural and chemical approach to zircon geochronology: refining the Archaean history of the Napier Complex, east Antarctica. *Contributions to Mineralogy and Petrology, 149*(1), 57-84. doi:10.1007/s00410-004-0635-6

KELSEY, D. E. (2008). On ultrahigh-temperature crustal metamorphism. *Gondwana Research, 13*(1), 1-29. doi:10.1016/j.gr.2007.06.001

KELSEY, D. E., CLARK, C., & HAND, M. (2008). Thermobarometric modeling of zircon and monazite growth in melt-bearing systems: examples using model metapelitic and metapsammitic granulites. *Journal of Metamorphic Geology, 26*, 199-212.

KELSEY, D. E., & HAND, M. (2015). On ultrahigh temperature crustal metamorphism: Phase equilibria, trace element thermometry, bulk composition, heat sources, timescales and tectonic settings. *Geoscience Frontiers, 6*(3), 311-356. doi:10.1016/j.gsf.2014.09.006

KELSEY, D. E., & POWELL, R. (2011). Progress in linking accessory mineral growth and breakdown to major mineral evolution in metamorphic rocks: a thermodynamic approach in the Na2O-CaO-K2O-FeO-MgO-Al2O3-SiO2-H2O-TiO2-ZrO2 system. *Journal of Metamorphic Geology, 29*, 151.

KELSEY, D. E., WHITE, R. W., HOLLAND, T. J. B., & POWELL, R. (2004). Calculated phase equilibria in K2O-FeO-MgO-Al2O3-SiO2-H2O for sapphirine-quartz-bearing mineral assemblages. *Journal of Metamorphic Geology, 22*, 559-578.

KELSEY, D. E., WHITE, R. W., & POWELL, R. (2005). Calculated phase equilibria in K2O-FeO-MgO-Al2O3-SiO2-H2O for silica-undersaturated sapphirine-bearing mineral assemblages. *Journal of Metamorphic Geology, 23*(4), 217-239. doi:10.1111/j.1525-1314.2005.00573.x

KOOIJMAN, E., SMIT, M. A., MEZGER, K., & BERNDT, J. (2012). Trace element systematics in granulite facies rutile: implications for Zr geothermometry and provenance studies. *Journal of Metamorphic Geology, 30*(4), 397-412. doi:10.1111/j.1525-1314.2012.00972.x

KORHONEN, F. J., BROWN, M., CLARK, C., & BHATTACHARYA, S. (2013). Osumilite–melt interactions in ultrahigh temperature granulites: phase equilibria modelling and implications for the P–T–t evolution of the Eastern Ghats Province, India. *Journal of Metamorphic Geology, 31*(8), 881-907. doi:10.1111/jmg.12049

KORHONEN, F. J., CLARK, C., BROWN, M., BHATTACHARYA, S., & TAYLOR, R. (2013). How long-lived is ultrahigh temperature (UHT) metamorphism? Constraints from zircon and monazite geochronology in the Eastern Ghats orogenic belt, India. *Precambrian Research, 234*, 322-350. doi:10.1016/j.precamres.2012.12.001

KORHONEN, F. J., CLARK, C., BROWN, M., & TAYLOR, R. J. M. (2014). Taking the temperature of Earth's hottest crust. *Earth and Planetary Science Letters, 408*, 341-354. doi:http://dx.doi.org/10.1016/j.epsl.2014.10.028

KORHONEN, F. J., SAW, A. K., CLARK, C., BROWN, M., & BHATTACHARYA, S. (2011). New constraints on UHT metamorphism in the Eastern Ghats Province through the application of phase equilibria modelling and in situ geochronology. *Gondwana Research, 20*(4), 764-781. doi:10.1016/j.gr.2011.05.006

KOTKOVÁ, J., & HARLEY, S. L. (2010). Anatexis during High-pressure Crustal Metamorphism: Evidence from Garnet–Whole-rock REE Relationships and Zircon–Rutile Ti–Zr Thermometry in Leucogranulites from the Bohemian Massif. *Journal of Petrology, 51*(10), 1967-2001. doi:10.1093/petrology/egq045

LUVIZOTTO, G. L., & ZACK, T. (2009). Nb and Zr behavior in rutile during high-grade metamorphism and retrogression: An example from the Ivrea–Verbano

Zone. *Chemical Geology, 261*(3–4), 303-317.
doi:http://dx.doi.org/10.1016/j.chemgeo.2008.07.023

MARSHALL, S. (2010). An integrated metamorphic, geochronological and spatial approach to the classic Eastern Ghats large hot orogen, India. *Unpublished Honours thesis, University of Adelaide.*

MEYER, M., JOHN, T., BRANDT, S., & KLEMD, R. (2011). Trace element composition of rutile and the application of Zr-in-rutile thermometry to UHT metamorphism (Epupa Complex, NW Namibia). *Lithos, 126*(3–4), 388-401. doi:http://dx.doi.org/10.1016/j.lithos.2011.07.013

MORRISSEY, L. J., HAND, M., KELSEY, D. E., & WADE, B. P. (2016). Cambrian high-temperature reworking of the Rayner-Eastern Ghats Terrane constraints from the northern Prince Charles Mountains region, East Antarctica. *Journal of Petrology, 57*(1), 53-92. doi:10.1093/petrology/egv082

MOURI, H., GUIRAUD, M., & OSANAI, Y. (2004). Review on "conundum plus quartz" assemblage in nature: possible indicatior of ultra-high temperature conditions? . *Journal of Mineralogical and Petrological Sciences, 99*, 159-163.

PAPE, J., MEZGER, K., & ROBYR, M. (2016). A systematic evaluation of the Zr-in-rutile thermometer in ultra-high temperature (UHT) rocks. *Contributions to Mineralogy and Petrology, 171*(5), 44. doi:10.1007/s00410-016-1254-8

PATTISON, D. R. M., & BÉGIN, N. J. (1994). Zoning patterns in orthopyroxene and garnet in granulites: implications for geothermometry. *Journal of Metamorphic Geology, 12*(4), 387-410. doi:10.1111/j.1525-1314.1994.tb00031.x

PATTISON, D. R. M., CHACKO, T., FARQUHAR, J., & MCFARLANE, C. R. M. (2003). Temperatures of Granulite-facies Metamorphism: Constraints from Experimental Phase Equilibria and Thermobarometry Corrected for Retrograde Exchange. *Journal of Petrology, 44*(5), 867-900. doi:10.1093/petrology/44.5.867

PEARCE, M. A., WHITE, A. J. R., & GAZLEY, M. F. (2015). TCInvestigator: automated calculation of mineral mode and composition contours for thermocalc pseudosections. *Journal of Metamorphic Geology, 33*(4), 413-425. doi:10.1111/jmg.12126

POWELL, R., & HOLLAND, T. J. B. (1988). An internally consistent dataset with uncertainties and correlations: 3. Applications to geobarometry, worked examples and a computer program. *Journal of Metamorphic Geology, 6*(2), 173-204. doi:10.1111/j.1525-1314.1988.tb00415.x

RACEK, M., ŠTIPSKA, P., & POWELL, R. (2008). Garnet–clinopyroxene intermediate granulites in the St. Leonhard massif of the Bohemian Massif: ultrahigh-temperature metamorphism at high pressure or not? *Journal of Metamorphic Geology, 26*(2), 253-271. doi:10.1111/j.1525-1314.2007.00754.x

RAPP, R. P., RYERSON, F. J., & MILLER, C. F. (1987). Experimental evidence bearing on the stability of monazite during crustal anatexis. *Geophysical Research Letters, 14*, 307-310.

RICKERS, K., RAITH, M., & DASGUPTA, S. (2001). Multistage reaction textures in xenolithic high-MgAl granulites at Anakapalle, Eastern Ghats Belt, India:

examples of contact polymetamorphism and infiltration-driven metasomatism. *Journal of Metamorphic Geology, 19*(563-582).

SAJEEV, K., WILLIAMS, I. S., & OSANAI, Y. (2010). Sensitive high-resolution ion microprobe U-Pb dating of prograde and retrograde ultrahigh-temperature metamorphism as exemplified by Sri Lankan granulites. *Geology, 38*, 971-974.

SANDIFORD, M. (1985a). The metamorphic evolution of granulites at Fyfe Hills implications for Archaean crustal thickness in Enderby Land, Antarctica. *Journal of Metamorphic Geology, 3*(2), 155-178. doi:10.1111/j.1525-1314.1985.tb00312.x

SANDIFORD, M. A. (1984). Structural and metamorphic studies in the Fyfe Hills - Khmara Bay region, Enderby Land, Antarctica. *PhD thesis*.

SANDIFORD, M. A. (1985b). The Origin of retrograde shear zones in the Napier Complex: implication for the tectonic evolution of Enderby Land, Antarctica. *Journal of Structural Geology, 7*, 477-488.

SANDIFORD, M. A., & POWELL, R. (1986). Pyroxene exsolution in granulites from Fyfe Hills, Enderby Land, Antarctica: evidence for 1000 C metamorphic temperatures in Archean continental crust. *American Mineralogist, 71*, 946-954.

SARKAR, S., DASGUPTA, S., & FUKUOKA, M. (2003). Petrological evolution of a suite of spinel granulites from Vizianagram, Eastern Ghats Belt, India, and genesis of sapphirine-bearing assemblages. *Journal of Metamorphic Geology, 21*(9), 899-913. doi:10.1046/j.1525-1314.2003.00490.x

SCHMITZ, M. D., & BOWRING, S. A. (2003). Ultrahigh-temperature metamorphism in the lower crust during Neoarchean Ventersdorp rifting and magmatism, Kaapvaal craton, southern Africa. *Geological Society of America Bulletin, 115*, 533-548.

SENGUPTA, P., DASGUPTA, S., BHATTACHARYA, P. K., FUKUOKA, M., CHAKRABORTI, S., & BHOWMICK, S. (1990). Petro-tectonic Imprints in the Sapphirine Granulites from Anantagiri, Eastern Ghats Mobile Belt, India. *Journal of Petrology, 31*(5), 971-996. doi:10.1093/petrology/31.5.971

SHERATON, J. W., OFFE, L. A., J., T. R., & ELLIS, D. J. (1980). Enderby Land, Antarctica - an unusual Precambrian high-grade metamorphic terrain. *Geological Society of Australia Journal, 27*, 1-18.

SHIMIZU, H., TSUNOGAE, T., & SANTOSH, M. (2013). Petrology and phase equilibrium modeling of sapphirine + quartz assemblage from the Napier Complex, East Antarctica: diagnostic evidence for Neoarchean ultrahigh-temperature metamorphism. *Geoscience Frontiers, 4*, 655-666.

SIMMAT, R., & RAITH, M. M. (2008). U–Th–Pb monazite geochronometry of the Eastern Ghats Belt, India: Timing and spatial disposition of poly-metamorphism. *Precambrian Research, 162*(1), 16-39. doi:10.1016/j.precamres.2007.07.016

SKRZYPEK, E., STIPSKA, P., & COCHERIE, A. (2012). The origin of zircon and the significance of U-Pb ages in high-grade metamorphic rocks: a case study from the Variscan orogenic root (Visges Mountains, NE France). *Contributions to Mineralogy and Petrology, 164*.

Stepanov, A. S., Hermann, J., Rubatto, D., & Rapp, R. P. (2012). Experimental study of monazite/melt partitioning with implications for the Ree, Th and U geochemistry of crustal rocks. *Chemical Geology, 300-301*, 200-220.

Taylor-Jones, K., & Powell, R. (2015). Interpreting zirconium-in-rutile thermometric results. *Journal of Metamorphic Geology, 33*(2), 115-122. doi:10.1111/jmg.12109

Taylor, R., Clark, C., Johnson, T., Santosh, M., & Collins, A. (2015). Unravelling the complexities in high-grade rocks using multiple techniques: the Achankovil Zone of southern India. *Contributions to Mineralogy and Petrology, 169*(5), 1-19. doi:10.1007/s00410-015-1147-2

Tomkins, H. S., Powell, R., & Ellis, D. J. (2007). The pressure dependence of the zirconium-in-rutile thermometer. *Journal of Metamorphic Geology, 25*(6), 703-713. doi:10.1111/j.1525-1314.2007.00724.x

Walsh, A. K., Kelsey, D. E., Kirkland C. L., Hand, M., Hugh Smithies, R., & Clark, C. (2016). P–T–t evolution of a large, long-lived, ultrahigh-temperature Grenvillian belt in central Australia. *Gondwana Research*.

Wark, D. A., & Watson, E. B. (2006). TitaniQ: a titanium-in-quartz geothermometer. *Contributions to Mineralogy and Petrology, 152*(6), 743-754. doi:10.1007/s00410-006-0132-1

Watson, E. B., & Harrison, T. M. (2005). Zircon Thermometer Reveals Minimum Melting Conditions on Earliest Earth. *Science, 308*(5723), 841-844. doi:10.1126/science.1110873

Watson, E. B., Wark, D. A., & Thomas, J. B. (2006). Crystallization thermometers for zircon and rutile. *Contributions to Mineralogy and Petrology, 151*(4), 413-433. doi:10.1007/s00410-006-0068-5

White, R. W., & Powell, R. (2002). Melt loss and the preservation of granulite facies mineral assemblages. *Journal of Metamorphic Geology, 20*(7), 621-632. doi:10.1046/j.1525-1314.2002.00206_20_7.x

White, R. W., & Powell, R. (2011). On the interpretations of retrograde reaction textures in granulity facies rocks. *Journal of Metamorphic Geology, 29*, 131-149.

White, R. W., Powell, R., Holland, T. J. B., & Green, E. C. R. (2014a). Progress relating to calculation of partial melting equilibria for metapelites. *Journal of Metamorphic Geology, 25*(5), 511-527. doi:10.1111/j.1525-1314.2007.00711.x

White, R. W., Powell, R., Holland, T. J. B., Johnson, T. E., & Green, E. C. R. (2014b). New mineral activity-composition relations for thermodynamic calculations in metapelitic systems. *Journal of Metamorphic Geology, 32*(3), 261-286. doi:10.1111/jmg.12071

Yukymchuk, C., & Brown, M. (2014). behaviour of zircon and monazite during crustal melting. *Journal of the Geological Society, London, 171*, 465-479.

Zack, T., Moraes, R., & Kronz, A. (2004). Temperature dependence of Zr in rutile empirical calibration of a rutile thermometer. *Contributions to Mineralogy and Petrology, 148*(4), 471-488. doi:10.1007/s00410-004-0617-8

Appendix A: Petrography

AK-3

In thin section the coarse-grained assemblage in the sample comprises very coarse garnet (~500 μm to >2–3 cm), brown orthopyroxene (0.5–1 cm), spinel (up to 7 mm), biotite (4–6 mm), K-feldspar and plagioclase. Garnet contains inclusions of sapphirine and euhedral rutile grains. Rare biotite and rutile are dispersed throughout the sample. All coarse-grained Fe–Mg minerals are isolated by extensively-developed fine-grained symplectites and coronas. Garnet and orthopyroxene are mantled by symplectic intergrowths of sapphirine$_2$ and orthopyroxene$_2$ (Fig. 3a). The sapphirine$_2$ orthopyroxene$_2$ symplectites occur in contact with local patches of biotite$_3$, sillimanite$_3$ and plagioclase$_3$ (Fig. 3c). Plagioclase$_3$ also occurs as an ~50 μm moat between garnet and sapphirine$_2$-orthopyroxene$_2$ symplectites (Fig. 3a). Small garnet grains with inclusions of sapphirine and orthopyroxene ribs (symplectites) are interpreted to postdate the symplectite (Fig. 3d). Spinel is rare and is mantled by a corona of sapphirine$_2$ and possibly plagioclase$_2$ (Fig. 3b). Rare coarse-grained perthite/mesoperthite-bearing (i.e. K-feldspar and plagioclase) veins, interpreted as leucosomes, provide evidence for at least some melt being present in the sample at the time of metamorphism. The sample is devoid of quartz.

The interpreted peak metamorphic assemblage is biotite$_1$–garnet$_1$–orthopyroxene$_1$–spinel$_1$–plagioclase–K-feldspar–rutile–melt. The interpreted post-peak, retrograde minerals are sapphirine$_2$ and orthopyroxene$_2$ ($\pm$ plagioclase$_2$) followed by sillimanite$_3$, biotite$_3$ and plagioclase$_3$; and then garnet$_4$.

AK-5

In thin section the mineralogy of the rock is orthopyroxene, garnet, plagioclase, K-feldspar, quartz, sillimanite, rutile, sapphirine and cordierite. Post-peak reaction microstructures are well developed in this sample and occur in parts of the rock where garnet occurs (or is interpreted to have occurred) (Fig. 4a).

There is no evidence that sapphirine and quartz coexisted as part of a stable mineral assemblage in the sample. Ternary feldspar$_1$ (now exsolved to K-feldspar and plagioclase), orthopyroxene$_1$, quartz$_1$ and garnet$_1$ are coarse-grained and, except for garnet, are all in direct contact (Fig. 4b). Sillimanite$_1$ is extremely rare in the sample, occurring sporadically along grain boundaries of orthopyroxene$_1$ aggregates. Rutile occurs as small grains throughout the sample (Fig. 4b, 4c).

Around garnet is a rich record of mineral development (Fig. 4a, 4c). A multi-layered corona structure is comprised of symplectic intergrowth of Na-rich plagioclase$_2$ and ribs of sapphirine$_2$ and sillimanite$_2$ adjacent to garnet, Na-rich feldspar$_2$ and K-feldspar$_2$ between orthopyroxene$_2$ and the sapphirine-bearing symplectites, and an outer composite moat of orthopyroxene$_2$ and orthopyroxene$_1$ adjacent to the orthopyroxene$_1$–K-feldspar–quartz–plagioclase matrix (Fig. 4a). Rib-like sapphirine$_2$ grains are commonly mantled by coronas of sillimanite$_3$ and cordierite$_3$ (Fig. 4c). Leucosomes are not obvious in this rock at hand-specimen or thin section scale but melt is assumed to be present in (very) small quantities on the basis that the formation of retrograde products such as hydrous cordierite typically requires the presence of melt (Sawyer, 1999; Brown, 2002; Johnson & Brown, 2005; White & Powell, 2011; Korhonen et al., 2013a; Kelsey & Hand, 2015).

Small, irregularly-shaped garnet grains occur in the sapphirine-bearing symplectites and contains inclusions of rib-like sapphirine$_2$ and Na-rich plagioclase$_2$ and partly contains rib-like grains of sillimanite and sapphirine. These garnet grains are interpreted as late (garnet$_4$). Rare biotite occurs in the symplectic corona layer and also in the outermost orthopyroxene$_1$–orthopyroxene$_2$ corona. Due to the hydrous nature of biotite it is interpreted as late, possibly at a similar time to cordierite$_3$.

The interpreted peak metamorphic assemblage is orthopyroxene$_1$–garnet–sillimanite$_1$–quartz–K-feldspar$_1$–rutile (and melt), where K-feldspar is ternary feldspar. The post-peak minerals are interpreted to be sapphirine$_2$, plagioclase$_2$, K-feldspar$_2$, cordierite$_2$, biotite$_2$ and orthopyroxene$_2$, followed by sillimanite$_3$, cordierite$_3$, biotite$_3$, and then garnet$_4$.

AK-6

Coarse-grained garnet (up to 8 mm), K-feldspar (3–10 mm) and orthopyroxene (6–9 mm) occur as porphyroblasts within a matrix of very abundant quartz (Fig. 5b). Garnet contains rare inclusions of sapphirine, rutile and sillimanite (Fig. 5a). Garnet and orthopyroxene are separated by K-feldspar when they occur in proximity (Fig. 5a). Small (up to 1.5 mm) grains of rutile occur throughout the matrix. Rare (<<1%), tiny sillimanite grains occur in the matrix spatially distal from garnet and orthopyroxene. Biotite occurs around and in direct contact with orthopyroxene. Biotite contains very rare inclusions of rutile and sillimanite, suggesting that orthopyroxene may have formerly contained inclusions. Leucosomes are not obvious in this rock at hand-specimen or thin section scale as there are so few ferromagnesian minerals present but melt is assumed to be present in (very) small quantities on the basis that the formation of the retrograde product (hydrous biotite) typically requires the presence of melt.

64

The interpreted peak metamorphic assemblage is orthopyroxene–garnet–K-feldspar–quartz–rutile–melt. Prograde minerals are interpreted to be sillimanite, sapphirine and rutile. The post-peak minerals are interpreted to be biotite and K-feldspar. The significance of matrix sillimanite is unclear.

R31180

Coarse-grained sapphirine (2–8 mm) porphyroblasts are consistently and systematically separated from matrix quartz (2–8 mm) by either a two-layer corona of sillimanite (3–4 mm, inner layer adjacent to sapphirine) and orthopyroxene (3–4 mm diameter, outer layer) (Fig. 6a, 6b) or a three-layer corona of corundum (inner layer adjacent to sapphirine), sillimanite (middle layer) and orthopyroxene (outer layer, adjacent to quartz). The matrix is predominantly quartz, but additionally contains rare, very coarse mesoperthitic K-feldspar (up to 14 mm). The mesoperthitic K-feldspar is observed with small clusters of fine-grained biotite and quartz at its edges. Rutile is typically coarse-grained (2–4 mm) and occurs within the corona structure (Fig. 6a, 6b) as well as in the matrix. Leucosomes are not obvious from the thin section. However, the presence of coarse mesoperthitic K-feldspar may attest to melting reactions having taken place in the sample, and the presence of rare biotite may attest to the former presence of melt. The interpreted peak mineral assemblage is quartz–sapphirine–mesoperthitic K-feldspar–rutile–melt. Retrograde minerals are interpreted to be sillimanite, orthopyroxene, corundum and biotite.

APPENDIX B: ZIR DATA

Sample name	Inclusion/grain boundary hosted	distance from xenocrystic zircon (μm)	Zr %ERR from EPMA measurement	EPMA measured ZIR (ppm)
AK3 RB1a	Grain boundary	1040	2.37244	2390.42
AK3 RB1b	Grain boundary	1040	2.358	2446.48
AK3 RB1c	Grain boundary	1040	2.41057	2458.26
AK3 RF1	Grain boundary	50	3.90506	1275.47
AK3 RF2	Grain boundary	35	2.45749	2377.53
AK3 RF3	Grain boundary	1013	4.90008	981.03
AK3 RG1	Grain boundary	-	4.34334	1164.31
AK3 RGZ1	Grain boundary	-	5.55717	838.29
AK3 RI2	Inclusion	515	3.64587	1419.79
AK3 RIB1	Grain boundary	1172	2.496	2293.96
AK3 RIB2	Inclusion	55	2.5001	2311.93
AK3 RIB3	Grain boundary	25	2.69151	2061.29
AK3 RIB4	Grain boundary	350	4.90692	1012.27
AK3 RS1a	Grain boundary	155	2.4067	2355.88
AK3 RS1b	Grain boundary	220	2.3058	2487.12
AK3 RS1c	Grain boundary	200	3.1342	1702.34
AK3 RS2	Grain boundary	930	3.91739	1290.17
AK3 RS3	Grain boundary	830	6.1978	740.66
AK3 RS4	Grain boundary	870	3.06624	1770.92
AK3 RZ1	Grain boundary	60	4.79232	1016.42

AK3 RZ2a	Grain boundary	45	2.51861	1449.87
AK3 RZ2b	Grain boundary	45	2.84086	1675.78
AK3 RZ2c	Grain boundary	45	3.17276	1943.85
AK3 RZ2d	Grain boundary	45	3.58521	2256.27
AK3 RZ3a	Grain boundary	40	3.81408	1178.12
AK3 RZ3b	Grain boundary	40	4.07269	1244.46
AK3 RZ3c	Grain boundary	40	4.24158	1310.78
AK3 RZ3d	Grain boundary	40	3.84777	1326.5
AK3 RZ3e	Grain boundary	40	4.63379	1342.56
AK3 RZ3-2	Grain boundary	40	3.8392	1055.25
AK3 RZ4	Grain boundary	200	3.92463	1292.1
AK3 RZ5	Grain boundary	240	4.95076	973.4
AK3-2 RB1	Grain boundary	1250	4.11208	1248.1
AK3-2 RB2	Grain boundary	610	3.78347	1396.71
AK3-2 RB3	Grain boundary	1860	4.50082	1131.8
AK3-2 RGB1	Grain boundary	-	7.56939	602.33
AK3-2 RZ1	Grain boundary	235	4.11506	1253.8
AK3-2 RZ2a	Grain boundary	235	3.56934	1529.43
AK3-2 RZ2b	Grain boundary	235	3.34763	1696.64
AK3-2 RZ2c	Grain boundary	235	2.88784	1996.22
AK3-2 RZ3a	Grain boundary	1130	4.41474	944.43
AK3-2 RZ3b	Grain boundary	1130	4.72339	1065.88
AK3-2 RZ3c	Grain boundary	1130	3.49666	1088.84
AK3-2 RZ3d	Grain boundary	1130	4.2863	1147.21
AK3-2 RZ3e	Grain boundary	1130	5.3489	1208.33
AK3-2 RZ3f	Grain boundary	1130	4.69568	1550.37

AK3-2 RZ4	Grain boundary	650	4.51485	1133.45
AK5 GXMAP RB5	Grain boundary	820	4.07519	1215.97
AK5 GXMAP RB5	Grain boundary	820	3.62197	1216.86
AK5 GXMAP RB5	Grain boundary	820	4.04965	1395.45
AK5 GXMAP RB7	Grain boundary	45	4.87041	990.21
AK5 GXMAP RF1	Grain boundary	775	4.87042	1001.64
AK5 GXMAP RI2	Inclusion	500	2.50103	2235.98
AK5 GXMAP RIB1	Grain boundary	800	6.0164	756.17
AK5 GXMAP RZ4a	Grain boundary	200	4.63643	684.77
AK5 GXMAP RZ4b	Grain boundary	200	6.69667	1054.62
AK5 GXMAP RZ5a	Grain boundary	300	3.57678	852.2
AK5 GXMAP RZ5b	Grain boundary	300	5.58612	1430.55
AK5 GXMAP RZ6	Grain boundary	500	4.26497	1119.92
AK5 GXMAP1 RB1a	Grain boundary	1350	6.32637	720.88
AK5 GXMAP1 RB1b	Grain boundary	1350	4.48905	1083.48
AK5 GXMAP1 RB2a	Grain boundary	510	4.38063	1118.9
AK5 GXMAP1 RB2b	Grain boundary	510	4.23349	1134.5
AK5 GXMAP1 RB3	Grain boundary	722	3.26155	1621.6
AK5 GXMAP1 RB4	Grain boundary	770	2.83762	1905.85
AK5 GXMAP1 RI1	Inclusion	730	3.86901	1289.69
AK5 GXMAP1 RZ1a	Grain boundary	10	2.79553	1331.69
AK5 GXMAP1 RZ1b	Grain boundary	10	2.64655	1931.89
AK5 GXMAP1 RZ1c	Grain boundary	10	3.74431	2076.12
AK5 GXMAP1 RZ2a	Grain boundary	760	4.68922	918.42
AK5 GXMAP1 RZ2b	Grain boundary	760	5.11444	1019.41
AK5 GXMAP1 RZ3	Inclusion	1160	4.22652	1149.8

AK5 GXMAP1 RZ7a	Grain boundary	1044	6.91801	637.42
AK5 GXMAP1 RZ7b	Grain boundary	1044	6.27678	723.6
AK5 GXMAP1 RZ7c	Grain boundary	1044	4.43092	1102.42
AK5 GXMAP1 RZ7d	Grain boundary	1044	4.21927	1152.08
AK5 GXMAP1 RZ8	Grain boundary	1210	3.50678	1451.89
AK5 GXMAP1 RZ9	Grain boundary	1220	4.82587	997.47
AK5 RB6a	Grain boundary	930	3.27216	1400.6
AK5 RB6b	Grain boundary	930	3.66222	1601.67
AK5 RF2a	Inclusion	425	4.10729	1085.87
AK5 RF2b	Inclusion	425	4.36934	1185.66
AK5 RI3	Inclusion	700	4.25958	1146.15
AK5 RZ10	Grain boundary	660	3.67352	1360.6
AK5-2 RB1	Grain boundary	810	5.54121	866.18
AK5-2 RB2	Inclusion	500	3.62777	1385.33
AK5-2 RB3	Grain boundary	100	4.35463	1159.35
AK5-2 RB4	Inclusion	480	3.73787	1390.5
AK5-2 RB5a	Grain boundary	850	3.53472	1409.57
AK5-2 RB5b	Grain boundary	850	3.75158	1509.06
AK5-2 RF1a	Grain boundary	200	3.64548	1298.49
AK5-2 RF1b	Grain boundary	200	3.93709	1431.6
AK5-2 RF1c	Grain boundary	200	3.30564	1620.48
AK5-2 RF2	Inclusion	780	3.94868	1270.07
AK5-2 RI1	Grain boundary	1130	2.48932	2306.45
AK5-2 RI2	Grain boundary	1130	3.88012	1300.48
AK5-2 RIB1	Inclusion	120	2.98492	1801.72
AK5-2 RZ1	Grain boundary	740	4.33383	1142.24

AK5-2 RZ10	Inclusion	1150	4.75594	1029.61
AK5-2 RZ11	Grain boundary	225	4.94966	992.54
AK5-2 RZ2	Grain boundary	170	6.2235	754.99
AK5-2 RZ3	Grain boundary	535	5.0933	930.97
AK5-2 RZ4	Grain boundary	365	3.11001	1761.55
AK5-2 RZ5	Inclusion	420	5.9997	802.8
AK5-2 RZ6	Grain boundary	550	5.18049	937.64
AK5-2 RZ7	Grain boundary	1175	2.49062	2321.82
AK5-2 RZ8	Inclusion	870	4.16409	1226.58
AK5-2 RZ8	Inclusion	870	3.16223	1705.83
AK5-2 RZ9	Inclusion	895	4.05275	1245.63
AK6 GXMap RB1	Grain boundary	450	1.84862	3480.22
AK6 GXMap RB2	Grain boundary	480	1.94259	3238.64
AK6 GXMap RI1	Inclusion	450	1.85419	3405.31
AK6 GXMap RI2	Inclusion	490	2.21937	2677.53
AK6 GXMap RM1a	Grain boundary	70	1.8951	3310.99
AK6 GXMap RM1b	Grain boundary	40	1.7795	3646.77
AK6 GXMap RM1c	Grain boundary	250	1.74405	3756.4
AK6 GXMap RM1d	Grain boundary	100	1.66149	3974.06
AK6 GXMap RM2	Grain boundary	166	1.80339	3571.9
AK6 GXMap RM3	Inclusion	650	1.58416	4345.25
AK6 GXMap RM4	Grain boundary	75	1.58187	4323.08
AK6 GXMap1 RB3a	Grain boundary	420	1.60255	4260
AK6 GXMap1 RB3b	Grain boundary	420	1.66831	4030.99
AK6 GXMap1 RB4	Grain boundary	250	1.82046	3560.14
AK6 GXMap1 RB6	Grain boundary	520	1.6407	4162.06

AK6 GXMap1 RF1	Grain boundary	320	2.27649	2549.5
AK6 GXMap1 RI3a	Inclusion	200	1.66408	4037.37
AK6 GXMap1 RI3b	Inclusion	200	1.61163	4185.54
AK6 GXMap1 RIB1a	Inclusion	440	1.68306	3967.92
AK6 GXMap1 RIB1b	Inclusion	440	1.66015	4017.23
AK6 GXMap1 RIB1c	Inclusion	440	1.74045	3778.4
AK6 GXMap1 RIB1d	Inclusion	440	1.67202	3971.94
AK6 GXMap1 RM5	Inclusion	690	1.53157	4490.59
AK6 GXMap1 RM6	Grain boundary	450	1.6788	3971.64
AK6 GXMap1 RZ1	Grain boundary	1	10.5624	422.06
AK6 GXMap2 RB10	Grain boundary	200	2.33058	2466.52
AK6 GXMap2 RB11a	Grain boundary	40	1.61318	4214.94
AK6 GXMap2 RB11b	Grain boundary	300	1.57735	4344.05
AK6 GXMap2 RB12	Grain boundary	500	1.54377	4474.75
AK6 GXMap2 RB2a	Grain boundary	480	1.83561	3487.32
AK6 GXMap2 RB2c	Grain boundary	480	1.85971	3463.97
AK6 GXMap2 RB7	Grain boundary	670	1.75512	3722.17
AK6 GXMap2 RB8	Grain boundary	670	1.50601	4656.77
AK6 GXMap2 RB9	Grain boundary	840	1.54548	4425.62
AK6 GXMap2 RF2	Grain boundary	310	1.43847	4991.24
AK6 GXMap2 RI5	Inclusion	1500	1.65034	4071.17
AK6 GXMap2 RI6	Inclusion	400	1.68023	3941.28
AK6 GXMap2 RI7	Inclusion	1650	1.64584	4057.56
AK6 GXMap2 RIB2	Inclusion	100	1.50759	4696.46
AK6 GXMap2 RZ2	Inclusion	86	1.448	4957.72
AK6 GXMap2 RZ3	Grain boundary	0	1.45115	4902.56

AK6 GXMap2 RZ4	Grain boundary	620	1.65903	4035.71
AK6-2 RB1	Grain boundary	735	1.50511	4922.3
AK6-2 RB2a	Grain boundary	20	3.92435	922.56
AK6-2 RB2b	Grain boundary	20	3.59752	1030.31
AK6-2 RB2c	Grain boundary	20	3.69412	1036.47
AK6-2 RB2d	Grain boundary	20	4.27974	1147.86
AK6-2 RB2e	Grain boundary	20	4.39449	1173.43
AK6-2 RB2f	Grain boundary	20	3.94086	1209.02
AK6-2 RB2g	Grain boundary	20	3.92159	1230.67
AK6-2 RB2h	Grain boundary	20	3.91142	1231.23
AK6-2 RB2i	Grain boundary	20	4.09014	1274.82
AK6-2 RB2j	Grain boundary	20	4.32425	1286.09
AK6-2 RB2k	Grain boundary	20	4.47166	1351.08
AK6-2 RB2l	Grain boundary	20	4.96997	1366.51
AK6-2 RB2m	Grain boundary	20	5.3026	1367.15
AK6-2 RB2n	Grain boundary	20	4.82926	1443.37
AK6-2 RB2o	Grain boundary	20	4.24369	1488.39
AK6-2 RB3a	Grain boundary	185	1.44597	5165.85
AK6-2 RB3b	Grain boundary	185	1.45265	5174.74
AK6-2 RB4a	Grain boundary	460	1.53174	4808.75
AK6-2 RB4b	Grain boundary	460	1.50663	4901.27
AK6-2 RB4c	Grain boundary	460	1.49304	4931.14
AK6-2 RB4d	Grain boundary	460	1.50807	4942.72
AK6-2 RB4e	Grain boundary	460	1.42586	5368.71
AK6-2 RF1a	Grain boundary	1200	1.59011	3471.07
AK6-2 RF1b	Grain boundary	1200	1.4986	4473.14

AK6-2 RF1c	Grain boundary	1200	1.50368	4573.35
AK6-2 RF1d	Grain boundary	1200	1.83469	4636.56
AK6-2 RF1e	Grain boundary	1200	1.56564	4681.23
AK6-2 RF2	Grain boundary	140	1.87458	3575.62
AK6-2 RF3	Grain boundary	920	1.49934	4917.8
AK6-2 RF4	Grain boundary	1150	1.69322	4104.37
AK6-2 RF5	Inclusion	1060	1.48131	5009.41
AK6-2 RF6	Grain boundary	100	1.65234	4282.44
AK6-2 RZ1	Inclusion	35	3.6188	1409.85
AK6-2 RZ2	Grain boundary	650	1.64612	4318.07
AK6-2 RZ3a	Grain boundary	1100	1.58157	3957.41
AK6-2 RZ3b	Grain boundary	1100	1.74555	4483.1
AK6-2 RZ4	Grain boundary	600	1.7126	4032.02
AK6-2 RZ5	Grain boundary	1140	1.57581	4566.62
R31180 GXMAP RB5	Grain boundary	900	6.89887	655.35
R31180 GXMAP RB6	Grain boundary	1300	6.50179	712.04
R31180 GXMAP RI1	Inclusion	620	21.3422	193.23
R31180 GXMAP RI2	Inclusion	930	9.60186	455.88
R31180 GXMAP RI3	Inclusion	865	17.3587	245.38
R31180 GXMAP RIB3	Grain boundary	365	13.9852	301.35
R31180 GXMAP RIB4	Grain boundary	340	12.7627	333.5
R31180 GXMAP RIB5	Grain boundary	1630	7.06221	636.89
R31180 GXMAP RIB6a	Grain boundary	1550	7.42153	588.46
R31180 GXMAP RIB6b	Grain boundary	1550	7.50974	604.47
R31180 GXMAP1 RZ3a	Grain boundary	15	9.86738	396.91
R31180 GXMAP1 RZ3b	Grain boundary	15	7.61395	443.33

R31180 GXMAP1 RZ3c	Grain boundary	15	6.8335	564.57
R31180 GXMAP1 RZ3d	Grain boundary	15	6.58007	587.04
R31180 GXMAP1 RZ3e	Grain boundary	15	6.62465	664.15
R31180 GXMAP1 RZ3f	Grain boundary	15	5.97479	688.42
R31180 GXMAP1 RZ3g	Grain boundary	15	7.50777	690.99
R31180 GXMAP1 RZ3h	Grain boundary	15	6.32799	692.51
R31180 GXMAP1 RZ3i	Grain boundary	15	6.49292	727.01
R31180 GXMAP1 RZ3j	Grain boundary	15	11.1316	779.75
R31180 GXMAP2 RB7	Grain boundary	180	7.72998	583.13
R31180 GXMAP2 RF2	Grain boundary	10	10.1955	433.29
R31180 GXMAP2 RF3	Grain boundary	350	21.5257	194.82
R31180 GXMAP3 RIB1	Grain boundary	2500	5.38671	879.6
R31180 GXMAP3 RIB2	Grain boundary	2500	17.6893	236.51
R31180 RB1	Grain boundary	70	8.38497	539.8
R31180 RB2a	Grain boundary	1475	4.98884	828.02
R31180 RB2b	Grain boundary	1475	5.64315	882.53
R31180 RB2c	Grain boundary	1475	5.31363	930.12
R31180 RB2d	Grain boundary	1475	5.11136	937.99
R31180 RB2e	Grain boundary	1475	5.09975	949.12
R31180 RB3a	Grain boundary	160	6.28834	365.12
R31180 RB3b	Grain boundary	1160	8.12547	495.58
R31180 RB3c	Grain boundary	1160	11.758	522.78
R31180 RB3d	Grain boundary	1160	9.05889	547.14
R31180 RB3e	Grain boundary	1160	8.40475	661.56
R31180 RB3f	Grain boundary	1160	6.7347	683.91
R31180 RB3g	Grain boundary	1160	6.6095	744.94

R31180 RF1a	Grain boundary	1145	6.95361	611.14
R31180 RF1b	Grain boundary	145	6.60685	662.31
R31180 RF1c	Grain boundary	1145	6.73829	684.94
R31180 RF1d	Grain boundary	1145	7.56036	697.85
R31180 RM1	Grain boundary	910	7.34878	616.46
R31180 RZ1	Grain boundary	1030	7.43466	605.73
R31180 RZ2	Grain boundary	640	9.61677	463.37
R31180 RZ4	Grain boundary	950	13.1321	326.02
R31180-2 RB1	Grain boundary	720	9.22617	486.34
R31180-2 RB2a	Grain boundary	633	5.55103	852.47
R31180-2 RB2b	Grain boundary	633	4.93189	981.55
R31180-2 RF1	Inclusion	3000	12.3637	346.43
R31180-2 RF2	Grain boundary	3000	22.2737	189.3
R31180-2 RI1	Inclusion	350	5.79726	794.05
R31180-2 RI2	Grain boundary	200	13.5912	323.29
R31180-2 RZ1a	Grain boundary	15	9.65915	376.37
R31180-2 RZ1b	Grain boundary	15	6.24024	420.64
R31180-2 RZ1c	Grain boundary	15	6.55283	445.29
R31180-2 RZ1d	Grain boundary	15	8.27823	558.71
R31180-2 RZ1e	Grain boundary	15	10.9066	628.23
R31180-2 RZ1f	Grain boundary	15	11.763	640.85
R31180-2 RZ1g	Grain boundary	15	7.3026	677.03
R31180-2 RZ1h	Grain boundary	15	6.11213	723.15
R31180-2 RZ1i	Grain boundary	15	5.8959	750.47
R31180-2 RZ1j	Grain boundary	15	7.06138	754.71
R31180-2 RZ1k	Grain boundary	15	6.25639	786.54

R31180-2 RZ1l	Grain boundary	15	6.46546	788.51
R31180-2 RZ1m	Grain boundary	15	5.96558	794.78
R31180-2 RZ2	Inclusion	1365	6.79661	680.08
R31180-2 RZ3a	Grain boundary	65	12.0778	363.42
R31180-2 RZ3b	Grain boundary	65	8.78567	502.87
R31180-2 RZ4	Inclusion	130	17.6129	245.76

Appendix C: Reintegrated ZIR data

Sample name	Initial ZIR (ppm)	Micro structural location	Reintegrated ZIR (ppm)	ΔZIR
AK3 RF1	1275.47	Grain boundary	3617.97953	2342.51
AK3 RZ1	1016.42	Grain boundary	9732.800237	8716.38
AK3 RZ3a	1178.12	Grain boundary	9182.479104	8004.359
AK3 RZ3b	1244.46	Grain boundary	9247.749568	8003.29
AK3 RZ3c	1310.78	Grain boundary	9313.000355	8002.22
AK3 RZ3d	1326.5	Grain boundary	9328.466917	8001.967
AK3 RZ3e	1342.56	Grain boundary	9344.267997	8001.708
AK3 RZ3-2	1055.25	Grain boundary	12787.33654	11732.09
AK3 RZ4	1292.1	Grain boundary	4237.843113	2945.743
AK3 RZ5	973.4	Grain boundary	12728.30868	11754.91
AK3-2 RB1	1248.1	Grain boundary	1646.750793	398.6508
AK3-2 RB2	1396.71	Grain boundary	3998.57907	2601.869
AK3-2 RZ1	1253.8	Grain boundary	10357.14119	9103.341
AK3-2 RZ3a	944.43	Grain boundary	4951.966155	4007.536
AK3-2 RZ3b	1208.33	Grain boundary	8651.255092	7442.925
AK5 GXMAP1 RI1	1289.69	Inclusion	2452.481533	1162.792
AK5 GXMAP1 RZ3	1149.8	Inclusion	19090.93761	17941.14
AK5-2 RZ10	1029.61	Inclusion	9114.628557	8085.019
AK5-2 RZ5	802.8	Inclusion	16214.90344	15412.1
AK5-2 RZ8a	1226.58	Inclusion	1558.941885	332.3619
AK5-2 RZ8b	1705.83	Inclusion	2037.87175	332.0417
AK5-2 RZ9	1245.63	Inclusion	5308.153191	4062.523
AK5 GXMAP RB5a	1215.97	Grain boundary	3108.871298	1892.901

AK5 GXMAP RB5b	1216.86	Grain boundary	3109.761717	1892.902
AK5 GXMAP RB5c	1395.45	Grain boundary	3287.674612	1892.225
AK5 GXMAP RZ4a	684.77	Grain boundary	5435.681289	4750.911
AK5 GXMAP RZ4b	1054.62	Grain boundary	5801.986313	4747.366
AK5 GXMAP RZ5a	852.2	Grain boundary	15847.02724	14994.83
AK5 GXMAP RZ5b	1430.55	Grain boundary	16407.89225	14977.34
AK5 GXMAP1 RB2a	1118.9	Grain boundary	4393.93435	3275.034
AK5 GXMAP1 RB2b	1134.5	Grain boundary	4409.42487	3274.925
AK5 GXMAP1 RZ1a	1331.69	Grain boundary	2364.340793	1032.651
AK5 GXMAP1 RZ1b	1931.89	Grain boundary	2963.294215	1031.404
AK5 GXMAP1 RZ1c	2076.12	Grain boundary	3107.226238	1031.106
AK5 GXMAP1 RZ2a	918.42	Grain boundary	3408.228179	2489.808
AK5 GXMAP1 RZ2b	1019.41	Grain boundary	3508.707024	2489.297
AK5 GXMAP1 RZ7a	637.42	Grain boundary	13828.28089	13190.86
AK5 GXMAP1 RZ7b	723.6	Grain boundary	13912.20045	13188.6
AK5 GXMAP1 RZ7c	1102.42	Grain boundary	14280.99416	13178.57
AK5 GXMAP1 RZ7d	1152.08	Grain boundary	14329.36286	13177.28
AK5 GXMAP1 RZ8	1451.89	Grain boundary	4033.795847	2581.906
AK5 GXMAP1 RZ9	997.47	Grain boundary	22786.26466	21788.79
AK5 RZ10	1360.6	Grain boundary	3661.454208	2300.854
AK5-2 RB1	866.18	Grain boundary	8974.301206	8108.121
AK5-2 RZ1	1142.24	Grain boundary	15010.90766	13868.67
AK5-2 RZ11	992.54	Grain boundary	2495.559031	1503.019
AK5-2 RZ2	754.99	Grain boundary	7566.681475	6811.691
AK5-2 RZ3	930.97	Grain boundary	8375.797204	7444.827
AK5-2 RZ4	1761.55	Grain boundary	2337.429768	575.8798

AK5-2 RZ6	937.64	Grain boundary	8656.552701	7718.913
AK5-2 RZ7	2321.82	Grain boundary	7187.351013	4865.531
AK6 GXMap RI1	3405.31	Inclusion	8625.741629	5220.432
AK6 GXMap2 RI5	4071.17	Inclusion	9870.78199	5799.612
AK6-2 RZ1	1409.85	Inclusion	11825.82551	10415.98
AK6 GXMap RB2	3238.64	Grain boundary	12351.49021	9112.85
AK6 GXMap RM4	4323.08	Grain boundary	12500.54835	8177.468
AK6 GXMap1 RB3a	4260	Grain boundary	5533.325241	1273.325
AK6 GXMap1 RB3b	4030.99	Grain boundary	5304.908716	1273.919
AK6 GXMap2 RB7	3722.17	Grain boundary	15486.81534	11764.65
AK6-2 RF6	4282.44	Grain boundary	6554.064161	2271.624
AK6-2 RZ3a	3957.41	Grain boundary	8908.509841	4951.1
AK6-2 RZ3b	4483.1	Grain boundary	9428.91967	4945.82
AK6-2 RZ5	4566.62	Grain boundary	87407.17452	82840.55
R31180 GXMAP RI1	193.23	Inclusion	1550.493665	1357.264
R31180-2 RZ2	680.08	Inclusion	2288.344736	1608.265
R31180 GXMAP1 RZ3a	396.91	Grain boundary	6791.291456	6394.381
R31180 GXMAP1 RZ3b	443.33	Grain boundary	6837.127604	6393.798
R31180 GXMAP1 RZ3c	564.57	Grain boundary	6956.757707	6392.188
R31180 GXMAP1 RZ3d	587.04	Grain boundary	6979.041703	6392.002
R31180 GXMAP1 RZ3e	664.15	Grain boundary	7055.147638	6390.998
R31180 GXMAP1 RZ3f	688.42	Grain boundary	7079.002823	6390.583
R31180 GXMAP1 RZ3g	690.99	Grain boundary	7081.57835	6390.588
R31180 GXMAP1 RZ3h	692.51	Grain boundary	7083.117375	6390.607
R31180 GXMAP1 RZ3i	727.01	Grain boundary	7117.186749	6390.177
R31180 GXMAP1 RZ3j	779.75	Grain boundary	7169.184531	6389.435

R31180 RB1	539.8	Grain boundary	3694.929863	3155.13
R31180 RB3	365.12	Grain boundary	504.3430818	139.2231
R31180 RZ1	605.73	Grain boundary	7375.019869	6769.29
R31180 RZ2	463.37	Grain boundary	11981.62565	11518.26
R31180 RZ4	326.02	Grain boundary	10848.25809	10522.24
R31180-2 RZ1a	376.37	Grain boundary	6196.571183	5820.201
R31180-2 RZ1b	420.64	Grain boundary	6240.334975	5819.695
R31180-2 RZ1c	445.29	Grain boundary	6264.708299	5819.418
R31180-2 RZ1d	558.71	Grain boundary	6376.89501	5818.185
R31180-2 RZ1e	628.23	Grain boundary	6445.554913	5817.325
R31180-2 RZ1f	640.85	Grain boundary	6457.992178	5817.142
R31180-2 RZ1g	677.03	Grain boundary	6493.819108	5816.789
R31180-2 RZ1h	723.15	Grain boundary	6539.38786	5816.238
R31180-2 RZ1i	750.47	Grain boundary	6566.423345	5815.953
R31180-2 RZ1j	754.71	Grain boundary	6570.473356	5815.763
R31180-2 RZ1k	786.54	Grain boundary	6601.989477	5815.449
R31180-2 RZ1l	788.51	Grain boundary	6603.948129	5815.438
R31180-2 RZ1m	794.78	Grain boundary	6610.168175	5815.388
R31180-2 RZ3a	363.42	Grain boundary	1031.179888	667.7599
R31180-2 RZ3b	502.87	Grain boundary	1170.441383	667.5714

Appendix D: LA-ICP-MS

METHODS

U–Pb geochronology was done using the Resonetics ASI M50 laser coupled with an
Agilent 7700 ICP–MS at Adelaide Microscopy. Prior to dating, high resolution reflected
light images were taken using an optical microscope to aid in determining the
microstructural location of monazite grains. U–Pb analyses were acquired in a He
ablation atmosphere with a frequency of 5 Hz and a spot size of 20 μm.

The primary monazite standard MAdel (TIMS normalisation data: $^{207}Pb/^{206}Pb = 491.0 \pm$
2.7 Ma, $^{206}Pb/^{238}U = 518.37 \pm 0.99$ Ma and $^{207}Pb/^{235}U = 513.13 \pm 0.19$ Ma: updated
from Payne et al. (2008) with additional TIMS analyses) was utilised to account for
elemental fractionation and mass bias. Data accuracy was monitored using secondary
monazite standards 222 (SHRIMP data: $^{206}Pb/^{238}U$ 450.2 ± 3.4 Ma) and Ambat (c. 525
Ma). Bracketing monazite runs with standards accounted for instrument drift. During
the course of this study the data collected on standards was: MAdel standards reported a
mean $^{206}Pb/^{238}U$ age of 518.4 ± 10.35 Ma (n=20), 222 gave a mean $^{206}Pb/^{238}U$ age of
447.7 ± 8 Ma (n=12), and Ambat gave a mean $^{206}Pb/^{238}U$ age of 514 ± 11.5 Ma (n=8).
All data quoted are at the two-sigma level.

AK-3

Twenty-four (24) monazite grains from sample AK-3 were in situ analysed by laser
ablation. The majority of data (n=21) is concordant (concordancy >90% and <110%)
and defines a spread along concordia of $^{206}Pb/^{238}U$ ages between 882 ± 19 Ma and 945 ±
18 Ma. Concordia, intercept and weighted mean ages were not calculated due to the

spread of data. Of the remaining data, one data point gave a $^{206}Pb/^{238}U$ age of 507 ± 9.8 Ma, and the final two data gave $^{206}Pb/^{238}U$ spot age results of 1464 ± 40 Ma and 1501 ± 43 Ma.

AK-5

Eight (8) monazite grains from sample AK-5 were also analysed by laser ablation. The limited data collected from this sample has two main age 'clusters'. The first, comprising two data points, has concordant (concordancy >90% and <110% concordant) $^{206}Pb/^{238}U$ spot ages of 813 ± 14 and 837 ± 13 Ma. The second age range contains three concordant data points ranging between 887 ± 17 Ma and 923 ± 7.9 Ma. Due to the limited size of the dataset it is not possible to calculate any meaningful weighted mean ages for the sample.

In situ monazite geochronology was not collected from samples AK-6 and R31180 as there was insufficient monazite in the thin sections to be able to define an age population. As geochronology was not the primary focus of the project this was deemed reasonable. Zircon is more abundant than monazite in these samples.

Monazite is a U–Pb chronometer widely applied to constraining high-temperature crustal/tectonic processes. As UHT conditions are thought to be close to or even exceed the temperature at which Pb diffusion in monazite is open to resetting (Cherniak et al., 2004), monazite age data may be interpreted as closure ages. However, in dry rocks such as UHT granulites, it has been argued that monazite can remain closed to Pb diffusion at extreme temperatures (approximately >1000 °C; Sajeev et al., 2010; Schmitz & Bowring, 2003; Walsh et al., 2015). Further, monazite growth in granulite facies rocks is thought to be largely a consequence of crystallisation from melt during the retrograde evolution (Kelsey et al., 2008; Yakymchuk & Brown, 2014), as UHT

conditions are through to be close to or exceed the temperature at which all existing (prograde) monazite dissolves into melt (Rapp et al., 1987, Kelsey et al., 2008; Stepanov et al., 2012). In actuality, monazite age data from UHT rocks may some combination of all the above possibilities, as well as from recrystallisation due to deformation, giving rise to the common 'smear' of age data along concordia. Monazite U–Pb geochronology was undertaken on two of the Anakapalle samples to broadly constrain the age of metamorphism. There is no published isotopic age data for the Anakapalle locality, only monazite chemical age data obtained by EPMA analysis (Simmat & Raith, 2008). Therefore, the data presented in this study is to confirm that metamorphism at Anakapalle is effectually the same age as UHT metamorphism elsewhere in the Eastern Ghats Province (Korhonen et al., 2013). Age data from sample AK-3 older than 1000 Ma is interpreted to be of detrital origin, located in the interiors of large monazite grains, analogous to Simmat & Raith (2008). The spread of age data from 882 ± 19 Ma to 945 ± 18 Ma along concordia are interpreted to define the age and partial duration of UHT metamorphism at Anakapalle. I attribute the spread of age data to a process of continual growth and/or recrystallisation as the retrograde evolution proceeded. The abundance of monazite amongst the symplectite, rather than in coarse-grained minerals, may suggest that the symplectite-forming reaction helped drive monazite production. The age spread is consistent at least partly with the spread of the majority of recent age data (c. 970–930 Ma) (Korhonen et al., 2013), which they attribute to crystallisation of monazite from crystallising melt during cooling. They attribute younger ages to a cryptic fluid-infiltration event. The age data for AK-3 is closely consistent with EPMA monazite age data for numerous parts of the Eastern Ghats Province (e.g. the western khondalite, charnockite–migmatite and eastern

khondalite zones shown in Fig. 1) including that from Anakapalle (see fig. 9 in Simmat & Raith, 2008). Leptynite (garnet–biotite gneiss) dated by Simmat & Raith from Anakapalle shows a major age peak at 907 ± 22 Ma, which coincides extremely well with the isotopic data from AK-3. Mg–Al-rich granulite (analogous to sample AK-3) dated by Simmat & Raith from Anakapalle shows many older (>1000 Ma) ages that are chiefly hosted within relict $garnet_1$, the most significant age peak is at 980 ± 25 Ma (interpreted a $garnet_1$ growth age) and few data are < c. 950 Ma. However, spot ages of 945 ± 24 Ma from monazite located in the sapphirine–orthopyroxene symplectites are interpreted to date decompression (Simmat & Raith, 2008). The similarity between this age and the dominant spread of ages in this study (882 ± 19 Ma to 945 ± 18 Ma) suggests that the amount of common Pb in monazite in this sample is low.

With the total geochronology dataset I have collected it is not possible to argue definitively for any particular interpretation made by Korhonen et al. (2013) or Simmat & Raith (2008). However, importantly, my age data is broadly comparable to the known ages of UHT metamorphism in the Eastern Ghats Province. Indeed, Korhonen argue that the total timescale of UHT metamorphism in the Province is unconstrained, but potentially as long as 200 Ma. As their geochronology samples are from rocks preserving the apparently earlier anticlockwise-style $P–T$ evolution, the concordant age data from Anakapalle in this study raises the possibility that a previously unrecognised younger component of UHT metamorphism in the Province is present at the Anakapalle locality as a consequence of it preserving the apparently later, clockwise-style $P–T$ evolution.
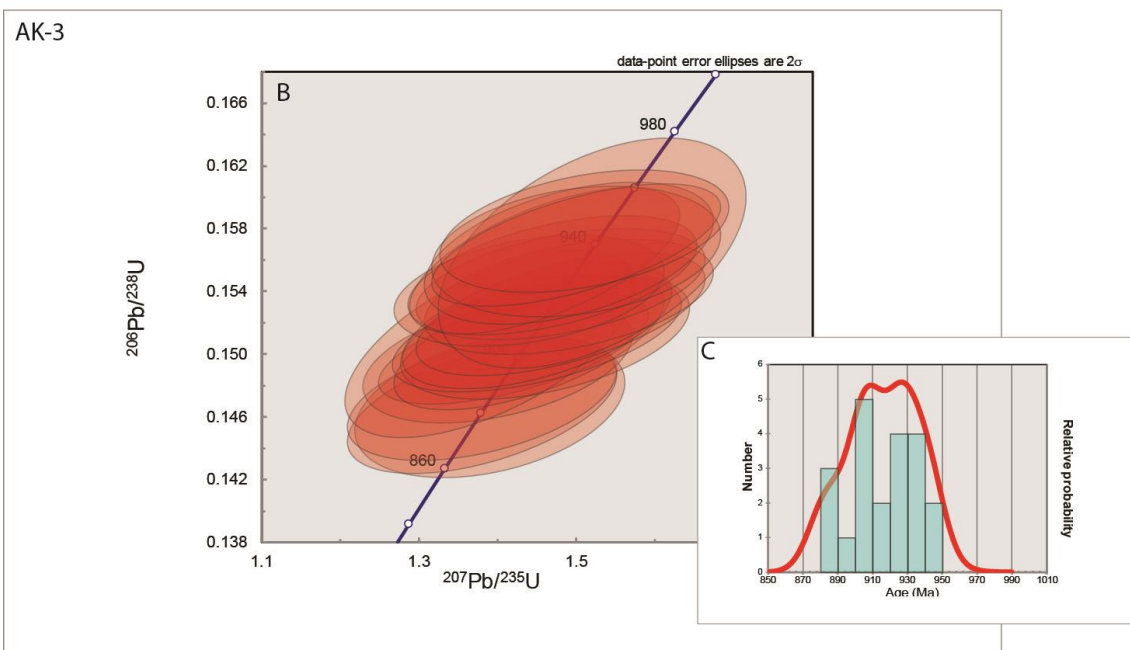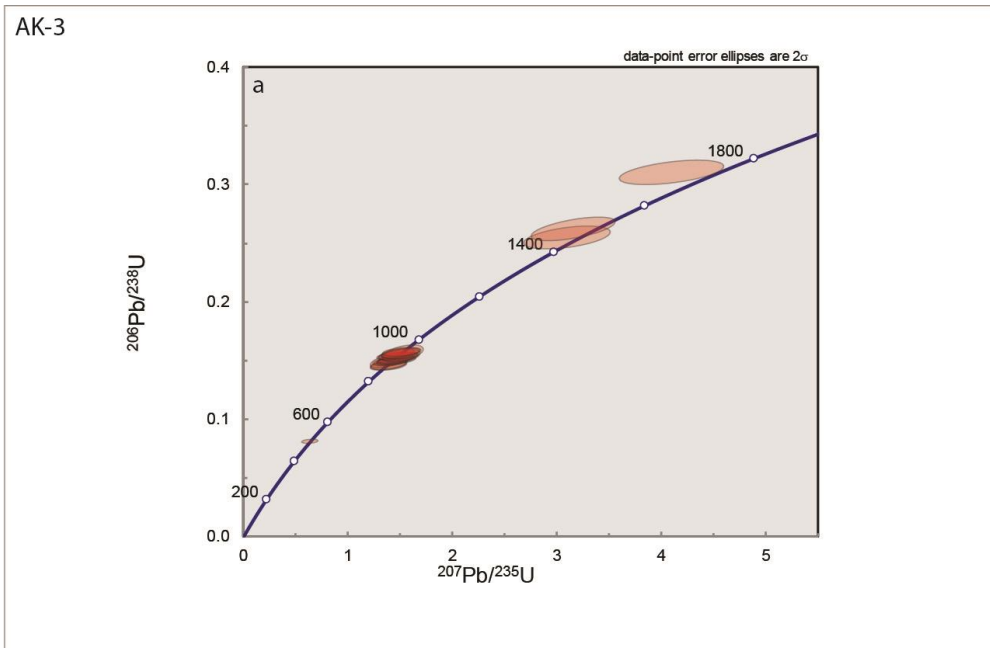
**In situ monazite U–Pb geochronology results for sample AK-3 (n = 25). (A) All data for AK-3 regardless of concordancy. Most data define a spread of data between 882 ± 19 Ma and 945 ± 18 Ma (^{206}Pb/^{238}U ages); (B) Close up of n=22 concordant data that define a spread of ^{206}Pb/^{238}U ages between 882 ± 19 Ma and 945 ± 18 Ma; (C) Probability density plot of the concordant data in B (n=22).**
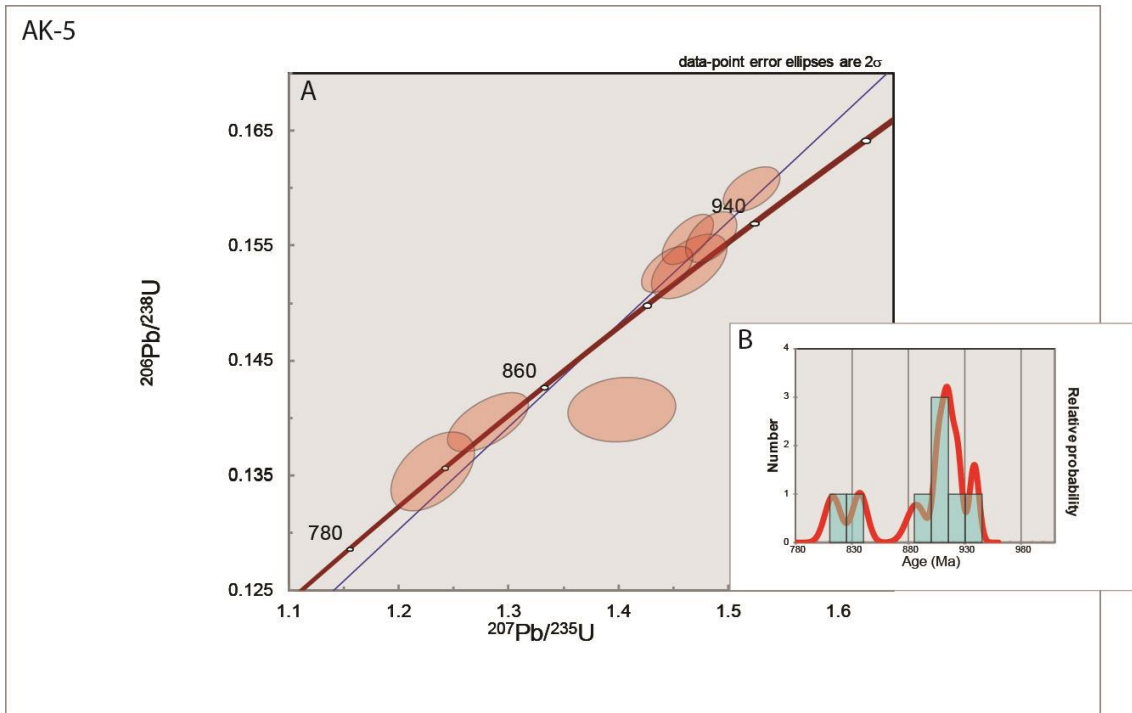
In situ monazite U–Pb geochronology results for sample AK-5 (n = 8). (A) The majority of concordant data (n = 5) cluster from 906.4 ± 8.1 Ma to 923 ± 7.9 Ma (all ages quoted are $^{206}Pb/^{238}U$ ages). Two data present results of 813 ±14 and 837 ± 13 Ma. The remaining data point has an age of 887 ± 17 Ma. (B) Probability density plot of geochronology data for sample AK-5.
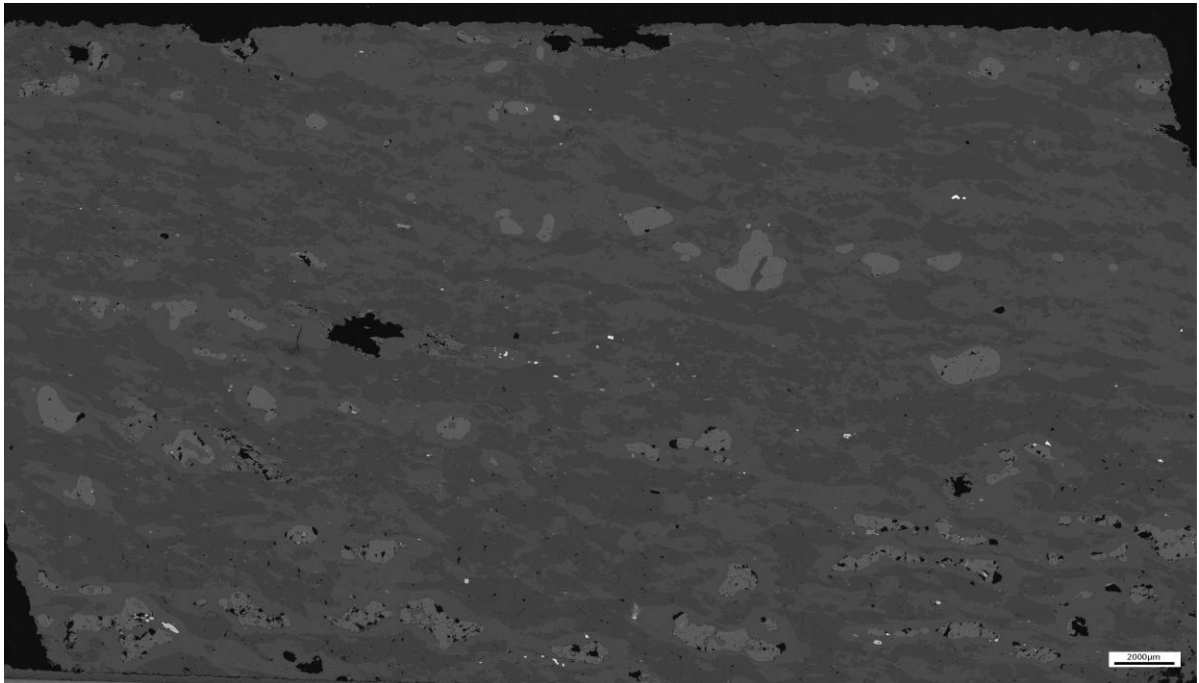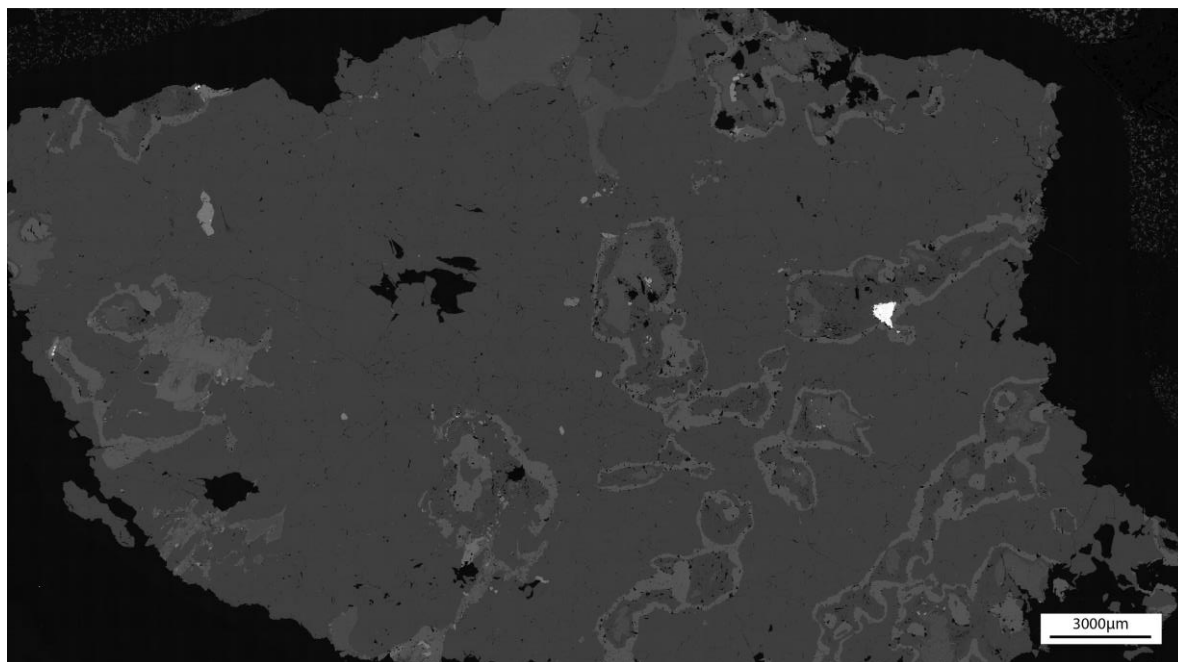
Appendix E: SEM/MLA maps
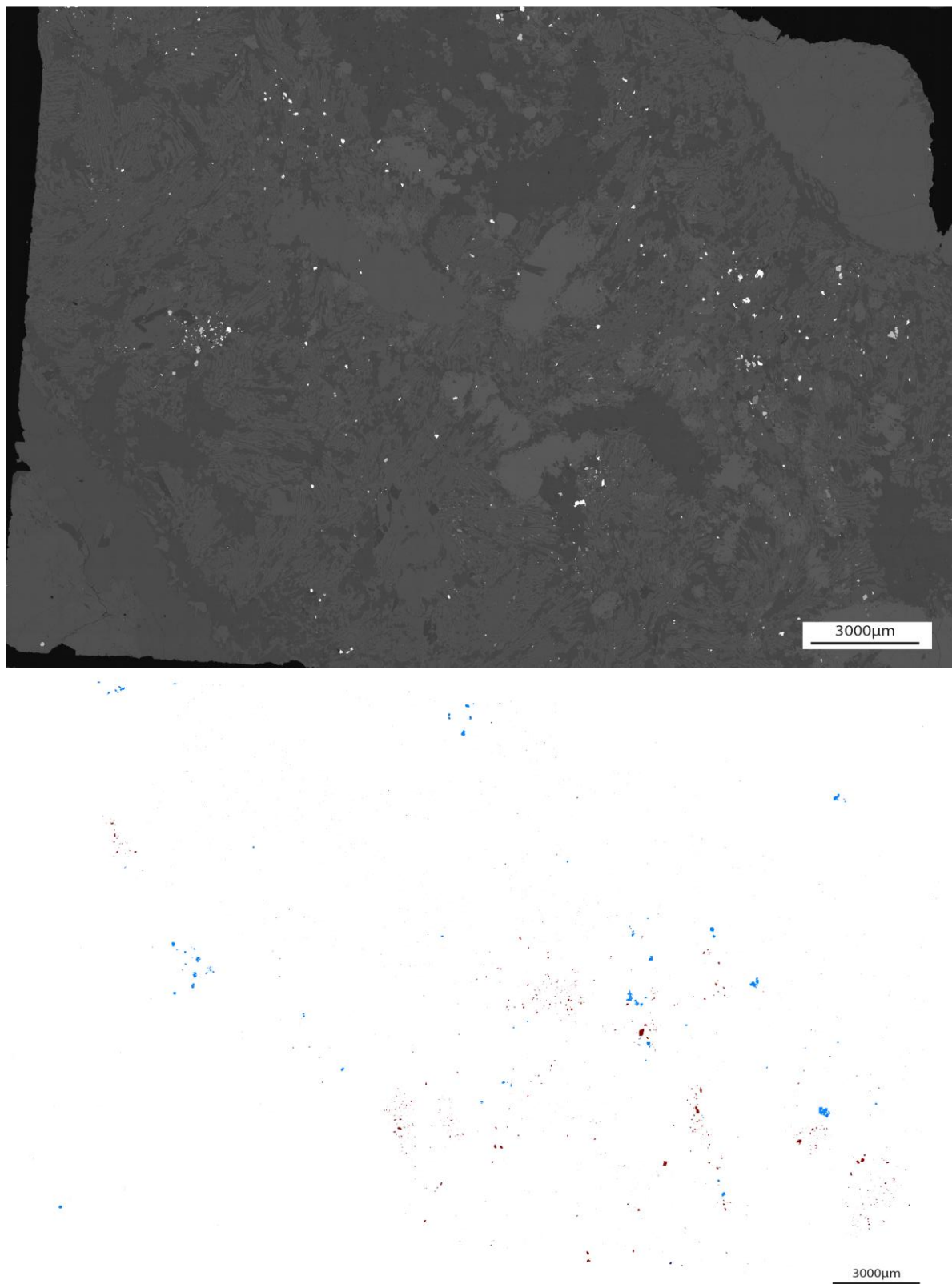
Full SEM and MLA maps for sample AK-3 used to calculate total rutile and zircon abundances, as well as distance from rutile to xenocrystic zircon
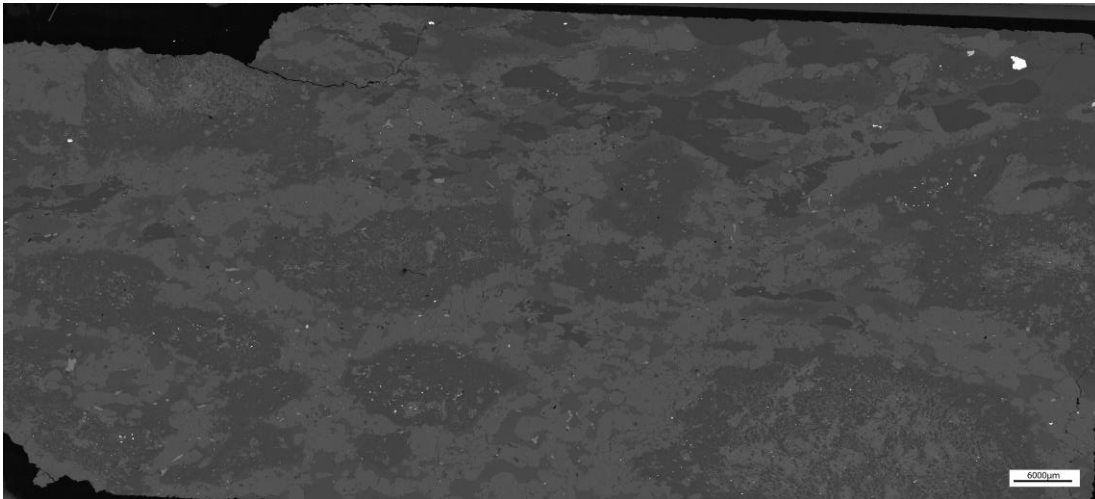
Full SEM and MLA maps for sample AK-5 used to calculate total rutile and zircon abundances, as well as distance from rutile to xenocrystic zircon
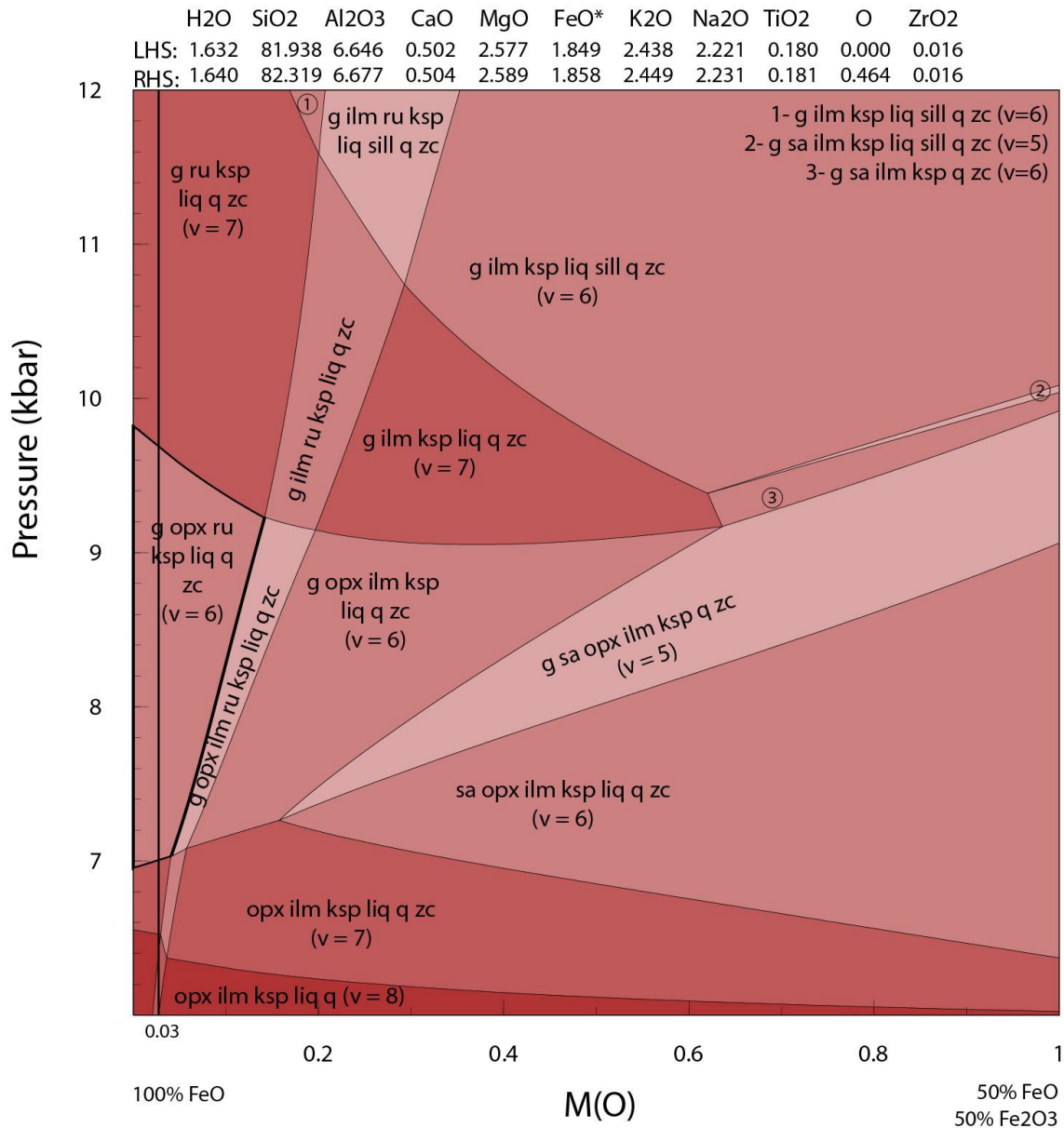
Full SEM and MLA maps for sample AK-6 used to calculate total rutile and zircon abundances, as well as distance from rutile to xenocrystic zircon

Full SEM and MLA maps for sample R31180 used to calculate total rutile and zircon abundances, as well as distance from rutile to xenocrystic zircon

Appendix F: P-M(O) and P-M(H₂O) Phase Diagrams for sample AK-6

P-MO AK-6

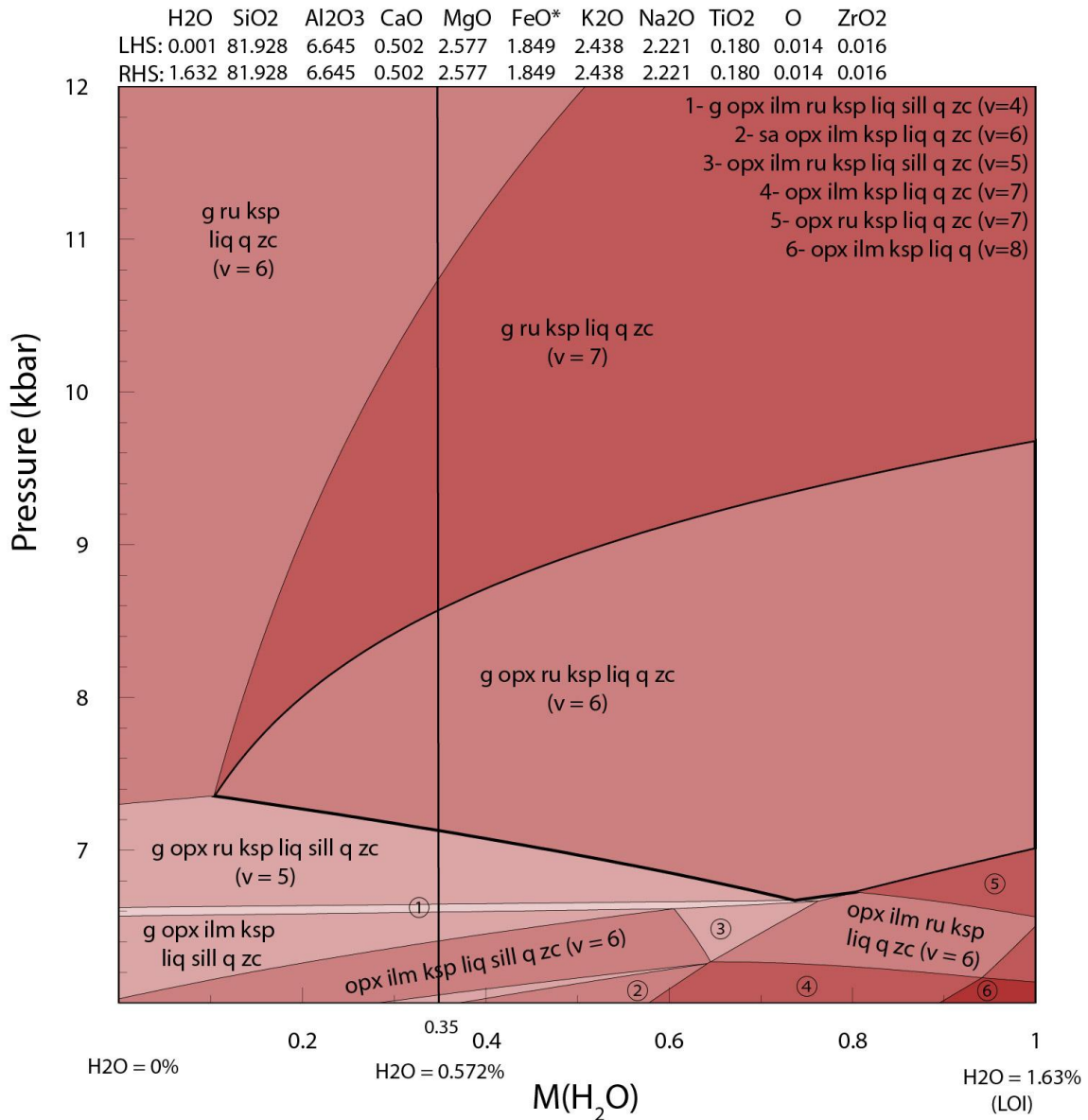|	H2O	SiO2	Al2O3	CaO	MgO	FeO*	K2O	Na2O	TiO2	O	ZrO2
LHS:	1.632	81.938	6.646	0.502	2.577	1.849	2.438	2.221	0.180	0.000	0.016
RHS:	1.640	82.319	6.677	0.504	2.589	1.858	2.449	2.231	0.181	0.464	0.016

Calculated *P–M*$_O$ pseudosection at 1020 °C for sample AK-6. Abbreviations: ilm = ilmenite; g = garnet; ksp = K-feldspar; liq = silicate melt; opx = orthopyroxene; q = quartz; ru = rutile; sa = sapphirine; sill = sillimanite; zc = zircon. The compositions (in mole%) used to calculate the pseudosection are provided above the diagram, where the top line represents that at *M*=0 (left-hand side) and the bottom line represents that at *M*=1 (right-hand side). FeO* = FeO + 2×'O'. This shows how phases change with varying oxidation state in the rock. From this diagram, an oxidation state can be chosen on the basis of mineralogy in the rock (bold vertical line)

The P–M_O pseudosection calculated at 1020 °C for sample AK-6 is shown above. The peak assemblage of orthopyroxene–garnet–K-feldspar–quartz–rutile–melt, which is stable in compositions with low Fe_2O_3 contents (left-hand side of diagram). The chosen oxidation state corresponds to the composition at $M_O = 0.03$ on the basis that the rock is rutile- rather than ilmenite-bearing. Compositions more oxidised than that at $M_O = 0.03$ would result in ilmenite-bearing assemblages occurring at pressures increasingly similar to the peak pressure for this sample.

Using the composition at oxidation state $M_O = 0.03$, the P–M_{H2O} pseudosection calculated at 1020 °C for sample AK-6 is shown below. The peak assemblage field occurs as a large field (outlined by bold boundaries) greater than $M_{H2O} = 0.1$. Due to the rarity of sillimanite and biotite in the sample, the composition chosen for the calculation of the P–T pseudosection is at $M_{H2O} = 0.35$. This composition is a trade-off between too much biotite to higher M_{H2O} (biotite not shown as temperature of diagram exceeds biotite stability but its stability is enhanced by higher H_2O amounts) and too much sillimanite stability at lower M_{H2O}.

P-MH2O AK-6

	H2O	SiO2	Al2O3	CaO	MgO	FeO*	K2O	Na2O	TiO2	O	ZrO2
LHS:	0.001	81.928	6.645	0.502	2.577	1.849	2.438	2.221	0.180	0.014	0.016
RHS:	1.632	81.928	6.645	0.502	2.577	1.849	2.438	2.221	0.180	0.014	0.016

1- g opx ilm ru ksp liq sill q zc (v=4)
2- sa opx ilm ksp liq q zc (v=6)
3- opx ilm ru ksp liq sill q zc (v=5)
4- opx ilm ksp liq q zc (v=7)
5- opx ru ksp liq q zc (v=7)
6- opx ilm ksp liq q (v=8)

Calculated *P–M*H2O pseudosection at 1020 °C for sample AK-6. Abbreviations: ilm = ilmenite; g = garnet; ksp = K-feldspar; liq = silicate melt; opx = orthopyroxene; q = quartz; ru = rutile; sa = sapphirine; sill = sillimanite; zc = zircon. The compositions (in mole%) used to calculate the pseudosection are provided above the diagram, where the top line represents that at *M*=0 (left-hand side) and the bottom line represents that at *M*=1 (right-hand side). FeO* = FeO + 2×'O'. This diagram allows the amount of fluid in the rock to be estimated (bold vertical line), by showing changes in mineralogy and mineral proportions as a function of pressure and H₂O content

Appendix G: Compatibility diagram and justification for peak assemblage of R31180

In the simple MgO–Al$_2$O$_3$–SiO$_2$ system in which reactions between sapphirine, orthopyroxene, sillimanite, quartz and cordierite can be depicted, natural rock compositions favour sapphirine–orthopyroxene–quartz-bearing assemblages (shown below). In addition, the figure below shows that sapphirine–quartz assemblages without orthopyroxene (or sillimanite) can only occur in extremely restricted parts of composition space between the green triangles defining stable mineral assemblages (e.g. a, c, below), thus explaining the absence of that assemblage from *P–T* diagrams in larger systems such as used in this study. The presence of post-peak corundum in some of the corona structures (Fig. 6) cannot be explained in *P–T–X* space as corundum and quartz are not stable together under crustal conditions of metamorphism in reduced (rutile-bearing) rock compositions such as for R31180 (Mouri et al., 2004; Kelsey & Hand 2015).
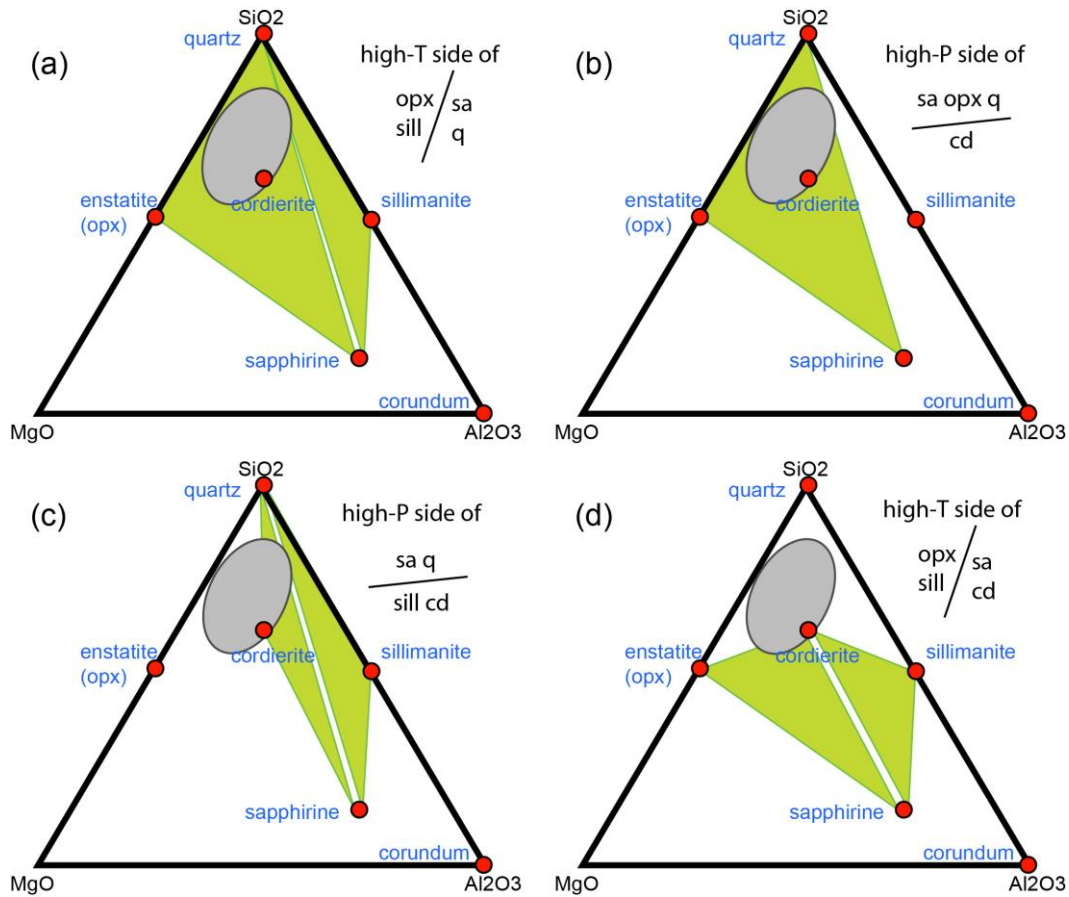
MgO–Al₂O₃–SiO₂ phase diagrams showing the possible stable mineral assemblages on the high-temperature (a, d) or high-pressure (b, c) sides of univariant reactions that define sapphirine stability in UHT rocks. The possible assemblages are shown by green triangles, and compositions of sapphirine–quartz rocks (including FeO in sum with MgO) (e.g. Ellis et al., 1980; Grew, 1980) are depicted by grey ellipse. The compositions of minerals used for the diagrams are: enstatite = Mg₂Si₂O₆, cordierite = Mg₂Al₄Si₅O₁₈, sillimanite = Al₂SiO₅, sapphirine = Mg₄Al₈Si₂O₂₀, quartz = SiO₂, corundum = Al₂O₃. For reactions depicted in (a) and (b) that allow sapphirine–quartz stability, common rock compositions sit in the stability field of sapphirine–orthopyroxene–quartz much more so than sapphirine–sillimanite–quartz (see also (c)).